Development of a Concept for Forced Response Investigations

Entwicklung eines Konzeptes zur Schaufelschwingungsanregung in Verdichtern

by
Felix Holzinger

Thesis submitted to the faculty of the Virginia Polytechnic Institute and State University in partial fulfillment of the requirements for the degree of

Master of Science
in
Mechanical Engineering

Walter F. O'Brien, VT-Chair
Heinz-Peter Schiffer, TUD-Chair

Jan Helge Bøhn, VT-Member
Manfred J. Hampe, TUD-Member

11/20/2009
Blacksburg, Virginia, US

Keywords: compressor, transonic, flutter, forced response, excitation system, air injection

Development of a Concept for Forced Response Investigations

Entwicklung eines Konzeptes zur Schaufelschwingungsanregung in Verdichtern

Felix Holzinger

PREFACE

In accordance with the rules of the Dual Master of Science Degree Program in Mechanical Engineering at Virginia Tech and at the Technische Universität Darmstadt has the present work also been presented at TU Darmstadt, Germany.

ABSTRACT

Striving to improve performance and lower weight of aircraft engines, modern compressor blades become thinner and lighter but higher loaded resulting in an increased vulnerability towards flutter. This trend is further aggravated through blisk designs that diminish structural damping and therewith flutter margin. Modern 3D wide-chord blade designs result in complex structural behaviors that add to the difficulty of correctly predicting flutter occurrence.
To counteract above tendencies by driving the physical understanding of flutter and thereby helping to improve aero engine design tools, free flutter as well as forced response will be investigated in the 1.5 stage transonic compressor at TU Darmstadt. Aim of the forced response campaign is to determine the system damping in the stable compressor regime. Hence a novel excitation system capable of dynamically exciting specific rotor blade modes is needed. It is aim of the present work to find a promising concept for such a system.
In the present work, the requirements for an excitation system to be used in the TUD compressor are defined with respect to achievable frequency, phase controllability, transferred excitation level, mechanical robustness, integrability and cleanliness. Different excitation system concepts, i.e. oscillating VIGVs, rotating airfoils, tangential and axial air injection are investigated numerically. An evaluation of the results obtained through 2D numerical studies proposes axial air injection as the most favorable concept.

ACKNOWLEDGEMENTS

This research was co-funded by the European Commission within the 7th Framework Programme (project FUTURE, grant agreement number 213414, www.future-project.eu). The author gratefully acknowledges this financial support.

The present work was performed at Volvo Aero Corporation in Trollhättan, Sweden.

I would like to express my sincere gratitude to Jan Östlund, Hans Mårtensson and Pieter Groth from Volvo Aero, who with their experience and expertise supported me throughout this work. I also owe them many thanks for their collegiality, which made the time at Volvo Aero so very pleasant.

Furthermore, I would like to thank Dr. O'Brien, Prof. Schiffer, Dr. Bøhn and Prof. Hampe for their work as committee members as well as their guidance and support throughout my studies. I especially thank Dr. Bøhn and Prof. Hampe for the great opportunity they gave me as well as all following students with the Dual MSME Program.

Finally, I owe many thanks to Edith Bothen, Barbara Seifert and Cathy Hill who with their endless patience and never ending support made the dual master degree come true.

Contents

List of Tables

List of Figures

Nomenclature

Greek Letters

π	[–]	Pressure Ratio
φ	[°]	Phase, Interblade Phase Angle
ϱ	$[\frac{kg}{m^3}]$	Density
γ	[–]	Specific Heat Ratio
Ω	[rpm]	Rotor Speed
ω	[Hz]	Eigenfrequency, Circular Frequency

Latin Letters

a	[m/s]	Speed of Sound
c	$[\frac{m}{s}]$	Velocity
c	[m]	Airfoil Chord Length
f	[Hz]	Frequency
F'$_{ax}$	[% Mean Axial Force]	Fluctuation of Axial Force
F'$_{tn}$	[% Mean Tangential Force]	Fluctuation of Tangential Force
F'	[% Mean Force]	Fluctuation of Total Force
M	[–]	Mach Number
p_s	[Pa]	Static Pressure
p_t	[Pa]	Total Pressure
R	$[\frac{J}{kgK}]$	Specific Gas Constant for Air
Re	[–]	Reynold's Number
t	[% Airfoil Chord]	Airfoil Thickness
u	[m/s]	Jet Velocity
u'	[m/s]	Axial Velocity Fluctuation
U$_{inf}$	[m/s]	Undisturbed Axial Velocity
v'	[m/s]	Tangential Velocity Fluctuation

Abbreviations

General

ADP	Aero Design Point
DL1	Design Loop 1
DL2b	Design Loop 2b
ND	Nodal Diameter
rpm	revolutions per minute
rps	revolutions per second
VIGV	Variable Inlet Guide Vane

Compressor Configurations

R1	Rotor 1 (TU Darmstadt Designation)
R6	Rotor 6 (TU Darmstadt Designation), *Fanny* (Volvo Aero Designation)
R1S1	Compressor Configuration with Rotor 1 - Stator 1
R6S1	Compressor Configuration with Rotor 6 - Stator 1

Blade Modes

1F	First Flap Mode
1T	First Torsional Mode
2F	Second Flap Mode

Numerical Simulations

CEL	CFX Expression Language
FF Domain	Front Frame Domain
R Domain	Rotor Domain
SV Domain	Strut and VIGV Domain

Cylinder Geometries

SCD05S01	Slotted Cylinder, Diameter 5 mm, Slot Width 1 mm
SCD05S02	Slotted Cylinder, Diameter 5 mm, Slot Width 2 mm
SCD05S03	Slotted Cylinder, Diameter 5 mm, Slot Width 3 mm
CCD05S01	Crossed Cylinder, Diameter 5 mm, Slot Width 1 mm
ECD05a2b1	Elliptic Cylinder, Diameter 5mm, Radii Ratio 2 to 1
ECD05a3b1	Elliptic Cylinder, Diameter 5mm, Radii Ratio 3 to 1

1 Introduction

Like all other machines, turbomachines and their components are susceptible to vibrations. Usually, these vibrations have very limited amplitudes resulting in uncritical stress levels only. Nevertheless, under certain conditions vibration amplitudes can grow significantly and therefore not only limit the operability, but lead to serious damage or even destruction of the entire machine.
In order to assure full functionality as well as safe operability, special care needs to be taken to design turbomachines as to avoid critical vibrations and predict under which operational conditions potentially harmful vibrations with high vibratory stress levels can occur.

The most critical vibrational phenomena related to turbomachinery are resonances and the so-called flutter, a flow induced vibration with high damage potential.

Especially in modern aircraft engine designs, where the driving forces are "lowering weight, raising performance and cost effective manufacturing" leading to "thinner, lighter but more loaded blades"[1], the vulnerability towards flutter is significantly increased.
This trend is further aggravated by blisk designs that diminish structural damping and therewith flutter margin.
Modern wide-chord and 3D blade designs (see Figure 1.1) result in complex structural behaviors that add to the difficulty of correctly predicting flutter occurrence.

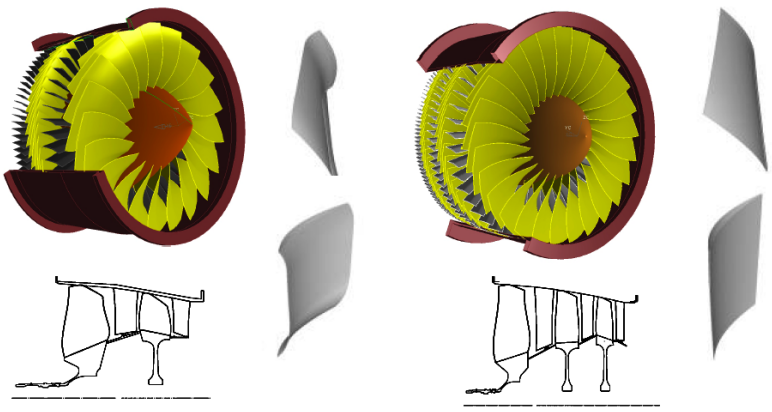

Figure 1.1: Modern 3D wide-chord (left) vs. old (right) compressor design, used with permission of [1]

Hence, there is a strong need for advancing flutter prediction methods in order to overcome the above described problems.
It is aim of FUTURE to establish an experimental data base for fine-tuning the flutter prediction tools and to improve the understanding of the underlying physics leading to flutter.

1.1 The Transonic Compressor Facility at TU Darmstadt

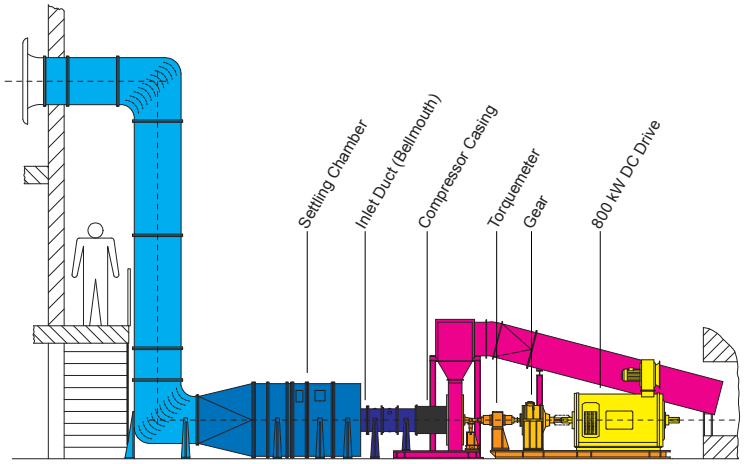

Figure 1.2: Transonic Compressor at TU Darmstadt

As part of FUTURE, engine relevant[1] compressor flutter tests will be performed at the Transonic Compressor Test Rig [15] at the Department of Gas Turbines and Aerospace Propulsion at TU Darmstadt. Figure 1.2 provides an overview of the compressor facility that represents the design of a typical front-stage of commercial turbofan high-pressure compressors.
As illustrated in the above figure, ambient air is sucked in and led through settling chamber and calibrated bell-mouth intake into the compressor.
The rotor is driven by an 800 kW DC-drive. A gearbox is increasing the shaft speed to a maximum speed of about 20 000 rpm. The shaft torque is measured with a torquemeter.
Temperature and pressure probes upstream and downstream of the compressor stage are used to calculate total stage pressure ratio[2] as well as isentropic efficiency[3].

[1] Other than cascades, rotating rigs are capable of modeling the 3D nature of the flow, but do so under conditions that make it difficult to extract detailed information about the system damping [3, 4, 5].
[2] $\mathrm{pr} = \frac{p_{03}}{p_{01}}$, where 01 and 03 denote conditions up- and downstream of the compressor stage
[3] $\eta_{st} = \frac{h_{03s} - h_{01}}{h_{03} - h_{01}}$, see [8]

The transonic compressor will be equipped with a new rotor, R6, that will be designed with the particular goal of achieving a well defined rotor blade flutter within the operating domain of the compressor (see [13]). Aim is, to drive the rotor into stall flutter before actually reaching the stall line as is explained below.
Furthermore, the compressor will be enhanced to a $1\frac{1}{2}$ stage environment by adding 15 VIGVs[4] upstream of the rotor for being able to adjust the inlet flow profile during the testing. Thereby, the correlation between VIGV angle and system damping can be investigated.

Table 1.1 compares the compressor standard configuration R1S1[5] against the new configuration R6S1. The data for R6S1 refers to Volvo Aero rotor design loop 1 and is subject to change as rotor design loops 2 and 3 are released.

Table 1.1: Compressor data (blue values referring to design loop 1)

	R1S1	R6S1
Flow Direction	axial/axial	axial/axial
Drive Power	800 kW	800 kW
Shroud Diameter	0.38 m	0.38 m
No. of Stator Vanes	29	29
No. of VIGVs	–	15
No. of Rotor Blades	16	19
Shaft Speed	20 000 rpm	18 000 rpm
Hub/Tip Ratio	0.51	0.50
Pressure Ratio	1.50	1.42
Mass Flow	16.0 kg/s	14.2 kg/s
Tip Speed	400 m/s	360 m/s

Lower rotor speed as well as decreased design mass flow mainly account for the limited drive power. With a design point shaft speed of 18 000 rpm, there is sufficient margin left for the 105% speed line in case flutter cannot be achieved for design speed.
Using a more moderate rotor design speed of 18 000 rpm also brings down the rotor mean stresses and thereby extends the HCF margin when performing the flutter tests.
The increased number of blades results from the design intent to bring down the frequencies of the first rotor blade eigenmodes[6].
Figure 1.3 shows the designated compressor layout including front frame struts, VIGVs, R6, S1 and diffuser struts[7]. A throttle attached to the radial diffuser is used to back pressure the compressor.

[4] Variable Inlet Guide Vanes
[5] MTU Rotor 1, MTU Stator 1
[6] For rotor design loops 2 and 3, the blade count will be further increased.
[7] A 94 poles slip ring system replacing the nose cone will be mounted upstream of the front frame struts. The slip ring cooling system pipes will also be penetrating the domain upstream of the front frame struts.

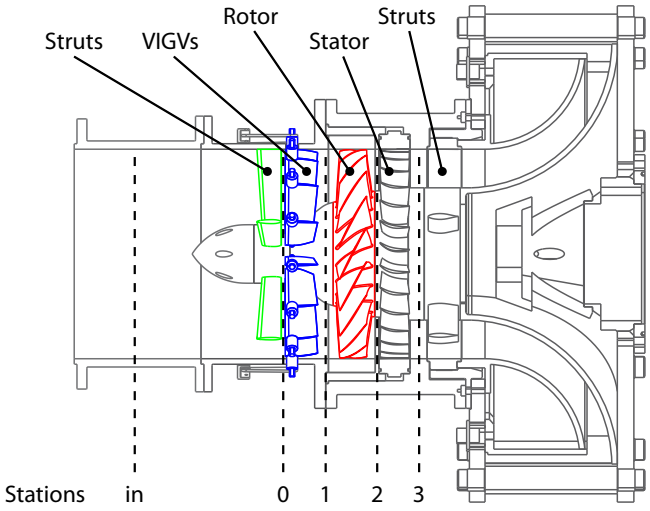

Figure 1.3: Compressor layout and definition of stations

1.2 Forced Response Testing

As outlined in [13], FUTURE is aiming to provide new sets of data to enhance the understanding of the inception of flutter [7, 10, 14, 18]. Hence, R6 will be designed to reach transonic stall flutter before actually running into stall[8]. Figure 1.4 shows a sketch of the corresponding compressor map where the transonic stall flutter limit is lower than the the stall line itself. Moreover, it shows the different flutter regimes as defined by Cumpsty [6][9].

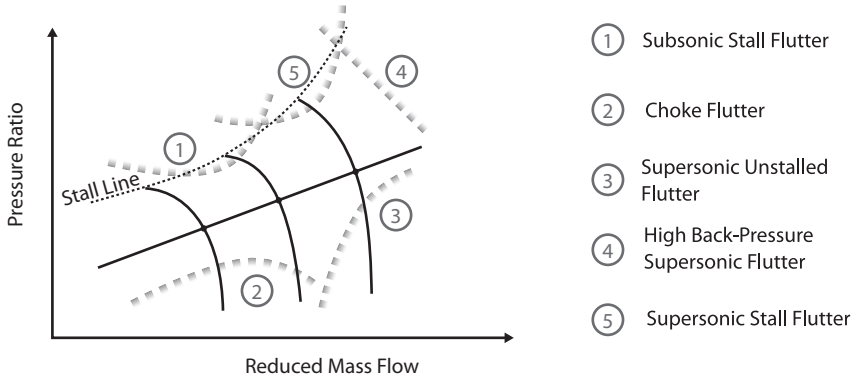

Figure 1.4: Compressor map with flutter regimes

[8] $\pi_{ADP} < \pi_{Flutter} < \pi_{Stall}$
[9] Supersonic Unstalled Flutter can be further divided into High and Low Back-Pressure Flutter

The TUD compressor test program will consist of three different campaigns:

- Commissioning of the New Compressor Configuration R6S1
- Forced Response Campaign
- Free Flutter Campaign

The compressor commissioning has the aim of confirming that the new configuration R6S1 operates as predicted.

Main goal of the forced response tests is to explore the correlation between system damping and operating conditions as well as interblade phase angles outside the flutter domain.
Therefore, an excitation system will be integrated upstream of the compressor rotor in order to create periodic flow disturbances that will then excite the rotor. The compressor will be operated at different points, the excitation system will be utilized to excite the rotor and the rotor blade displacement as a measure of the system damping will be recorded[10].
The excitation of the rotor will be performed by running frequency sweeps around the predicted eigenfrequencies of the blades.
As shown in Figure 1.5, the amplitudes of the rotor blade displacement will reach a maximum for excitation frequencies close to the blades' eigenfrequencies. Moreover, it can be readily seen that the blade displacement will grow for decreased system damping and decline for increased system damping.
With the structural damping having already been determined, the aerodynamic contribution to the damping can be derived from the system damping.

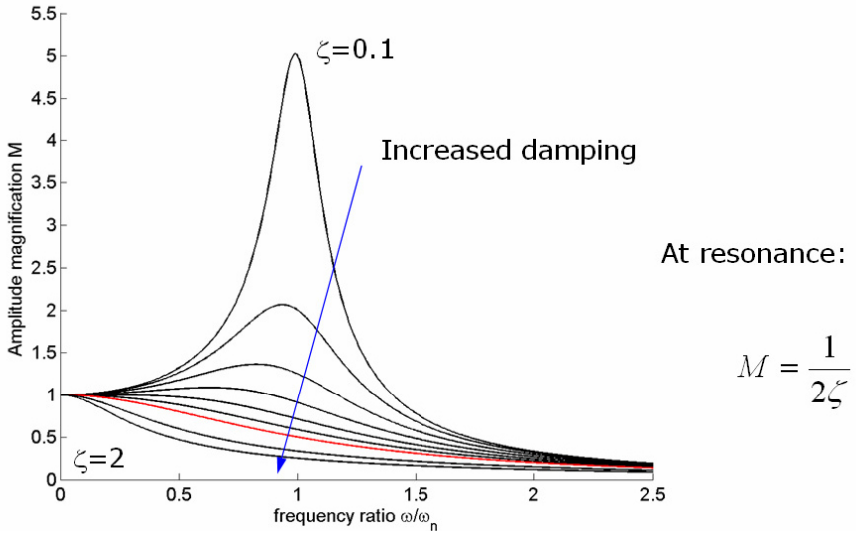

Figure 1.5: Effect of system damping on oscillation amplitude during forced response, used with permission of [20]

[10]The procedure for deriving the system damping from the recorded blade displacement is outlined in [3].

Risk reduction is another reason for running a forced response campaign prior to the free flutter tests.
Instead of unexpectedly ending up in free flutter[11], it is planned to iteratively approach the flutter limit where blade displacement amplitudes grow as the system damping is diminishing towards zero. Referring to Figure 1.4, approaching the flutter limit means to begin at a point of low pressure ratio and follow the speed lines upwards by increasing the back pressure. When a point of zero system damping is reached, the oscillation amplitudes stop decaying over time[12].

Finally, forced response possibly provides the means for controlling free flutter.
It is not yet planned to employ the excitation system for controlling free flutter, but this might be an interesting area for future research.

Once the forced response campaign is completed, the obtained results will be used to decide on the procedure for the free flutter campaign.
During the free flutter campaign, the compressor will actually be driven into the region with negative system damping. As further explained in the appendix, negative system damping is equivalent to adding energy to the vibration instead of dissipating it. Hence, vibrational amplitudes stop decaying over time and start growing until nonlinear effects begin to limit them. In order to yet assure a safe operability of the compressor while in free flutter, special measures will be taken to safely withdraw the compressor from the flutter region.

1.3 Implementation of an Excitation System

For being able to measure rotor blade displacements and therewith system damping as a function of operating conditions as well as interblade phase angles, a novel excitation system will be integrated into the front frame of the Transonic Compressor Test Rig at TU Darmstadt.

Aim of this Master Thesis is thus to develop an excitation system concept that is capable of exciting the rotor blades to a measurable but safe degree without negatively affecting the overall compressor operation.

As outlined by Vogt in [19], interaction phenomena present in turbomachine components are

- Wake Interaction
- Vortex Interaction
- Potential Interaction

[11] Outcome of FUTURE is to improve the flutter prediction accuracy.
[12] More information about system damping is given in the appendix.

Different excitation system concepts utilizing the individual interaction phenomena to varying extents will be discussed in the following chapters.
As mentioned before, all concepts are based upon the idea to generate periodic flow disturbances that will have an either direct or indirect effect on the rotor blades resulting in the desired rotor blade displacements. Like all periodic signals, the periodic flow disturbances can be characterized by

- Frequency f
- Phase φ
- Amplitude A

This can be summarized as $ex(t) = A\sin(2\pi ft + \varphi)$, where $ex(t)$ is the time varying signal and $2\pi f = \omega$ the circular frequency.
For a successful implementation of the excitation system, controllability of all above mentioned parameters needs to be guaranteed. This will be specified in more detail in the following chapter.

The concept of all investigated excitation systems is drafted in Figure 1.6 that shows a sketch of the unwrapped compressor geometry outlined in more detail in Figure 1.3.

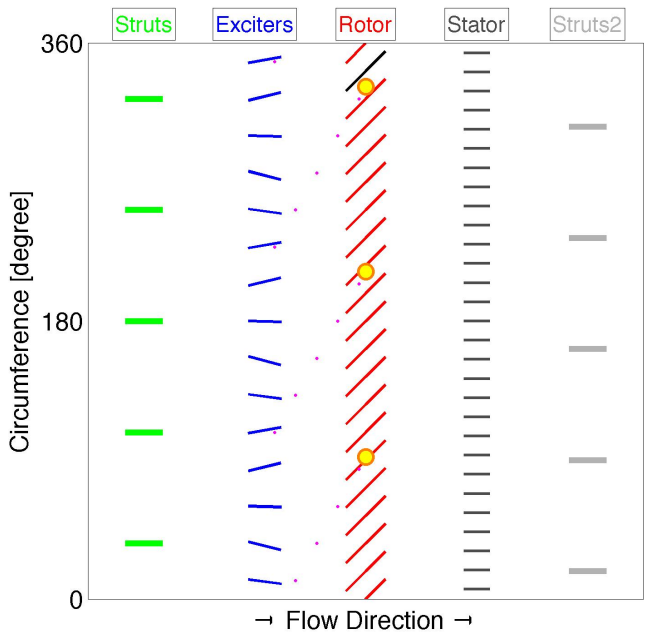

Figure 1.6: Implementation of an excitation system into the compressor front frame

In this case, the VIGVs are employed as exciters by performing an out-of-phase oscillating motion and thereby generating flow disturbances (as symbolized through the small pink circles) that will then affect the rotor (as indicated by the larger orange circles).

Depending on the phase difference between the individual exciters as well as their number, a varying number of excitation cycles will travel around the compressor annulus. In this case, the number of cycles also referred to as nodal diameters is 3. This is indicated through the 3 forward leaned diagonals beginning where the flow disturbances are generated by the exciters and ending where the flow perturbations interact with the rotor blades.
Stator and diffuser struts are colored in grey as their influence was neglected in this study.

2 Technical Specifications

It is aim of the present Master Thesis to find a concept for an excitation system that is capable of exciting the newly designed rotor. Exciting the rotor implies that the flow disturbances generated by the excitation system do result in forces on the rotor blades that lead to measurable but safe rotor blade displacements[1].
Shape and amplitude of the rotor blade displacement depend on the excited rotor blade mode as well as the interblade phase angle.
As outlined in [21], the "three basic natural modes are referring to the directions of the principal inertial axes of the blade":

- F or Flap, i.e. bending normal to the blade's skeleton line
- E or Edgewise Bending, i.e. bending in the direction of the blade's skeleton line
- T or Torsion, i.e. torsion around the blade's stacking line

Figure 2.2 shows above mentioned basic natural blade modes, namely 1F, 1E and 1T. Besides the basic natural modes, higher order blade modes and combinations thereof exist.

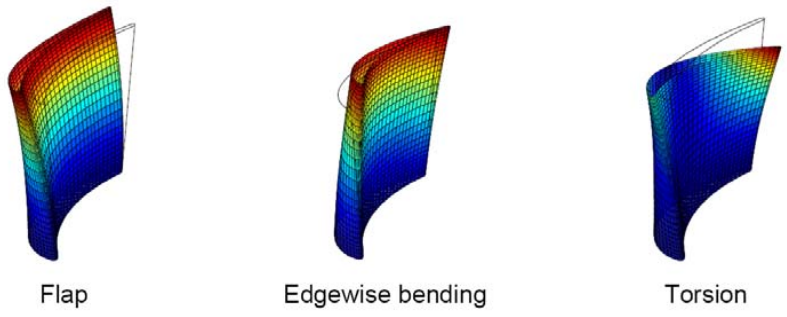

Figure 2.1: The 3 basic natural blade modes, used with permission of [21]

Neglecting mistuning effects[2], all rotor blades feature identical blade modes and eigenfrequencies. Thus, the interblade phase angle translates into a traveling wave pattern that is referred to as nodal diameter. The number of nodal diameters is equivalent to the number of cycles around the circumference as already mentioned in the preceding chapter. Waves can travel

[1] The modal force for sufficient excitation of the rotor blades was provided by Volvo Aero.
[2] Mistuning arises from manufacturing tolerances, imperfections and varying wear and results in differing individual blade mode shapes and varying blade eigenfrequencies.

either with the rotor or in reverse direction. Forward traveling waves are the ones traveling with the rotor, backward traveling waves are the ones traveling in reverse direction.

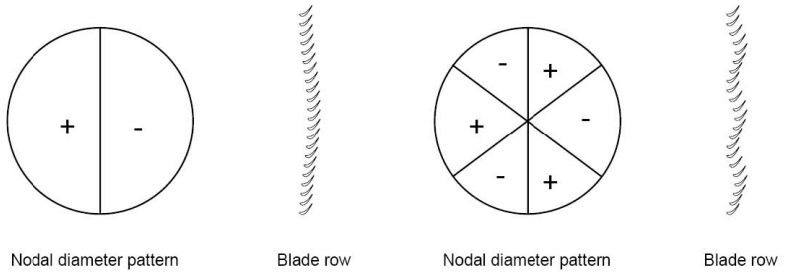

Figure 2.2: Rotor response for 1 and 3 nodal diameters, used with permission of [21]

When thus looking at the flutter predictions for R6 as given in Figure 2.3 showing the system damping for R6 design loop 2b, we can readily see that 1F is the mode most likely to flutter for interblade phase angles of about -50°. The corresponding plot of the work coefficient is given in the appendix in Figure 8.1.
Subsequently, the excitation system will be designed to excite the 1F mode with 3 nodal diameters forward traveling wave.
The specifications for such an excitation system are given in detail in the following sections.

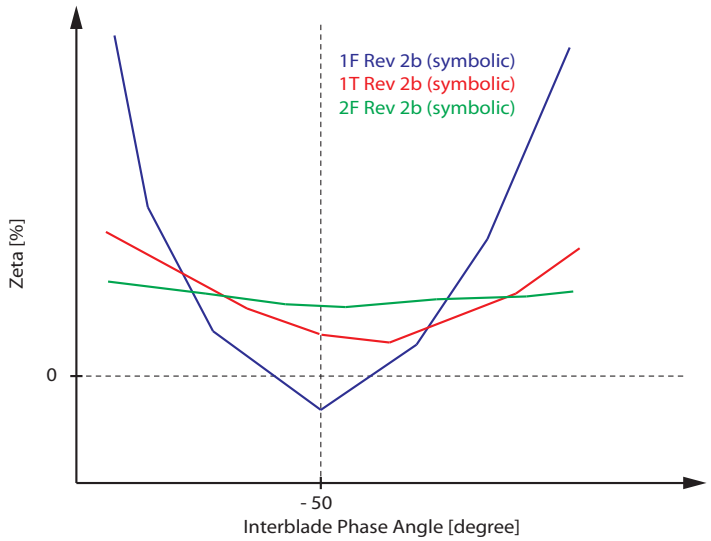

Figure 2.3: Volvo Aero flutter prediction results (interblade phase angle inversely defined and symbolic values only)

2.1 Frequency Requirements

As outlined before, 1F is the blade mode most prone to flutter and will therefore be excited during the forced response campaign. The damping for the 1F mode is lowest for 3 nodal diameters and the number of actuators was set to 15 based upon the number of VIGVs. The design speed is 18 000 rpm. This data is summarized in Table 2.1.

Table 2.1: Input for transforming blade frequencies to the stationary frame of reference

Design Speed	Ω	18 000 rpm
No. of Nodal Diameters	n	3
No. of Actuators	m	15

Whereas the rotor blades will oscillate in the frame of reference of the rotor, the excitation system will be installed in the stationary frame.
In order to get the excitation frequency requirements for the stationary frame, the rotor blade frequencies need to be transformed from the relative into the stationary frame.
This can be done with the following relationship

$$f = \frac{\Omega}{60} \cdot n + \omega \tag{2.1}$$

, where Ω as well as n are taken from Table 2.1 and ω is taken from Table 2.2 showing the lowest blade mode frequencies for design loops 1 and 2b of R6[3] at design speed.

Table 2.2: Frequencies of the R6 blade modes closest to flutter

Blade Mode	Eigenfrequency (DL1)	Eigenfrequency (DL2b)
ω(1F)	588 Hz	535 Hz
ω(1T)	1643 Hz	1271 Hz
ω(2F)	1788 Hz	1560 Hz

For the 1F mode, this leads to excitation frequency requirements of 1488 Hz for design loop 1 and 1435 Hz for design loop 2b.
Since predictions can be inaccurate, a safety margin of about 100 Hz is added to guarantee the functionality of the excitation system for the target frequencies.
Thus, the frequency requirement of the excitation system is set to a maximum excitation frequency of 1600 Hz.

[3]The given values are the predictions made by Volvo Aero

2.2 Mechanical Robustness

In order to assure a safe operation of the test rig during the forced response campaign, the excitation system needs to be mechanically robust[4].
Since the excitation system will generate high frequency flow perturbations, care needs to be taken to design the excitation system as to avoid self-excitation.
The requirement for the eigenmodes of the exciters can hence be directly derived from the target excitation frequency as specified in the previous section.
Designing the exciters such, that their lowest eigenmodes are twice as high as the maximum excitation frequency, the operation of the exciters can be considered uncritical.
To meet this criterion for a maximum excitation frequency of 1600 Hz, the lowest exciter eigenmode needs to be above 3200 Hz. If this turns out to be unfeasible, it was agreed that a frequency margin of 400 Hz is sufficient.

2.3 Phase Controllability

As outlined by Östlund in [13], part of the forced response testing is to investigate the correlation between system damping and interblade phase angle.
Subsequently, the excitation system will be generating flow disturbances with varying traveling wave patterns and thereby different numbers of nodal diameters.
As outlined in [3], nodal diameters can be translated to interblade phase angles[5] using

$$\varphi = 2\pi \cdot \frac{n}{m} \tag{2.2}$$

for forward traveling waves and

$$\varphi = 2\pi \cdot \frac{m-n}{m} \tag{2.3}$$

for rearward traveling waves, where φ is the interblade phase angle, n the number of nodal diameters and m the number of exciters.
Using the values from Table 2.1, the interblade phase angle for the exciters is calculated to be 72°.
In order to be able to excite various interblade phase angles of the rotor, the interblade phase

[4] Aim of this study is to find feasible concepts from the aerodynamic point of view. Therefore, this issue is not addressed directly in the present study, but still needs to be remembered when defining the concepts.
[5] This is valid for both, the interblade phase angles between the rotor blades as well as the interblade phase angles between the exciters. The two values will differ, though, resulting from the different number of rotor blades and exciters.

angle of the exciters needs to be accurately controlled. It was agreed that phase controllability of about 10% of the maximum angle was precise enough. This results in a phase controllability requirement of about $\pm 5°$.

2.4 Transferred Excitation Level

It was mentioned before, that the system damping will be determined during the forced response campaign by measuring the rotor blade displacement amplitudes[6]. Therefore, the excitation system needs to generate flow disturbances that cause measurable but safe[7] blade displacements.
Since the excitation will be applied in regions where the system damping ranges from 1% down to 0.1%, the blade displacement amplitudes will increase approximately by factor 10 for unchanged excitation level. This was also shown in Figure 1.5.
If amplitudes vary by a factor of 10, it is questionable whether they can be measured for large system damping and safely operated for small system damping.
It is therefore absolutely necessary that the excitation level can be adjusted and thus the amplitudes controlled.

Another issue concerning the excitation level is the total amount of perturbations that are added to the compressor system, i.e. the cleanliness of the signal with regard to higher harmonics and noise content.
The higher the excitation level used for exciting the desired rotor blade mode, the less perturbations need to be added in total. It is therefore of prior interest to find a concept with as high and clean an excitation signal transferred to the rotor as possible.

In order to maintain repeatability of the tests as well as predictable rotor blade response, the impact of the excitation system on the mean flow needs to be limited and well determined. Especially for highly turbulent flow as a result of the excitation, it will become particularly difficult to predict and control the rotor response.
The lower and the more predictable the impact on the mean flow for measurable rotor blade displacements, the better.

2.5 Integrability and Cleanliness

In order to be able to integrate the excitation system into the front frame of the compressor, the system needs to be designed as to not interfere with the existing front frame components.

[6] The same procedure will be followed again during the free flutter campaign, but then with blade displacement resulting from negative aerodynamic damping instead of excitation.
[7] What can be considered safe blade displacements is addressed by Woods in [22].

For excitation system concepts that require the installation of additional exciters, an installation envelope has to be defined.
The installation envelope will be constrained by

- the turning angle of the VIGVs
- a safety distance to the rotor leading edge
- sufficient space for inserting probes in the annulus between exciters and rotor leading edge

Subject of the forced response campaign is to investigate the influence of the VIGV angle on the system damping. The maximum turning angle of the VIGVs was defined to be ±30°.
That being the case, the exciters can only be installed where they do not limit the sweep of the VIGVs[8].

Since the rotor will be designed with a particular high susceptibility towards flutter, sources of possibly harmful potentials shall maintain a safety distance towards the rotor leading edge. The safety distance therefore depends on the respective exciter design.

As it is also part of the forced response campaign to determine the impact of the excitation system on the mean flow, probes will be inserted downstream of the exciters to characterize the excitation.
Since the probes also have to maintain a safety distance to the rotor, this criterion is the more critical and hence the limiting one.

For the above reasons, the number of exciters was set equal to the number of VIGVs.
If the VIGVs themselves are not directly employed as excitation system, the additional exciters can then be equidistantly installed in between the VIGVs. Thereby, no parts are closer to the rotor leading edge than the trailing edge of the VIGVs. Moreover, the sweep of the VIGVs will be the least constrained, depending on the actual dimension and axial position of the exciters relative to the VIGVs rotational axes.

Cleanliness of the excitation system is a critical issue since the rotor will be instrumented with strain gauges and up to 21 pressure transducers.
In order to prevent the rotor instrumentation from taking damage no humidity[9], dust, oil[10] or other potentially hazardous materials can be allowed to enter the compressor domain.
This was the main reason for withdrawing from the initial excitation system concept based on oil droplet injection.

[8] If not feasible, the 30° could be relaxed to 15°
[9] e.g. condensation problems with compressed air injection.
[10] e.g. from bearings.

2.6 Excitation System Concepts

In the following, the different excitation system concepts investigated in this work will be shortly presented, namely

- Oscillating VIGVs
- Rotating Cylinders
- Tangential Air Injection
- Axial Air Injection

Radial Air Injection was also discussed, but due to the limitations of the used setup not further analyzed.

2.6.1 Oscillating VIGVs

Oscillating VIGVs are the excitation system concept aimed for after the oil droplet injection was discarded due to the potential damage the rotor instrumentation could take from the oil droplets.
The concept is based on an oscillating motion of the VIGVs and thereby varying inlet flow angles, the excitation level depends on the oscillation angle of the VIGVs.
For exciting the 1F mode with 3 nodal diameters, the phase angle for the periodic oscillation of the VIGVs is 72°, the maximum oscillation frequency is 1600 Hz as explained in the previous sections.
Figure 2.4 gives a comparison between standard setup (left) and the case with oscillating VIGVs (right). The graphic shows $\frac{1}{5}$ of the compressor annulus with a scaled rotor.

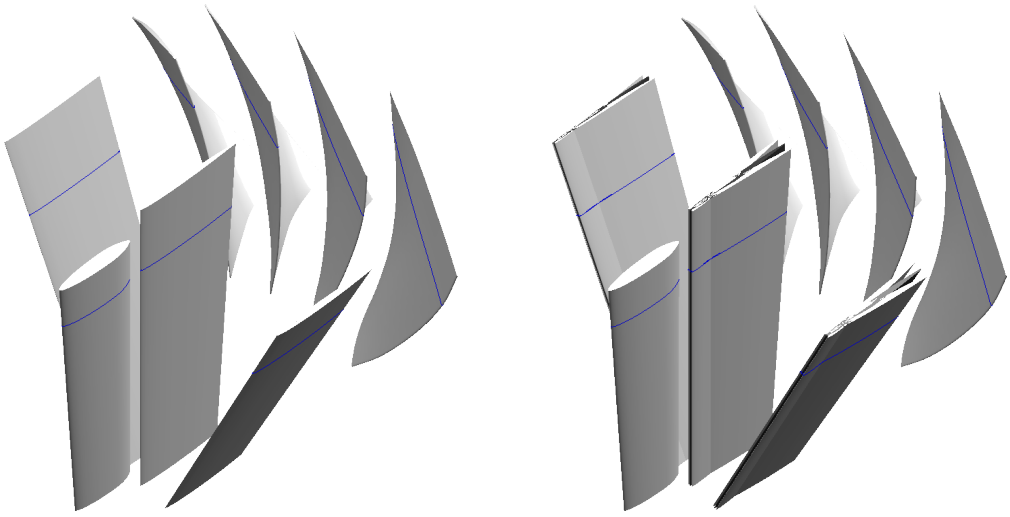

Figure 2.4: Standard Setup vs. Oscillating VIGVs

2.6.2 Rotating Cylinders

Rotating Cylinders is a derivative of the Oscillating VIGVs concept where the oscillating motion of the VIGVs was replaced by a rotating motion of additional profiles sticking into the compressor domain.
With this concept, the excitation level depends on the geometry of the rotating profiles as well as their length.
In order to excite the 1F blade mode with 3 ND, the phase angle of the cylinder rotation must be set to 72° and the excitation frequency to 1600 Hz.
For symmetric profiles, at least two excitation cycles are completed per cylinder revolution[11]. Therefore, the excitation phase angle results in a phase difference between the cylinders of 36°. The excitation frequency of 1600 Hz transforms to a rotating speed of 800 revolutions per second.
Figure 2.5 compares standard setup (left) against the setup with rotating cylinders for exciters, in this case cylinders with elliptic profiles. Again, $\frac{1}{5}$ of the compressor annulus with one strut, three VIGVs and four blades of a scaled rotor is shown. In the right partial image, three rotating elliptic profiles are added halfway between the VIGVs. The length of these profiles will be designed to meet the excitation level demands.

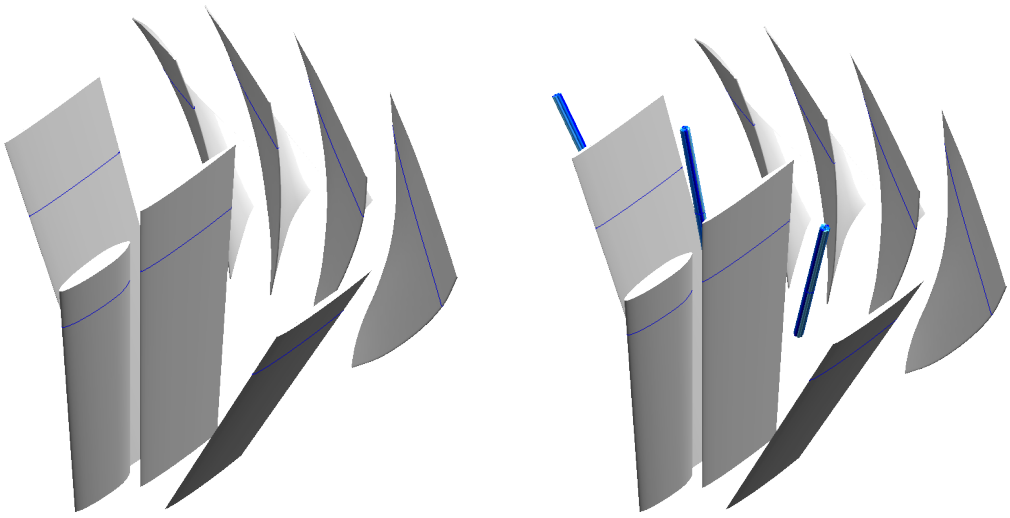

Figure 2.5: Standard Setup vs. Rotating Cylinders

2.6.3 Tangential Air Injection

With the Tangential Air Injection concept, the rotor excitation will be achieved by injecting compressed air through additional injectors tangentially towards the VIGVs.
The amplitude of the rotor blade displacement will thus depend on the injected mass flow

[11] Depending on the cylinder design, multiple cycles can be completed per revolution.

and consequently on supply pressure and injection area.
For exciting the 1F mode of the rotor blades with 3 nodal diameters, the phase difference between the compressed air pulses needs to be 72°, the frequency of the pulsed compressed air injection is 1600 Hz.
In Figure 2.6 a comparison between the standard setup and the setup with additional profiles for tangential air injection is given. As with the rotating cylinders, the profiles are added midway between the VIGVs. Yellow stripes on the injector profiles mark the injector nozzles directing the injected air pulse tangentially towards the VIGVs.

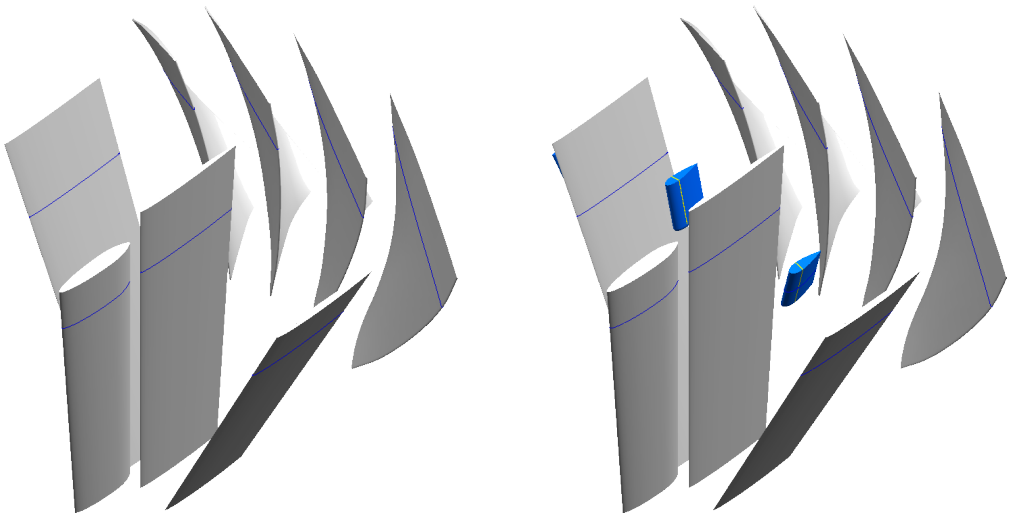

Figure 2.6: Standard Setup vs. Tangential Air Injection

2.6.4 Axial Air Injection

Axial Air Injection is a concept similar to the Tangential Air Injection, only that the compressed air pulses are aiming directly for the rotor instead of being injected towards the VIGVs.
The amplitude of the rotor response will again depend on the injected mass flow and hence on injector nozzle area and pressure. Other than for the Tangential Air Injection, the jet velocity is also of importance. For a jet velocity equal to the core flow velocity, the rotor won't feel much of an excitation.
In order to excite the 1F blade mode of the rotor, the phase difference between the compressed air injection cycles has to be set to 72°. The compressed air needs to be pulsed with a frequency of 1600 Hz.
A comparison between standard setup and the setup with axial air injectors added equidistantly between the VIGVs is shown in Figure 2.7 for $\frac{1}{5}$ of the compressor annulus.
The graphic illustrates the same injectors as for the Tangential Air Injection, only that now

the injector nozzles are located at the injector trailing edge[12].

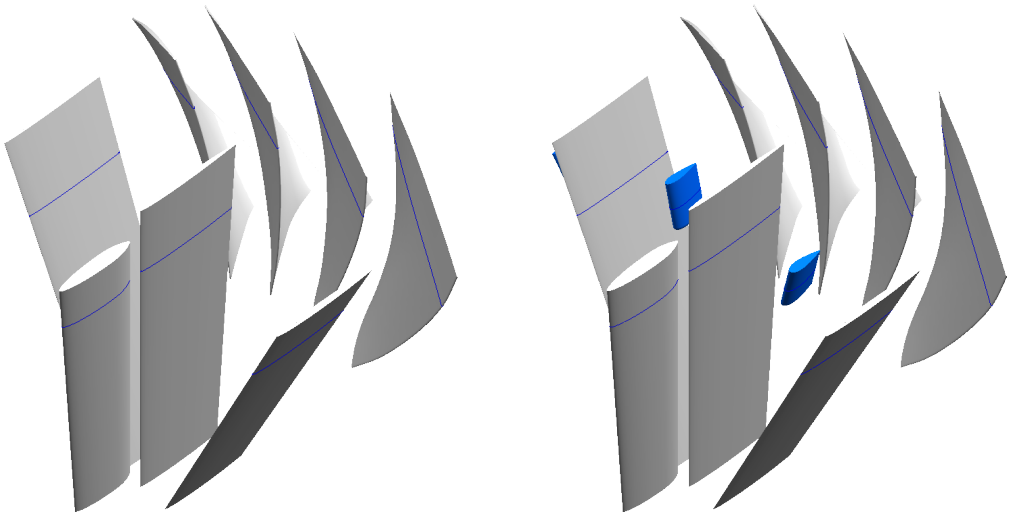

Figure 2.7: Standard Setup vs. Axial Air Injection

[12] As for trailing edge cooling, where holes are drilled in the trailing edge of the turbine blades.

3 Oscillating VIGVs

When FUTURE was first proposed, the initial idea was to utilize an oscillating motion of the existing VIGVs for exciting the desired rotor blade mode.
The oscillating motion of the VIGVs was specified to have a frequency of 1600 Hz for exciting the 1F rotor blade mode as described earlier in this document. If the excitation was to have 3 nodal diameters, the phase angle of the VIGVs needs to be set to 72°. For obtaining a sufficient excitation level, the oscillation amplitude was defined to be 3° for the 1600 Hz excitation and 5° for a lower excitation frequency of 500 Hz.

It then turned out, that oscillating the VIGVs based on the Hulda VIGV design (see [12, 9]) with the above specified parameters is not feasible for

- stiffness
- strength
- power

reasons.

As outlined by Snedden [16], the first three modes of the VIGV occur at eigenfrequencies of 342 Hz, 665 Hz and 1051 Hz. Since all of these eigenfrequencies are below the excitation frequency of 1600 Hz, a VIGV design based on the Hulda VIGVs is not stiff enough to be safely oscillated.
When oscillating the VIGVs as described above, the resulting shear stress at the profile root of the VIGV was calculated to be 590 MPa, whereas the maximum shear strength for 7075 Al T6 is only 331 MPa.
Finally, the total mean power required to overcome the inertia of the VIGVs when performing the oscillation was estimated to be 235 kW, the total peak power was as high as 740 kW[1].

Considering the above problems, it becomes readily clear that an excitation system based upon an oscillating motion of the VIGVs is not feasible without changing the VIGV design entirely.

The present work yet includes an aerodynamic study of the Oscillating VIGVs concept for reference purposes. The oscillation amplitude in the following aerodynamic study was reduced to 0.5° which is still not mechanically feasible, but at least a more realistic value.

[1] These values refer to a VIGV with the shaft moved to the optimum position.

3.1 Mesh Setup

For investigating the aerodynamic aspects of the different excitation system concepts, a 2D[2] numerical simulation using ANSYS CFX was performed.

Aim of the simulation was to obtain information about the rotor blade forces induced by the Oscillating VIGVs as well as the effect of the oscillation on the mean flow.
Therefore, the simulation includes the compressor front frame with struts and VIGVs as well as the compressor rotor.
It was assumed that the stator has little effect on the performance of the upstream excitation system and hence it was neglected in this study.

The mesh for the simulation was generated with ANSYS ICEM CFD, a commercial mesh generation program.

3.1.1 Defining the Geometry

The geometry used for the simulation consists of the strut profiles, the VIGV profiles and the rotor blade profiles as extracted at 92.5% tip radius.
This radius was chosen since the VIGVs are cropped at tip with a radius of 189.5 mm for mounting reasons[3] as shown in Figure 3.1. Using the profiles at 92.5% tip radius leaves sufficient margin towards this gap to obtain representative results.

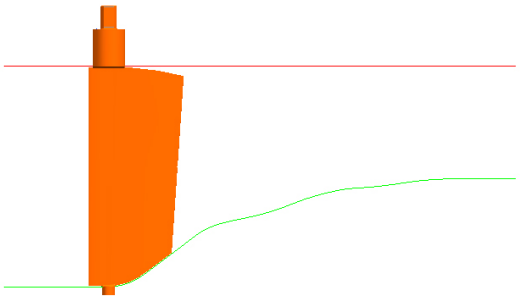

Figure 3.1: VIGV with hub and shroud line

In order to save computing time, the simulation setup includes one fifth of the compressor annulus only. Having 5 struts and 15 VIGVs, the model contains 1 strut and 3 VIGVs.

[2]The mesh is a 3D mesh, but is only two layers thick.
[3]The casing diameter is 380 mm leaving a clearance of 0.5 mm. During the installation, the VIGVs can therefore be rotated 360°.

This becomes more complicated for the rotor with 19 rotor blades[4]. For being able to model one fifth of the rotor while maintaining a pitch ratio of 1, a scaled rotor geometry was used with 20 instead of 19 rotor blades.
Figure 3.2 shows the geometry as is was employed to generate the mesh. The left partial image shows the profiles[5] with a blue line indicating the 92.5% tip radius, the right partial image shows the profiles as extracted at this radius.
The thickness of the profile sheets was set to 0.05 mm to meet the ANSYS CFD requirement that the thickness of the mesh layers is about the size of the elements near the wall boundaries.

Figure 3.2: Profiles with marked 92.5% tip radius and extracted profiles

3.1.2 Generating the Mesh

The mesh was generated as a multi-block structured hexahedral volume mesh with ANSYS ICEM CFD in two parts. The first mesh was generated for the strut and VIGV domain, the second mesh was generated for the rotor domain.

The strut and VIGV domain contains one strut located midway in circumferential direction and three VIGVs positioned accordingly.
The domain extends one strut chord length in upstream direction. In downstream direction, the domain is confined by the interface to the rotor domain halfway between VIGV trailing edge and rotor leading edge.
O-Grids were defined around all solids, namely the strut and the three VIGVs.
Along all solid walls, the nodes are distributed based on hyperbolic or bigeometric distribution laws.
In circumferential direction, the vertices are rotationally periodic.

The mesh for the rotor domain was set up in the same way with the exception that only a single rotor blade was meshed. Care was taken to have the suction side of the blade in the

[4]The rotor blade geometry is taken from design loop 1. The other design loops had not been released.
[5]The profiles are as generated from the point cloud files and don't show correct hub and shroud features.

farther extending part of the rotor mesh, since interfaces in critical regions can have negative effects on the quality of the results.
Once the meshing was completed, a rotational instance transform was applied to include all four rotor blades in the simulation.
As already mentioned, the rotor domain is upstream confined by the interface to the strut and VIGV domain halfway between rotor leading edge and VIGV trailing edge. In downstream direction, the rotor domain extends one rotor chord length.
The nodes along the rotor blade walls are allocated following hyperbolic distribution laws.
The mesh vertices satisfy periodicity in the circumferential direction.

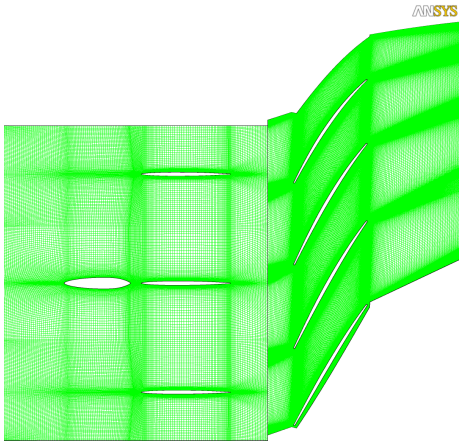

Figure 3.3: Hexahedral mesh as used for Oscillating VIGVs

Figure 3.3 shows the final mesh consisting of strut and VIGV domain mesh as well as the rotor domain mesh.
Table 3.1 summarizes the mesh quality statistics.

Table 3.1: Mesh statistics for Oscillating VIGVs

	SV Domain	R Domain
Nodes	180000	4 x 110000
Elements	240000	4 x 150000
Layers	2	2
Min. Angle	22.8°	22°
Determinant	0.75-1	0.9-1
Max. Aspect Ratio	282	183
Max. Volume Change	3	2.9
Average(y^+)	< 4	< 6.5

3.2 Solver Setup

3.2.1 Boundary Conditions and Domain Setup

For the numerical simulation ANSYS CFX as a commercial turbomachinery solver was used. At the inlet of the strut and VIGV domain, a total pressure boundary condition was applied with the values as specified in Table 3.2. The rotor outlet was defined as static pressure boundary condition with the static pressure taken from [11].
The obtained pressure ratio is with 1.48 slightly higher than that of the actual compressor, resulting from an inlet to outlet area ratio of 1 instead of a more representative one of about 1.1.
At all solid walls, standard no-slip wall boundary conditions were applied.
In circumferential direction, all interfaces were specified as rotationally periodic with 1 to 1 mesh connection method.
The bottom and top surfaces of all domains were defined as free-slip wall[6] boundary conditions.

Steady state simulations that were run to obtain the initial values for the transient simulations, had the interface between stationary SV Domain and rotating R Domain defined as stage interface.
All transient simulations had the interface between rotating and stationary domain specified as transient rotor-stator interface.

The turbulence model used is the Shear-Stress-Transport model, a combined k-ϵ k-ω model, which is considered superior to the standard k-ϵ model when it comes to accurately predicting flow separation as stated in [2].
The Total Energy[7] heat transfer model was applied in all domains.

Table 3.2: Boundary conditions at SV Inlet and R Outlet

	SV Domain Inlet	R Domain Outlet
Total Pressure p_t	101325 Pa	–
Total Temperature T_t	288.15 K	–
Turbulence Intensity	5%	–
Static Pressure p_s	–	124500 Pa

3.2.2 Mesh Motion

For being able to model the oscillating motion of the VIGVs, a CEL mesh motion was specified for the SV Domain.

[6] For round surfaces, symmetry boundary conditions cannot be selected.
[7] including viscous term

The mesh motion was applied using the *specified displacement* method. Since the VIGV oscillation is known, it can be assigned. Using this method, CFX deforms and smoothens the mesh for each time step depending on the specified displacement.
The motion of the VIGVs is defined in VIGV coordinates around the rotational axes of the VIGVs and then transformed back to absolute coordinates.

The chord of the VIGV in the center as shown in Figure 3.3 is aligned with the x-axis of the absolute coordinate system.
Subsequently, the coordinates of the rotational axis of the central VIGV can be given in the TUD coordinate system[8] as

- x_c = -314.9 mm
- $y_c = 0$ (center VIGV oscillates in x-z-plane)
- $z_c = 0$

Knowing the origin of the VIGV's rotational axis, the mesh displacement for the VIGV oscillation can be defined in two steps:

- Displacing the mesh according to the VIGV oscillation
- Projecting the mesh back onto the original duct[9]

The displacement of the mesh can then be assigned as

$$x_{disp} = -(x - x_c) \cdot (1 - \cos\alpha(t)) - (z - z_c) \cdot \sin\alpha(t)$$
$$z_{disp} = (x - x_c) \cdot \sin\alpha(t) - (z - z_c) \cdot (1 - \cos\alpha(t))$$

where x and z are the coordinates of the VIGV wall and

$$\alpha(t) = \hat{\alpha} \cdot \sin(2\pi f \cdot t + \varphi)$$

with $\hat{\alpha} = 0.5°$ being the oscillation amplitude and φ being the phase difference depending on the number of nodal diameters of the VIGV oscillation. f is the frequency of the performed excitation.
Projecting the mesh back onto the original duct is done by correcting the y-coordinate with

$$y_{disp} = \sqrt{r^2 - (z + z_{disp})^2} - y$$

where

$$r^2 = (z^2 + y^2)$$

For the remaining two VIGVs, the procedure for specifying the mesh oscillation is the same

[8] The origin of the TUD coordinate system lies on the compressor axis at the radial diffuser flange.
[9] When the VIGV is oscillated, the mesh leaves the initial duct defined by the 92.5% tip radius. For that reason, the mesh needs to be projected back onto the original duct.

with the exception that the rotational axes of the other two VIGVs are at angles of $\vartheta = \pm 24°$ to the central VIGV's axis. Hence, the VIGV profile coordinates need to be transformed to the VIGV coordinate system using

$x\prime = \mathrm{x}$
$z\prime = z \cdot \cos\vartheta + y \cdot \sin\vartheta$
$y\prime = -z \cdot \sin\vartheta + y \cdot \cos\vartheta$

before computing the oscillation around the VIGVs' rotational axes. The displacements are then calculated using the VIGV coordinates marked with $\prime$. Afterwards, the displacements in VIGV coordinates need to be transformed back to displacements in absolute coordinates according to

$x = x\prime$
$z = z\prime \cdot \cos\vartheta - y\prime \cdot \sin\vartheta$
$y = z\prime \cdot \sin\vartheta + y\prime \cdot \cos\vartheta$

3.2.3 Time Resolution and Data Sampling

For the transient simulations, a time step needs to be specified.
Having a compressor speed of 18 000 rpm, the blade passing frequency of the scaled rotor with 20 blades as used in the CFX simulation is 6000 Hz.
When resolving 4 times the blade passing frequency the Nyquist-Shannon sampling theorem demands that the sampling frequency be twice as high, resulting in a sampling frequency of 48000 Hz.
In order to have CFX do about 10 time steps per sampling point, the time step needs to be as small as $\frac{1}{480000}$s.
With that, it readily becomes clear that simulating a single rotor revolution of $\frac{1}{300}$s takes 1600 time step iterations.
Having about 6 coefficient loop iterations per time step plus 3 to 6 iterations for the mesh displacement, the computing time goes up rapidly.

Another constraint on the CFX time step is applied by the motion of the mesh:
For avoiding mesh distortion, the specified mesh displacement cannot exceed 5 adjacent elements.
With a VIGV chord length at 92.5% tip radius of about 58.3 mm and the rotational axis of the VIGV being 12.5 mm downstream of the VIGV leading edge, the maximum radius of the VIGV oscillation becomes 45.8 mm.
Assuming the summarized thickness of the 5 mesh elements closest to the VIGV wall to be about 0.1 mm, the maximum oscillation angle per time step can be calculated using

$\alpha_{max\,timestep} \leq \arcsin\left(\frac{0.1}{45.8}\right)$ and therefore $\alpha_{max\,timestep} \leq 0.13°$

Taking the time step based on the desired sampling rate of 48000 Hz and for an oscillation frequency of 1600 Hz, we obtain $\alpha_{max\,timestep} \approx 0.01°$ which is only one tenth of the allowed value.
Hence, the above time step of $\frac{1}{480000}$s results in small enough displacements and can be used without violating the mesh distortion requirement.
Table 3.3 summarizes the time resolution data for the transient simulation of the Oscillating VIGVs:

Table 3.3: Time resolution for Oscillating VIGVs

		Period	Frequency
Rotor Revolution	t_{rev}	$\frac{1}{300}$s	300 rps
Blade Passing	t_{bp}	$\frac{1}{6000}$s	6000 Hz
Transient Result Sampling	t_s	$\frac{1}{48000}$s	48000 Hz
CFX Time Step	t_{cfd}	$\frac{1}{480000}$s	480000 Hz

Concerning the total time of the transient simulations, there are two conflicting challenges. The first one is to run the simulations long enough to sample sufficient data, the second one is to limit the computing time.
Here a compromise needs to be found since less data results in a coarser frequency resolution when it comes to the analysis of the blade forces. This point will be further discussed in the following chapters.
In general, steady state simulations[10] were run until the solution converged, transient simulations were run until they reached pseudo-equilibrium state before starting to sample transient results, record transient statistics and monitor the blade forces.

3.2.4 Specifying the Excitation

Since the numerical model includes only one fifth of the compressor annulus, the number of interblade phase angles and traveling wave patterns that can be simulated is limited.
Periodic boundary conditions are applied in circumferential direction, hence the traveling wave pattern in the simulation needs to be closed, i.e. complete cycles need to be modeled.
Having 3 out of 15 VIGVs included in the numerical study, either 0 or 5 nodal diameters can be excited.
Therefore, it was agreed to use a 5 nodal diameters forward traveling wave resulting in phase angles of 120° for the VIGV oscillation.
Figure 3.4 shows the onset of the VIGV oscillation where the uppermost VIGV in Figure 3.3 starts first with the oscillation.
One third of the oscillation period later, the central VIGV starts to oscillate. Two thirds of the oscillation period after the first VIGV started, the last VIGV begins with the oscillation before the whole pattern is repeated.

[10] used as initial values for the transient simulations

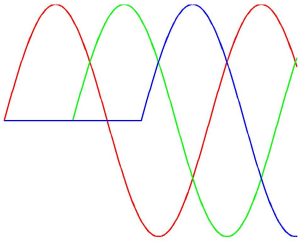

Figure 3.4: Onset of VIGV oscillation with 5 nodal diameters forward traveling wave

To simulate 5 nodal diameters instead of 3 as is planned for the real compressor, the excitation frequency also needs to be adapted.
For exciting the rotor blades with 600 Hz[11], the oscillation frequency can be calculated using equation 2.1 $f = \frac{\Omega}{60} \cdot n + \omega$ which returns $f = 2100$ Hz for 5 nodal diameters.

Hence, the VIGV oscillation study can be summarized as follows:

- Traveling wave pattern: 5 nodal diameters forward traveling wave with $\varphi = 120°$
- Excitation frequency in stationary frame: 2100 Hz
- Excitation frequency in rotor frame of reference: 600 Hz
- Excitation amplitude: 0.5° VIGV oscillation

3.3 Results

3.3.1 Impact on Mean Flow

The aerodynamic criteria with which the excitation systems are to be evaluated were listed in the preceding chapter as:

- Achievable excitation frequency and phase controllability
- Achievable excitation amplitude
- Impact on mean flow

Frequency and phase controllability as well as excitation amplitude will be addressed in the following section when analyzing the blade forces.
The effect the VIGV oscillation has on the mean flow can be most clearly seen when comparing the compressor flow field without oscillation against the compressor flow field with oscillation. Two contour plots showing snapshots of the compressor flow fields are given in Figure 3.5 and Figure 3.6.

[11] For R6 design loop 1, the 1F frequency was 588 Hz as specified in Table 2.2.

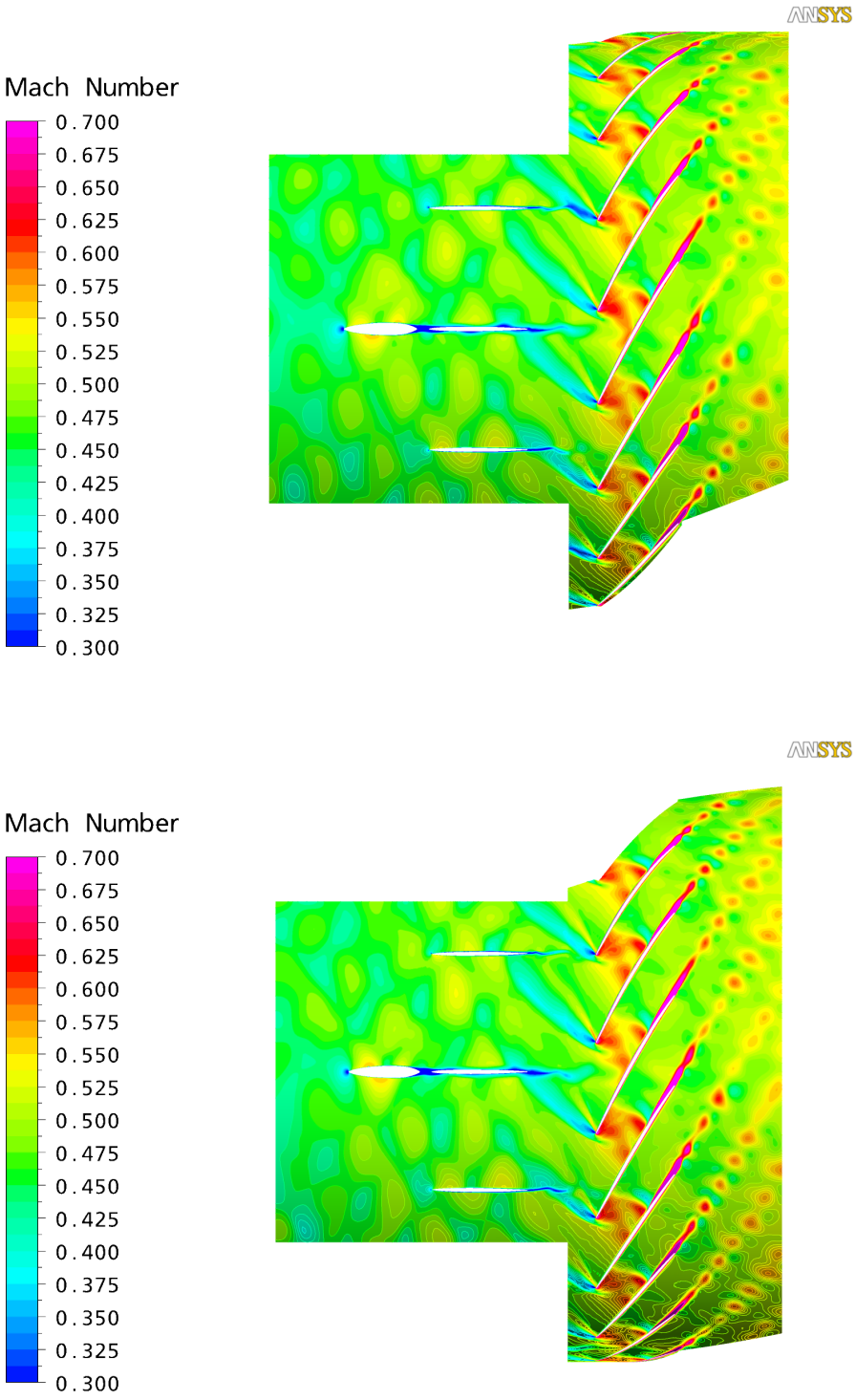

Figure 3.5: M_{stn} for no excitation (top) and for 0.5° VIGV oscillation (bottom)

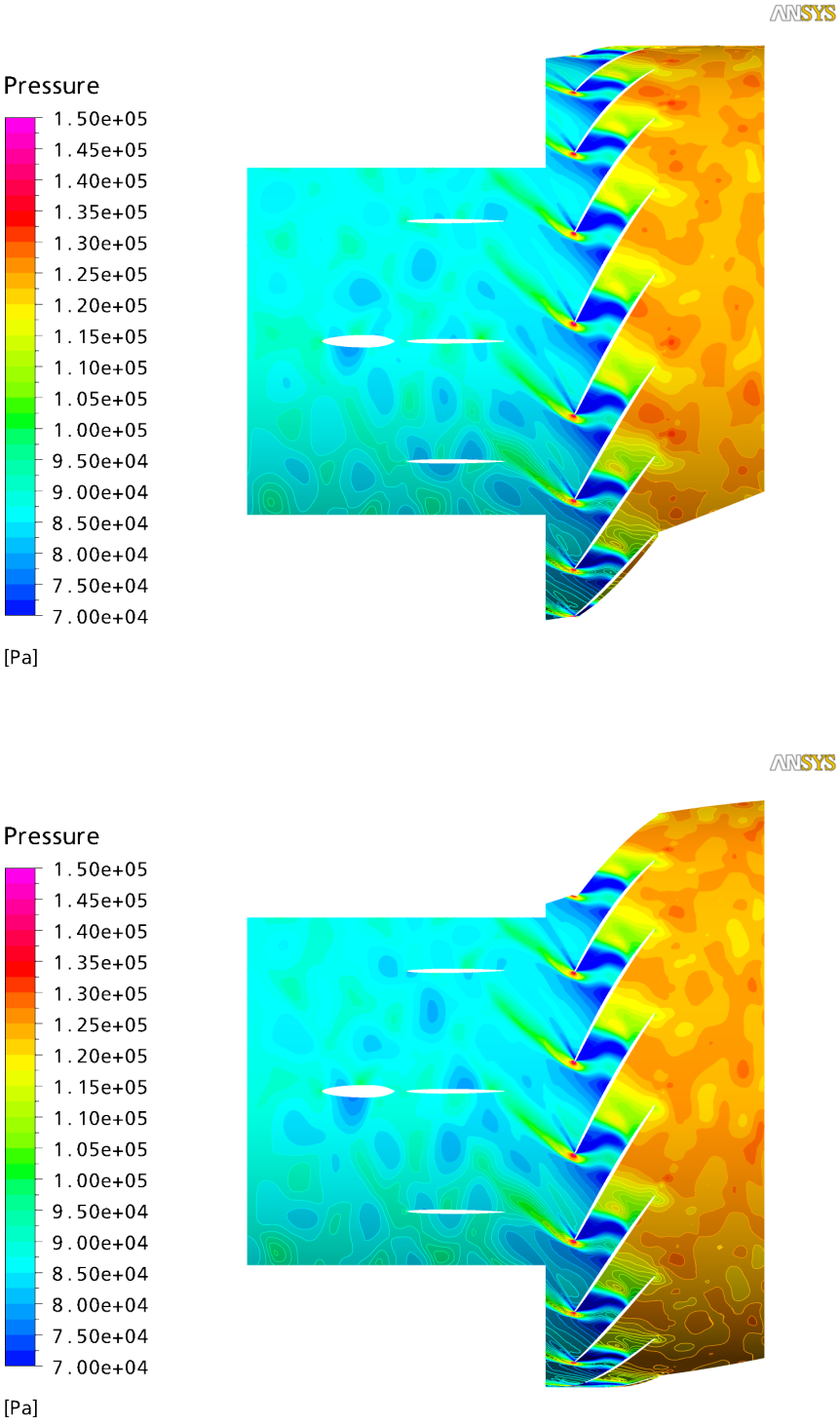

Figure 3.6: p_s for no excitation (top) and for 0.5° VIGV oscillation (bottom)

In Figure 3.5[12], the plotted variable is the Mach number in the stationary frame with a range of 0.3 to 0.7.
When comparing the Mach number contour plot without excitation against the Mach number contour plot with excitation, basically no difference can be observed.
Even the wakes of the VIGVs, where the excitation is actually introduced into the compressor flow field, seem to be completely unaffected by the VIGVs' oscillating motion. The perceivable fluctuation of the VIGV wakes is present in both cases and does therefore not result from the VIGV oscillation.
No pattern caused by the traveling wave can be observed, the flow fields inside the rotor passages seem exactly identical.

The contour plots of the static pressure as shown in Figure 3.6 lead to the same conclusion. Plotted is the static pressure with a range of 0.7 to 1.5 bar.
The flow fields of the SV Domain seem to be absolutely identical. The same is valid for the rotor domain.
That the oscillation of the VIGV has basically no impact on the flow field in the rotor is also confirmed when looking at the shock patterns.
No matter whether the VIGVs are oscillating or not, the shock pattern remains unimpressed. Neither the shocks at rotor leading edge nor the shocks in the blade passage move when the VIGVs oscillate.

Hence, it can be concluded that oscillating the VIGVs with 5 nodal diameters, an oscillation amplitude of 0.5° and an oscillation frequency of 2100 Hz does not have a significant impact on the mean flow inside the compressor domain.

Contour plots of corresponding time averaged static pressure and Mach number are shown in the appendix in Figure 8.2.

3.3.2 Rotor Blade Forces

The rotor blade forces as a result of pressure and viscous forces were recorded using the CFX monitoring function. The rotor blade force sampling rate was therefore equal to the time step.
This data was then imported to MATLAB and Fourier transformed using the built-in standard Fast Fourier Transform function.
The single-sided amplitude spectrum for the forces on rotor blade 4[13] is plotted in Figure 3.7.

As before, the force on blade 4 is plotted once for the case without VIGV oscillation (red) and once for the case with oscillating VIGVs (green) as specified in the previous section.

[12] For improving the visibility of the compressor flow field, 8 blade passages are shown even though only 4 were simulated.
[13] Blade 4 is the uppermost blade as shown in Figure 3.3

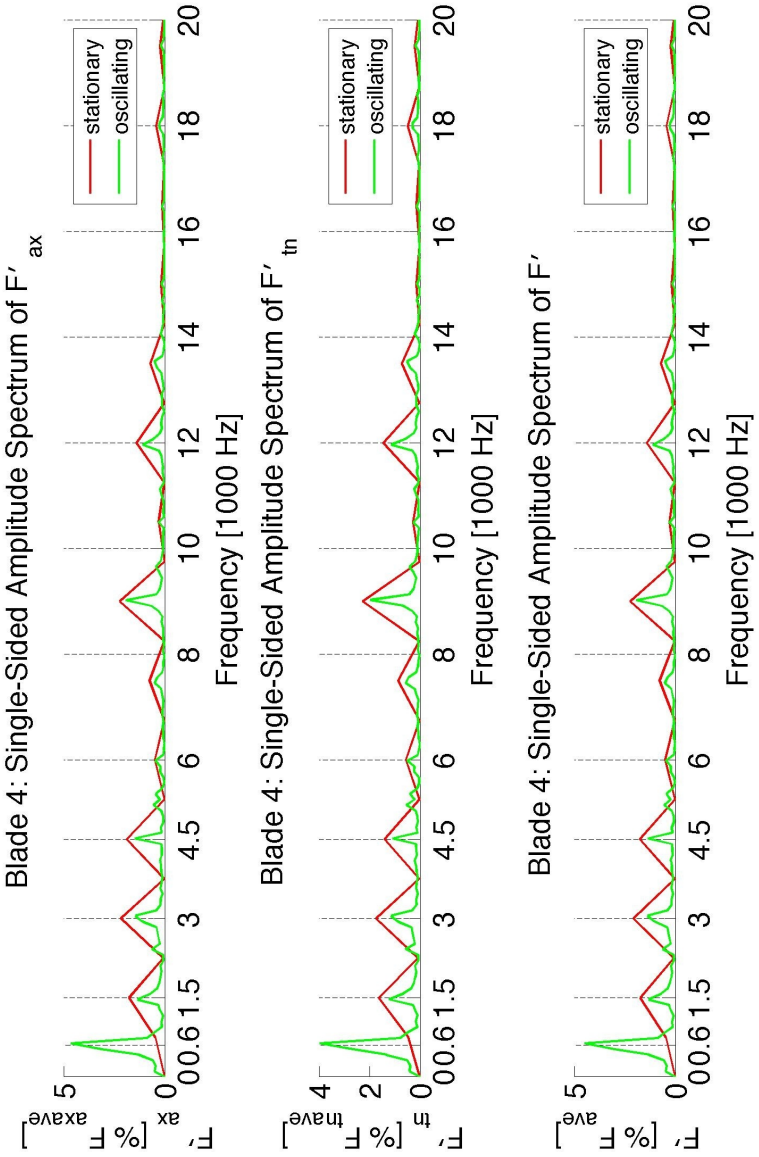

Figure 3.7: Oscillating VIGVs: Forces on rotor blade 4

Shown are the force fluctuations in axial and in tangential direction as well as the total force. All forces have been normalized using the time averaged blade forces.
The blade mean forces are summarized in Table 3.4. In order to obtain the forces in N/mm, the recorded blade force was divided by the 0.05mm thickness of the CFX setup.

Table 3.4: Time averaged forces on rotor blade 4

$F_{axial\,ave}$	-1.77 N/mm
$F_{tangential\,ave}$	1.06 N/mm
F_{ave}	2.06 N/mm

When looking at the force oscillations for the non-oscillating VIGVs as shown in Figure 3.7 in red, we can readily see the peaks for the fifth engine order, i.e. the struts at 1500 Hz, the second harmonic of the struts at 3000 Hz as well as the fifteenth engine order, that is the VIGVs, at 4500 Hz. The second harmonic of the VIGVs at 9000 Hz is also clearly visible. Besides, combinations thereof can be observed.[14].

For the finer resolved[15] case with the oscillating VIGVs shown in green, we obtain the predicted distinct peak for the excitation frequency in the rotor frame of reference at 600 Hz. With an amplitude of about 5% blade mean force, the excitation level is rather moderate. Nevertheless, the peak is sharp and dominant and the excitation based upon oscillating VIGVs can be considered clean.
This remains true when it comes to the higher harmonics of the excitation frequency, since no other distinguished peaks related to the VIGV oscillation can be perceived.
Other than that, the peaks for the struts at 1500 Hz, the peak for the corresponding second harmonic and the VIGVs at 4500 Hz can be identified.
Again, the peak for the second harmonic of the VIGVs at 9000 Hz is also distinctly visible.

It can be concluded, that the excitation system concept based upon oscillating the VIGVs is feasible from the aerodynamic point of view.
The impact on the mean flow is diminishing, the compressor flow field is not disturbed.
The excitation level is with about 5% blade mean force moderate, but since the oscillation of the VIGV would affect the entire span it still seems doable.
Due to the mechanical limitations of the VIGVs, the concept still remains impractical and is therefore only used as reference case.

[14] Due to computing time constraints, the simulation without VIGV oscillation was only run for 2 pitches or 8 blade passings. Hence, the frequency resolution for this case is rather coarse. Nevertheless, the data shows the expected peaks and the amplitudes agree well with the finer resolved case with VIGV oscillation.
[15] Here, the data was sampled over two entire rotor revolutions, i.e. 10 pitches.

4 Rotating Cylinders

As it was outlined before, an excitation system based on an oscillating motion of the VIGVs is not feasible due to mechanical limitations.
When looking for the underlying cause leading to the mechanical problems with the VIGV oscillation, it will be found in the large inertia of the VIGVs and in the nature of the motion.

Utilizing a rotation instead of an oscillation, the above mentioned problem can already be partially overcome since the mass would not have to be accelerated in inverse directions.
For obvious reasons it is useless to rotate the VIGVs. Hence, it was proposed to rotate separate profiles for generating the excitation.
These profiles would not have to penetrate the entire span, but be introduced at the tip region only where they would achieve the largest effect.

4.1 Cylinder Parameter Study

Since little was known about how rotating profiles would act on the flow and if they would actually bring the desired excitation level, a separate study was set up to find a feasible rotating cylinder concept as well as the most promising cylinder design.

4.1.1 Cylinder Designs

For being able to use rotating cylinders as excitation system, the cylinders need to have specific design features to create periodic flow disturbances.

The first proposed design was slotted cylinders.
When rotating these cylinders with a certain rotational speed, the slot would either open or shut to the main flow and therefore generate the desired periodic flow perturbations.

Based upon this idea, a second concept was proposed utilizing cylinders with multiple slots, e.g. cylinders with crossed slots in order to bring down the required rotational speed for achieving the same excitation frequency.

Inverting this concept, slender profiles were suggested that - depending on their orientation towards the main flow - would either create blockage regions or be basically invisible to downstream components.

Summing up, the following cylinder designs were proposed and are further described in the following sections:

- Slotted Cylinders with varying slot size
- Crossed Cylinders
- Elliptic Cylinders with varying radii ratios

For maintaining a good comparability between the different cylinder designs, all cylinders were given the same maximum diameter.
As a initial guess, 5 mm was proposed which is about twice the maximum profile thickness of the VIGVs. Assuming that 1 mm cylinder diameter would probably be too small to create the desired effect and a 10 mm cylinder might cause blocking problems, the 5 mm diameter was chosen as the intermediate value.

Figure 4.1 shows the designs of the studied cylinder shapes. The upper row shows slotted cylinders with increasing slot size. The slot sizes range from 1 mm to 3 mm.
The leftmost cylinder in the bottom row features crossed slots with a slot width of 1 mm.
The remaining two cylinders in the bottom row are elliptically shaped with radii ratios of 3 to 1 and 2 to 1, respectively.

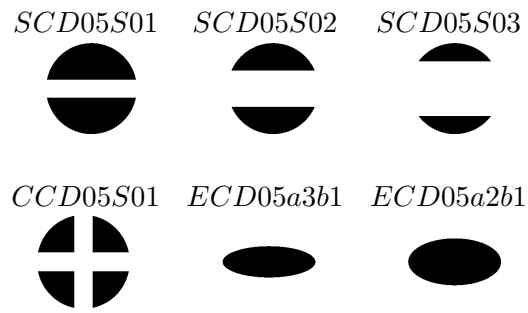

Figure 4.1: Investigated cylinder designs

4.1.2 Achievable Frequencies and Excitation Levels

Mesh Setup for Cylinder Design Study

In order to be able to analyze the different cylinder designs while still keeping the computational effort low, a separate numerical simulation was set up.
The mesh shown in Figure 4.2 was again generated as structured hexahedral volume mesh with ANSYS ICEM CFD. The displayed mesh is twice the actual mesh and was used that way for being able to investigate counter rotating cylinders as well.
To enable the incorporation of the different cylinders into the same outer domain, a round

interface was spared in the center with a diameter of 30 mm or 6 times the cylinder diameter. The large diameter was used with the intention to keep the interface away from where the flow perturbations are generated.
In circumferential direction, the mesh extends 73.6 mm which is $\frac{1}{15}$th of the compressor annulus at 92.5% tip radius[1]. With 15 exciters being finally integrated into the compressor domain, the distance between the cylinders is representative.
Referring to the rotational axis of the cylinders, the mesh extends 50 mm in upstream direction and 100 mm or 20 cylinder diameters in downstream direction.
The mesh for the cylinders is simply defined as an O-grid mesh with hyperbolic node distribution along the cylinder walls. In normal direction, vertices are periodic.

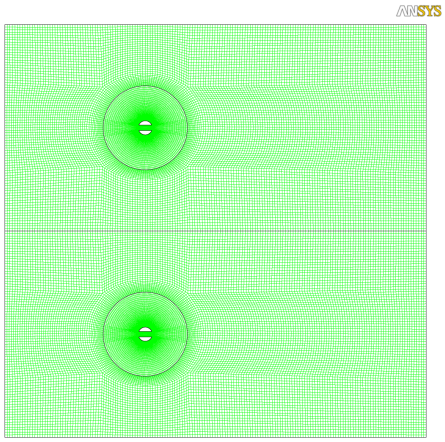

Figure 4.2: Mesh for cylinder design study, here with SCD05S02

Table 4.1 summarizes the mesh statistics as used for investigating the different cylinder designs[2].

Table 4.1: Mesh statistics for cylinder design study

	Outer Domain	Inner Domain
Nodes	2 x 44000	2 x 26000
Elements	2 x 56000	2 x 33000
Layers	2	2
Min. Angle	54°	72°
Determinant	0.9-1	0.9-1
Max. Aspect Ratio	40	27
Max. Volume Change	1.6	2
Average(y^+)	−−	< 22 (< 8)

[1] The mesh as displayed in Figure 4.2 shows the $\frac{1}{15}$th mesh twice.
[2] The simulation has also been run with a refined mesh with an average(y^+) of below 8 leading to the same results.

Solver Setup for Cylinder Design Study

As for the original model, ANSYS CFX was used to run the numerical simulation.
At the domain inlet, the boundary condition is identical to the one used for the compressor setup with the values shown in Table 4.2.
Here, two different boundary conditions are given for the domain outlet[3]. In order to assure that the boundary condition at the outlet does not affect the quality of the results, two independent simulations have been run. The first simulation with normal velocity boundary condition at the outlet, the second simulation with static pressure boundary condition at the outlet. The results for both simulations agree.
The bottom and top surfaces of the domain were specified as free-slip walls[4].
In circumferential direction, the interfaces have been defined as translational periodic with 1 to 1 mesh connection. All cylinder walls were set to standard no-slip walls.
The interface between the rotating inner cylinder domain and the stationary outer domain was specified as transient rotor-stator interface.
For the steady state simulations that were run to obtain the initial values for the transient simulation, the interface was set to frozen rotor[5].

Table 4.2: Boundary conditions at inlet and outlet

	Domain Inlet	Domain Outlet
Total Pressure p_t	101325 Pa	–
Total Temperature T_t	288.15 K	–
Turbulence Intensity	5%	–
Velocity c_{ax}	–	153.5 m/s
Static Pressure p_s	–	86311 Pa

As for the Oscillating VIGVs simulation, the used turbulence model is the Shear-Stress-Transport model and the heat transfer was set to Total Energy including viscous term.

Other than for the compressor simulation with Oscillating VIGVs, the excitation frequency for this simplified study was set to 1600 Hz[6].
For all of the above listed cylinder designs with the exception of the crossed cylinders, this excitation frequency transforms to a cylinder rotational speed of 800 rps. For the crossed cylinders, this value is halved to 400 rps since 4 excitation cycles per revolution are completed.
Aiming for a time step resolution of about 1 time step per 0.5° cylinder rotation, the simulation time step was hence defined as $\frac{1}{576000}$s.

[3]The outlet boundary condition was specified according to the conditions at rotor inlet.
[4]Since this setup is a planar one, the simulation was also run with symmetry boundary condition at bottom and top surface. The results were found to be identical.
[5]For a 360° interface as shown in Figure 4.2, a stage interface cannot be used.
[6]1600 Hz is the original frequency requirement. For the Oscillating VIGVs the frequency was changed to 2100 Hz to match the 5 nodal diameters.

The transient results were sampled every 10 time steps equivalent to a sampling frequency of 57600 Hz or 1 per 5° cylinder rotation.
During all simulations, the data was sampled for at least 2 complete cylinder revolutions equivalent to 4 excitation cycles for all but the crossed cylinders. For the crossed cylinders, this transforms to 8 excitation cycles. Except for the setup with counter rotating cylinders, all cylinders rotate counterclockwise.
A summary of the time resolution is given in Table 4.3.

Table 4.3: Time step and data sampling for cylinder design study

		Period	Frequency
Cylinder Revolution	t_{rev}	$\frac{1}{800}$s	800 rps
Transient Result Sampling	t_s	$\frac{1}{57600}$s	57600 Hz
CFX Time Step	t_{cfd}	$\frac{1}{576000}$s	576000 Hz

Rotating Cylinder Flow Fields

Figure 4.3 shows the time averaged Mach number contours for the investigated cylinder designs[7]. The Mach number is plotted in the range of 0.2 to 0.6.
Figure 4.4 displays the corresponding contour plots of the time averaged static pressure in the range of 0.7 to 1 bar.

The wakes look similar for all of the cylinders, with the trend to become somewhat stronger for the more aggressive profile shapes like the elliptic cylinders.
The Magnus effect caused by the cylinder rotation is hardly observable due to the high Reynold's number[8] of the flow. The difference between the flow fields of the counter rotating slotted cylinders and the regular rotating cylinders is therefore diminishing. Hence, using counter rotating cylinders to keep the induced tangential velocity component small is unnecessary.
The results for the counter rotating cylinders are given in the appendix.

More information is obtained when looking at the instantaneous flow field that reveals the periodic pattern of the vortex shedding caused by the cylinder rotation.
Figure 4.5 shows the static entropy over one excitation cycle[9] with a snapshot taken every 30° or $\frac{1}{9600}$s. The entropy is plotted in the range of -25 to 0 $\frac{J}{kgK}$.
The correlation between vortex shedding and cylinder orientation can be readily seen.

[7] The pattern that can be observed in the inner domain around the cylinders is caused by the time averaging in a rotating domain.
[8] based on cylinder diameter, $\mathrm{Re}_d = 49000$
[9] equivalent to one half cylinder revolution or $\frac{1}{1600}$s

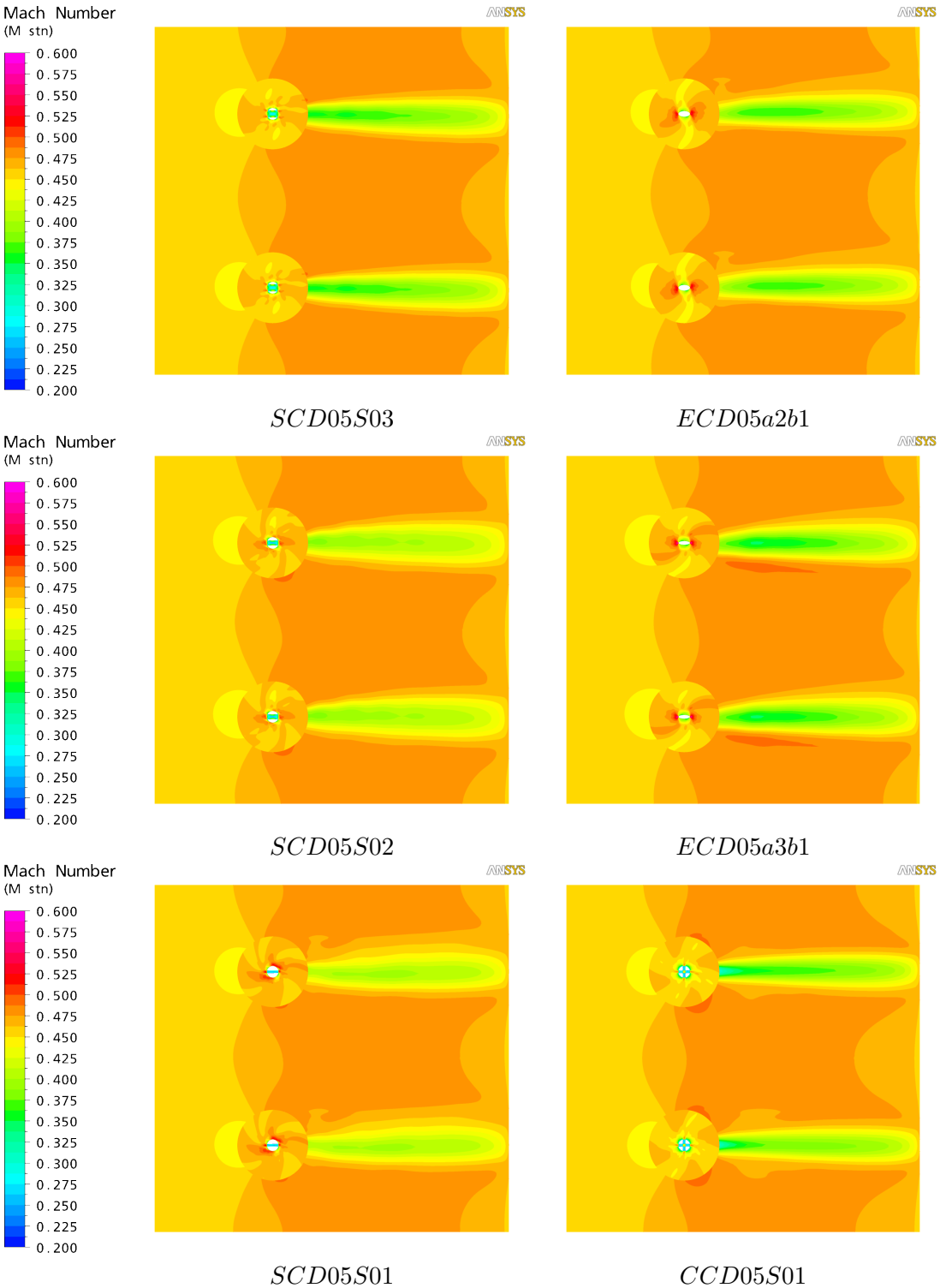

Figure 4.3: Time averaged M_{stn} for cylinder design study

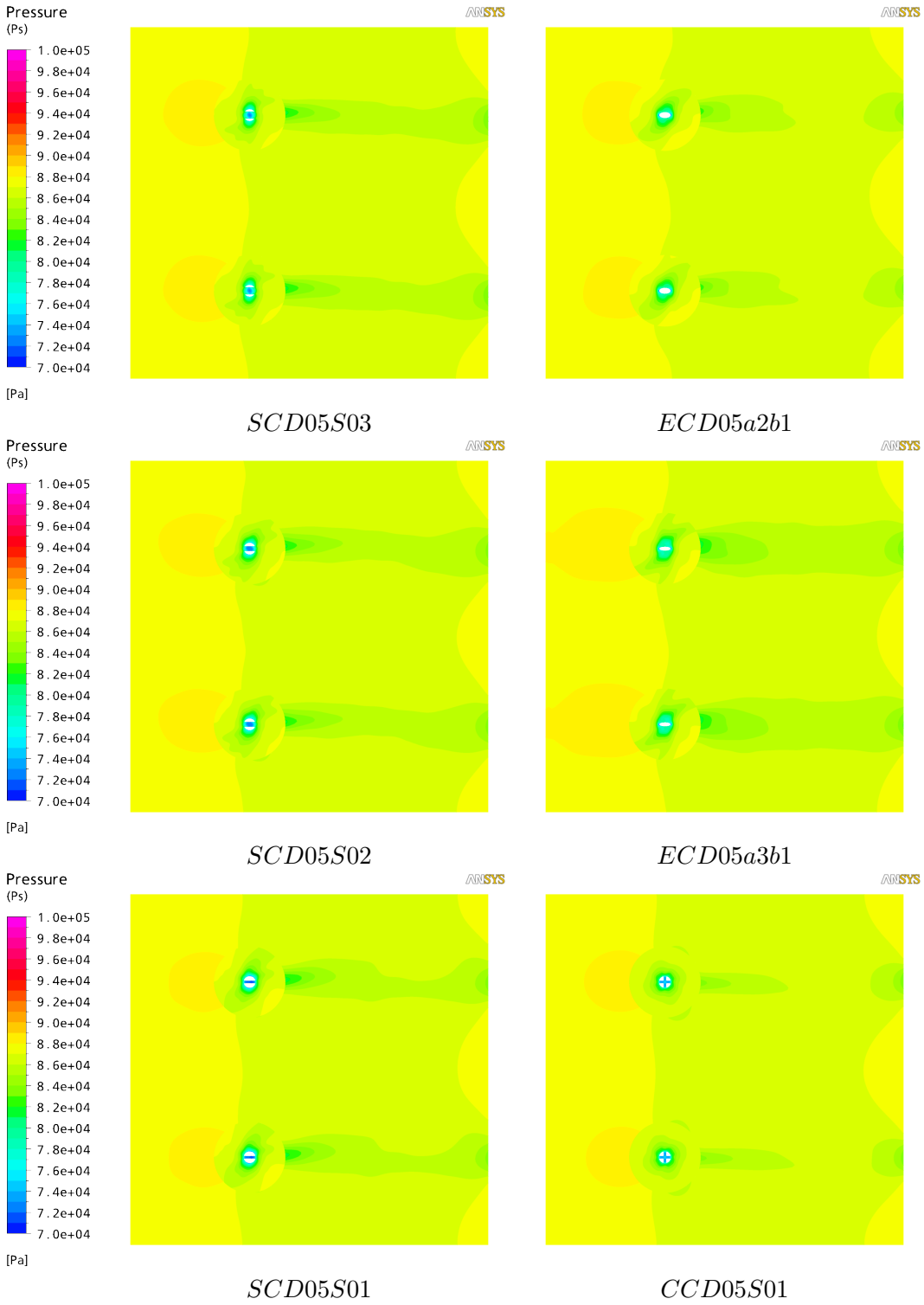

Figure 4.4: Time averaged P_s for cylinder design study

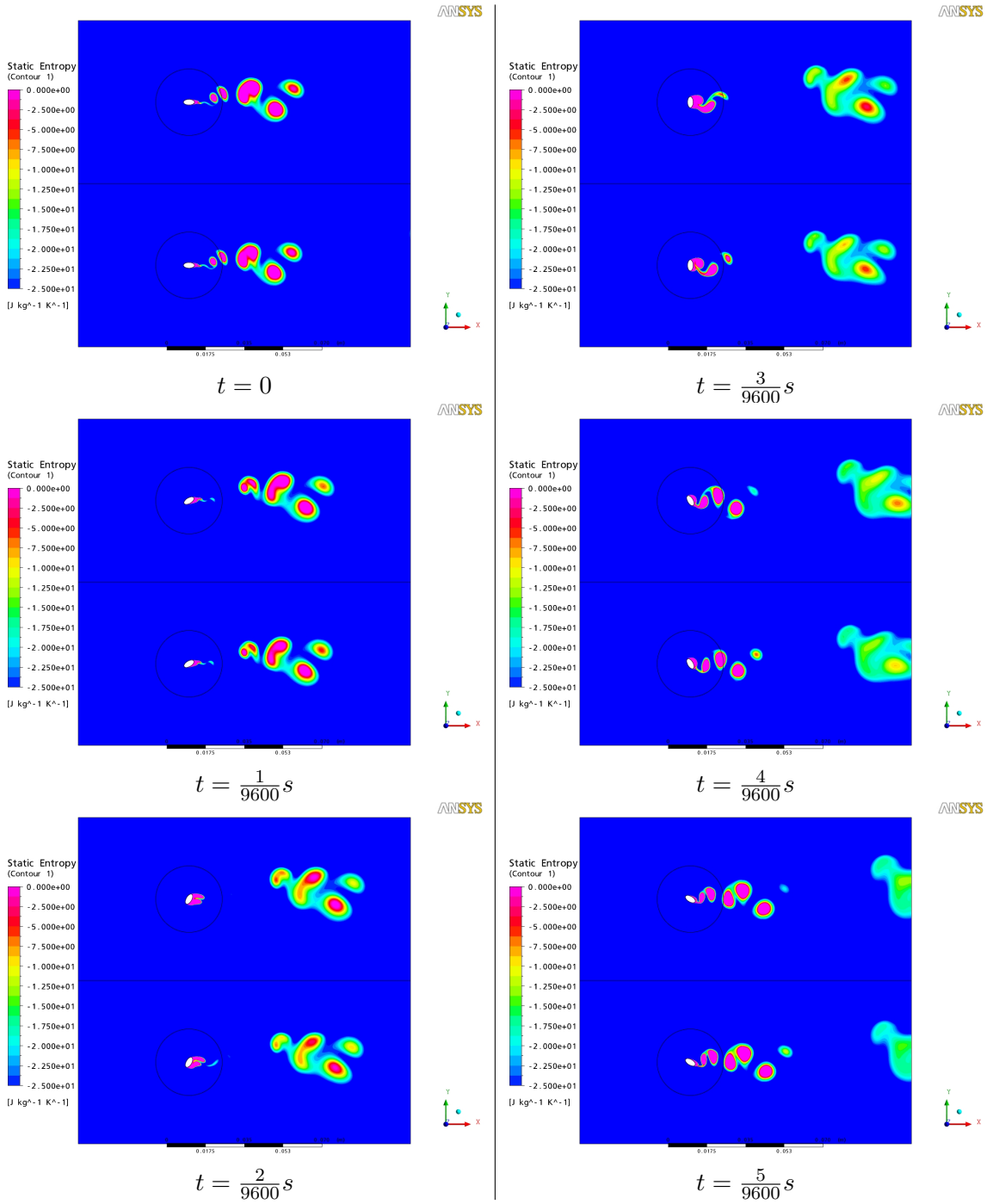

Figure 4.5: ECD05a2b1: Snapshots of static entropy over one excitation cycle

Excitable Frequencies

For investigating whether the rotating cylinders are capable of achieving the desired excitation frequency of 1600 Hz[10] in the stationary frame, the induced velocity fluctuations have been extracted from the transient results, i.e. u' and v'.
The data was extracted at lines 6, 12 and 18 diameters downstream of the cylinder rotational axis as shown in Figure 4.6.
The fluctuations of u' and v' have then been transformed to the frequency domain using the standard MATLAB Fast Fourier Transform.
The FFT was either applied on points aligned with the cylinder wake (blue cross[11]) or on points $\frac{1}{4}$th domain width off center (red cross).

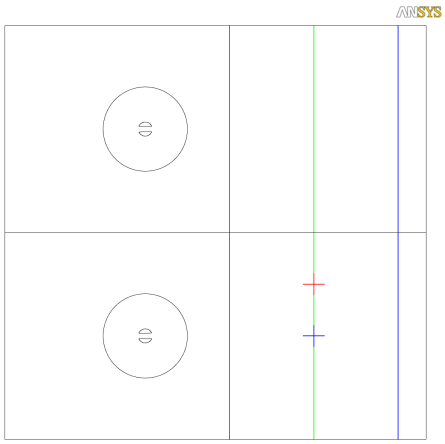

Figure 4.6: Lines used for sampling transient data

Summarizing, it can be stated, that all concepts are capable of exciting 1600 Hz, but to different amplitude levels. Moreover, the cleanliness of the excitation with regard to higher harmonics and noise content was differing significantly.
The most promising design was found to be an elliptical cylinder profile.
For all other cylinder designs, either the amplitudes for the desired excitation at 1600 Hz were much smaller or the signal to noise ratio with regard to higher harmonics was worse.
The FFT results for the non-elliptic cylinder designs are given in the appendix in Figures 8.4 thru 8.8.

For both elliptic profiles, the one with a radii ratio of 2 and the one with a radii ratio of 3, comparable results were obtained.
Hence, the thicker profile was chosen for its improved robustness against self excitation.
The FFT results for the elliptic cylinder design with a radii ratio of 2 are given in Figure 4.8[12]. Velocity fluctuations were analyzed 6, 12 and 18 diameters downstream of the cylinder

[10] This is the real frequency requirement, not the modified one to match 5 instead of 3 nodal diameters.
[11] point 46 in the graphics refers to the point as marked by the blue cross
[12] The velocities have been normalized with the inlet velocity U_{inf}

center axis.
For u', the elliptic profiles show a dominating peak at the desired excitation frequency of 1600 Hz and a second prominent peak at 3200 Hz, the corresponding second harmonic. The induced velocity fluctuations are as high as 30% inlet velocity, but decay for positions further downstream. All other peaks of u' can be neglected against the superiority of these two peaks. For v', the results are more chaotic due to the vortex shedding involved. Nevertheless, the vortex pattern decays quickly and the chaotic amplitudes diminish for distances of 12 or 18 diameters downstream of the rotating cylinder.

For the outlined reasons, the elliptic cylinders are considered feasible when it comes to inducing a sufficient level of periodic velocity fluctuations.
60 mm or 12 cylinder diameters downstream of the cylinder axis, the excitation can be considered clean with regard to noise. Hence, 12 cylinder diameters between rotor leading edge and cylinder axis seems a promising distance to integrate the cylinders into the compressor domain.
As shown in Figure 4.7 integrating cylinders with a length of 20 mm[13] and a diameter of 5 mm wouldn't interfere with a rotation of the VIGVs of up to ±30°.
In the next step, the phase controllability of the concept is investigated.

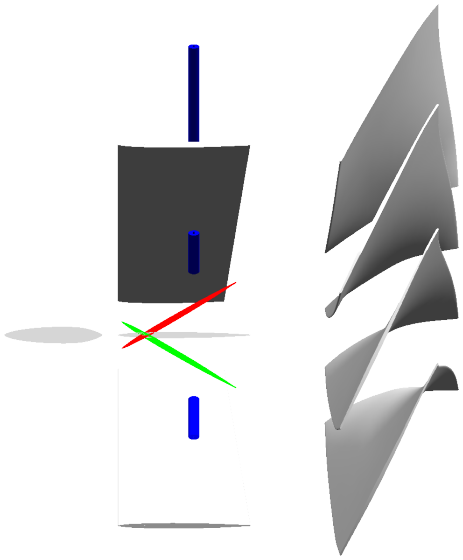

Figure 4.7: Integrability of rotating cylinders

[13]In Figure 4.7, the shown cylinder length is 50 mm.

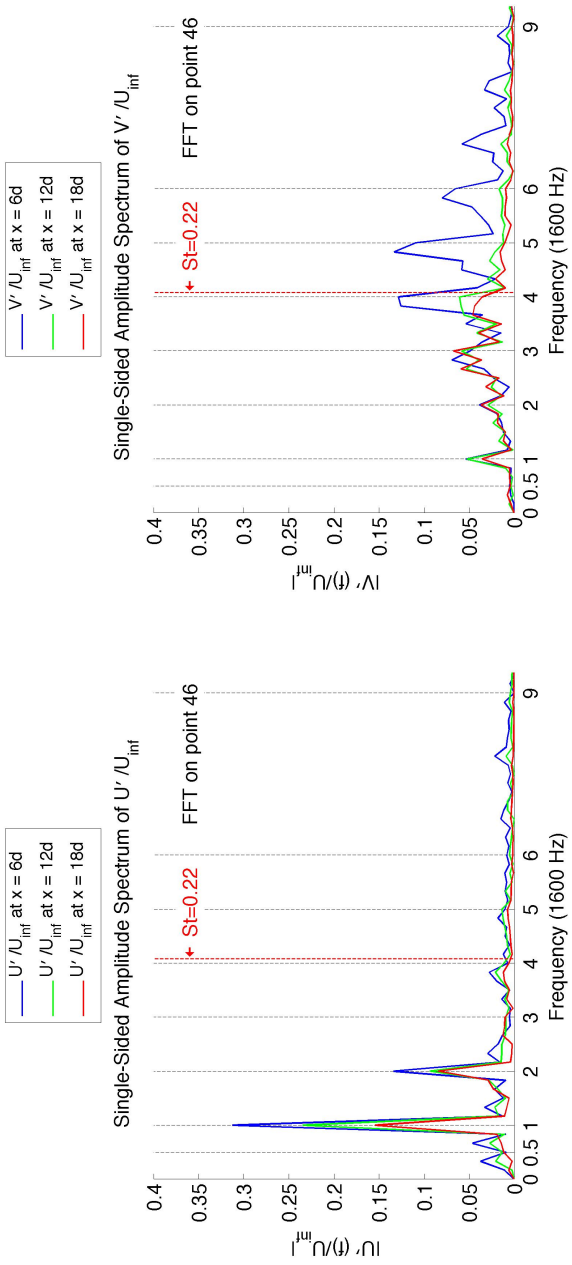

Figure 4.8: ECD05a2b1: FFT of velocity fluctuations induced by cylinder rotation (Point 46)

4.2 Phase Controllability

Having seen that the elliptic cylinder design seems capable of exciting the rotor blades by inducing periodic velocity fluctuations with a frequency of 1600 Hz, the phase controllability of the concept was investigated.

Therefore, a new simulation was set up with the mesh taken from the previous study. For being able to investigate the phase controllability of a 3 nodal diameters forward traveling wave, the mesh was instance transformed 4 times to obtain the setup as shown in Figure 4.9[14].
As can be seen in the graphic, all elliptic cylinders have a phase difference of $\pm 36°$ towards their neighboring cylinders[15]. With two excitation cycles per revolution, this transforms to an excitation phase angle of 72° as illustrated on the left of the graphic. Having thus modeled one nodal diameter with 5 cylinders, 15 elliptic cylinders with identical phase angles would excite 3 nodal diameters in the real compressor.

Figure 4.9 also shows lines at 6, 12 and 18 cylinder diameters downstream of the cylinder axes used for extracting the transient data, i.e. the velocity fluctuations.
Moreover, points 46, 136, 226, 316 and 406 are indicated where the data used to analyze the phase angle as actually induced by the cylinder rotation was recorded.

The results of the phase controllability analysis are shown in Figure 4.10. The velocity history was recorded on the above mentioned points with a time step of $\frac{1}{640000}$s resulting in an accuracy of $\pm 2.25°$. The analysis was done in MATLAB with the standard FFT function.
The phase of u' between neighboring cylinders lies in the range of 69° to 74° and is hence accurately controlled.
This looks differently for the phases of v' and p'. Counted from the bottom, the v'-phase between cylinders 1 and 2 is as high as 86°, whereas it is only 54° between cylinders 4 and 5.
The same variation can be observed for p', the phase of which varies between 50° and 70°.
Sampling the data for more than two excitation cycles probably leads to improved results due to the averaging of the statistical - since turbulent - behavior of v'.

Figure 4.11 shows the FFT results of the recorded transient data along Line 2.
The results agree well with the results given in Figure 4.8.
For v' it can be observed that each cylinder shows two 1600 Hz peaks a little off the cylinder wakes. Directly in the wake, the peak lies at 3200 Hz.
This is caused by the vortex shedding from both cylinder sides.

[14]The circles surrounding the cylinders mark the interface between rotating and stationary domain.
[15]The cylinders shown in Figure 4.9 are rotating in counterclockwise direction.

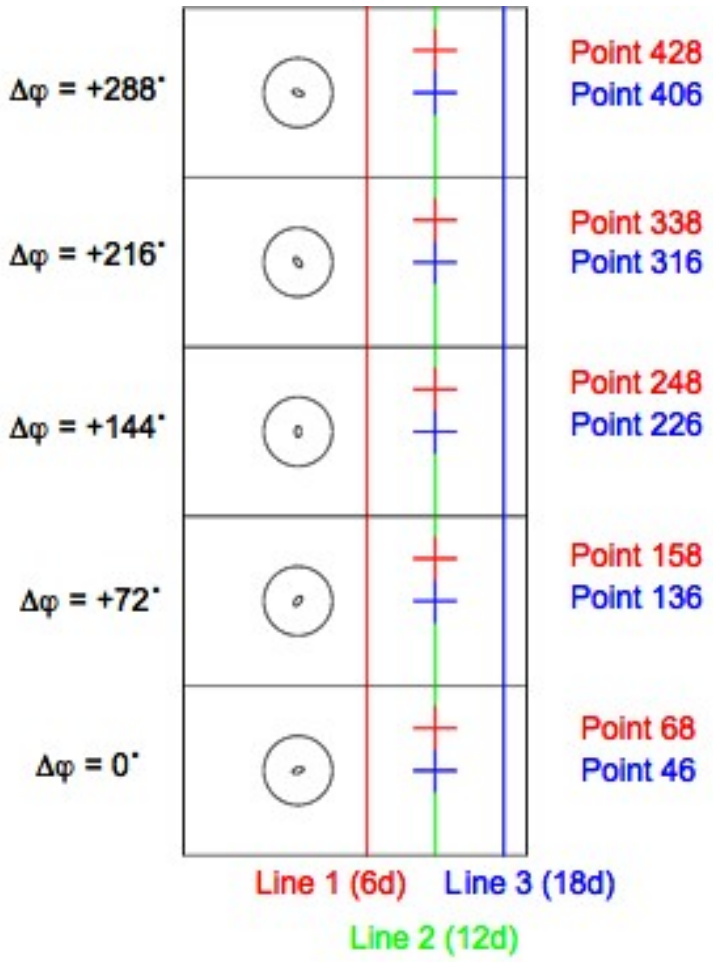

Figure 4.9: ECD05a2b1: Phase controllability setup

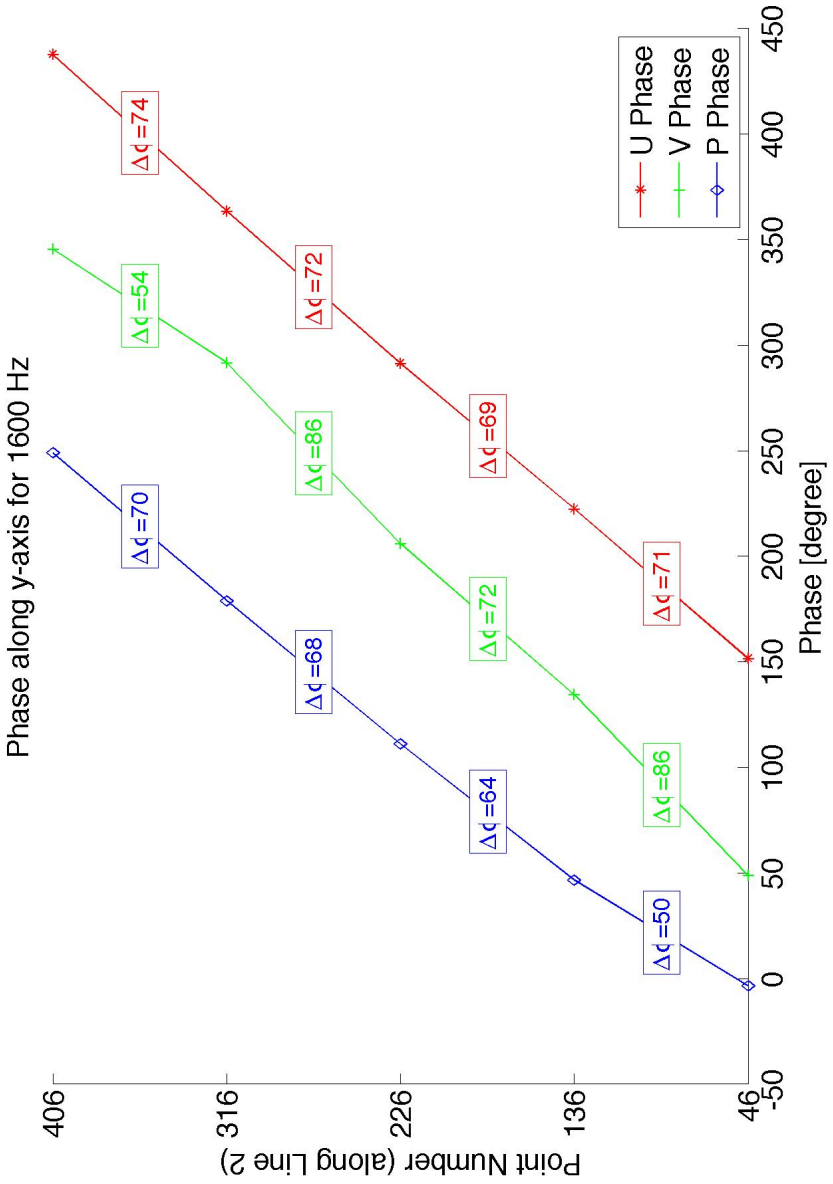

Figure 4.10: ECD05a2b1: Phase controllability analysis

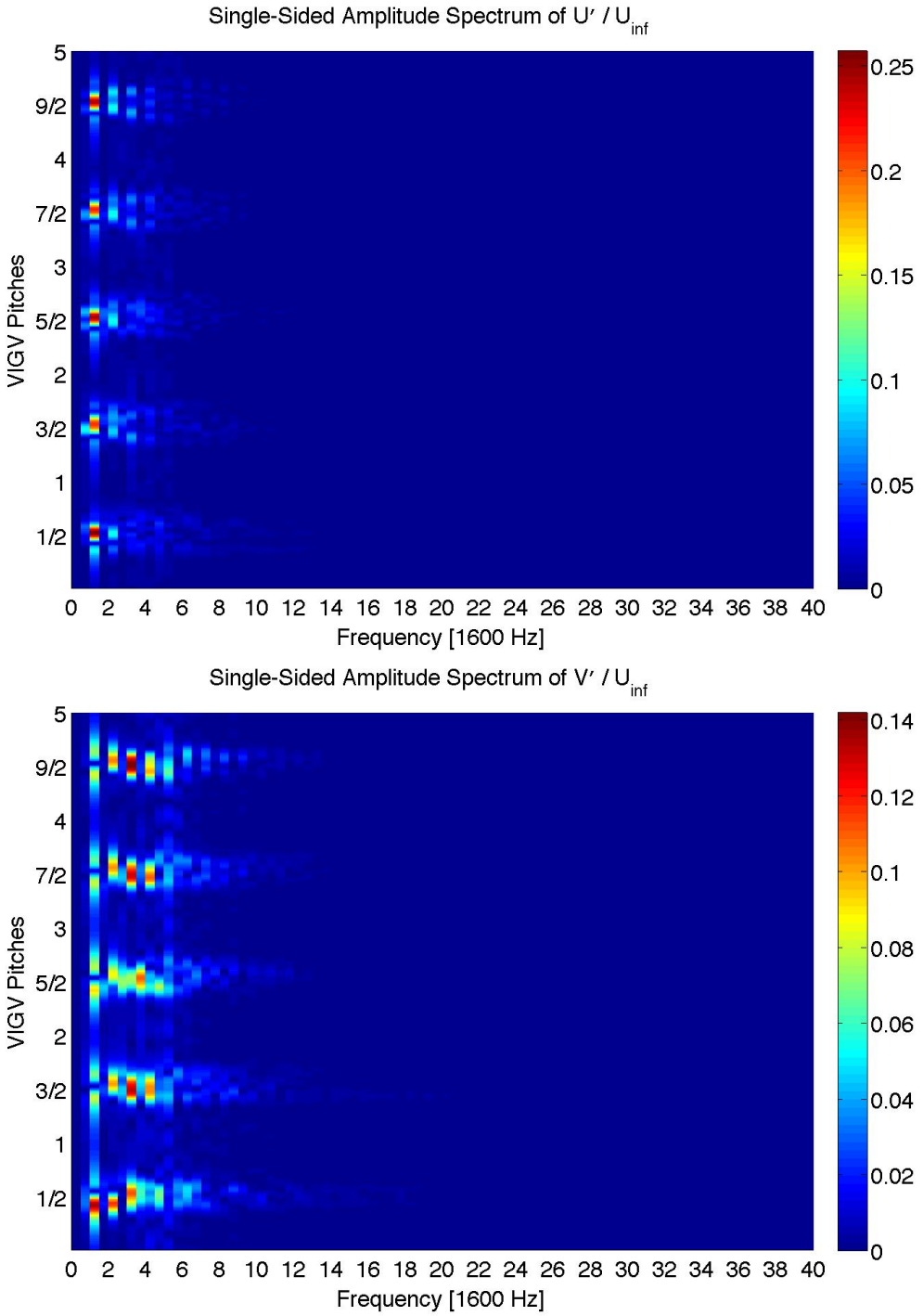

Figure 4.11: ECD05a2b1: FFT of u' and v' along Line 2

4.3 Elliptic Profiles: ECD05a2b1

4.3.1 Mesh Setup

For being able to investigate the applicability of elliptic cylinders as excitation system for the forced response campaign, the cylinders need to be incorporated upstream of the rotor into the compressor domain.
As described in the previous sections, 60 mm or 12 cylinder diameters upstream of the rotor leading edge was found to be a promising distance[16].

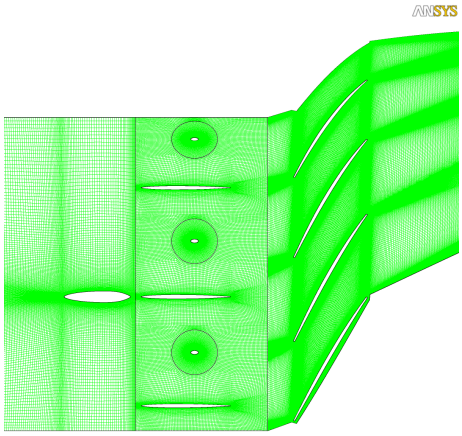

Figure 4.12: Hexahedral mesh as used for Rotating Elliptic Cylinders

Therefore, the strut and VIGV domain as used for the Oscillating VIGVs was remeshed as two separate domains. The positions of the strut and the central VIGV have been moved outwards to account for the interfaces of the rotating cylinder meshes.
The first domain includes the strut and features $\frac{1}{5}$th of the compressor annulus.
The second domain represents only $\frac{1}{15}$th of the annulus containing one VIGV and one interface for integrating the elliptic cylinders.
O-grids have been defined around the strut, the VIGV as well as the elliptic cylinder domain. Along the strut and VIGV walls, the nodes are again distributed using a hyperbolic distribution law. Around the interface for the elliptic cylinders, nodes are uniformly spaced to account for the cylinder rotation.
The dimensions of the domains in general have not been changed.
In circumferential direction, the nodes satisfy rotational periodicity.
The rotor domain has not been remeshed and was copied from the Oscillating VIGVs without changes.
Once the mesh containing VIGV and cylinder interface was completed, a rotational instance

[16] In TUD coordinates, 60 mm upstream of the rotor leading edge is 292.41 mm upstream of the radial diffuser flange.

transform was applied twice on this domain to obtain the mesh as shown in Figure 4.12[17]. The sections into which the rotating cylinder domains have been integrated can be clearly seen in between the VIGVs. The cylinder mesh is similar to the one used in the preceding section, only that bottom and top surface have been projected onto the 92.5% tip radius duct. Table 4.12 summarizes the mesh quality statistics for front frame and rotor domain of the Rotating Cylinders study with elliptic profiles.

Table 4.4: Mesh statistics for Rotating Elliptic Cylinders

	FF Domain	R Domain
Nodes	230000	4 x 110000
Elements	300000	4 x 150000
Layers	2	2
Min. Angle	23°	22°
Determinant	0.7-1	0.9-1
Max. Aspect Ratio	286	183
Max. Volume Change	3	2.9
Average(y^+)	< 6	< 6.5

4.3.2 Solver Setup

The solver setup is in general identical to the setup used to investigate the VIGV oscillation. Again, ANSYS CFX was used to run the simulations with the boundary conditions as already specified in Table 3.2.

The main difference between the two setups is the additional rotating domain for the elliptic cylinders.
Here, a transient rotor stator interface was specified to model the rotation of the cylinders.
In order to keep the rotating cylinder domain always aligned with the stationary front frame domain surrounding it, a mesh motion was required. For projecting the rotated section of the cylinder duct back onto the actual duct geometry as defined by the 92.5% tip radius, a specified mesh displacement was applied.
The mesh displacement is similar to the mesh displacement used for the Oscillating VIGVs, with the exception that the rotation does not have to be prescribed.
Hence, the mesh is rotated each time step as specified for the rotating cylinder domain and before beginning the coefficient loop iterations, the meshes of rotating and stationary domain are aligned using the projection of the mesh displacement outlined in the previous chapter for the VIGV oscillation.
The time steps for the rotating cylinders simulations are summed up in Table 4.5. To account for the cylinder rotation, the time step had been further reduced to $\frac{1}{600600}$s.

[17] The interface connecting the strut mesh with the three VIGV meshes was then defined as General Grid Interface

The blade forces were recorded for each time step using the monitoring function. Data was sampled for 3 compressor revolutions[18].

Table 4.5: Time resolution for Rotating Elliptic Cylinders

		Period	Frequency
Rotor Revolution	t_{rev}	$\frac{1}{300}$s	300 rps
Blade Passing	t_{bp}	$\frac{1}{6000}$s	6000 Hz
Transient Result Sampling	t_s	$\frac{1}{60060}$s	60060 Hz
CFX Time Step	t_{cfd}	$\frac{1}{600600}$s	600600 Hz

As outlined before, the limitations of the CFX setup don't permit to model the actual excitation with 3 nodal diameters forward traveling wave as to excite the 1F blade mode of R6.

Hence, the cylinder rotation was adapted to generate a 5 nodal diameter forward traveling wave excitation with 2100 Hz in the stationary frame. The cylinders are thus rotating with 1050 rps.
The phase difference between neighboring cylinders is set to 60°, resulting in an excitation phase angle of 120°.
The excitation frequency of 2100 Hz in the stationary frame transforms to 600 Hz in the rotor frame of reference.
The inception of the cylinder rotation is similar to the onset of the VIGV oscillation as shown in Figure 3.4 with the uppermost cylinder starting to rotate first. The bottommost cylinder is following last with an excitation phase angle of 240°.

Accordingly, the excitation using the rotating cylinders can be summarized as

- Traveling wave pattern: 5 nodal diameters forward traveling wave with $\varphi = 120°$
- Excitation frequency in stationary frame: 2100 Hz
- Rotating speed of cylinders: 1050 Hz
- Excitation frequency in rotor frame of reference: 600 Hz
- Excitation amplitude: Dependent on cylinder profile and length

In order to obtain information about the influence of the cylinder diameter on the excitation level, the simulation was run twice, first with the standard cylinder diameter of 5 mm, then with a reduced diameter of 2.5 mm.
In both cases, the elliptic profiles with a radii ratio of 2 to 1 were used.

[18]Transient results have only been saved for specified time steps.

4.3.3 Results

Figure 4.13 thru 4.15 show the results obtained with the 5 mm diameter elliptic cylinders used to generate a 2100 Hz excitation with 5 forward traveling nodal diameters .
Figure 4.15 also includes the results for the blade forces induced by 2.5 mm diameter cylinders.

When looking at the Mach number contour snapshot shown in Figure 4.13, the 5 nodal diameter pattern caused by the 120° phase angle between the cylinders can be clearly seen.
Whereas the vortex shedding marked by the interfering spots of high and low Mach numbers is in full effect for the uppermost cylinder, it has just started for the central cylinder and cannot yet be seen for the bottommost one.
When looking at the time averaged Mach number contours, the smeared out wakes of the elliptic cylinders can be observed[19].

The contour plots of the instantaneous static pressure in the range of 0.7 to 1.5 bar show that the flow perturbations induced by the cylinder rotation drive the compressor into stall.
Whereas the bottommost blade passage still looks comparably normal, the passage shock is moving forward for the next two blade passages before it is again withdrawing. This pattern is then repeated for the fifth passage and in total moving forward.
The same can be observed for the time averaged pressure contours shown in the lower part of Figure 4.14. The time averaged plot doesn't feature the distinct shock known from the Oscillating VIGVs as shown in Figure 8.2, but shows it smeared out. This also implies that the shock is oscillating inside the blade passage.

Table 4.6: Time averaged forces on rotor blade 4

$F_{axial\ ave}$	-1.8 N/mm
$F_{tangential\ ave}$	1.0 N/mm
F_{ave}	2.1 N/mm

Accordingly, the blade force fluctuations as induced by the rotating 5 mm cylinders are with up to 30% blade mean load for the 600 Hz peak very high. This agrees well with the 600 Hz shock oscillation as observed when looking at the contour plots.
The second harmonic of the excitation frequency can be seen at 1200 Hz.
Moreover, the 15th engine order, the rotating cylinders more likely than the VIGVs, is also clearly visible at 4500 Hz.
The blade mean forces for the 5 mm diameter cylinders are given in Table 4.15 and agree comparably well with the blade mean forces for the Oscillating VIGVs. The deviation is about 5%.
For the 2.5 mm cylinders, the same pattern can be observed but with much smaller force fluctuations of about 10% blade mean load for the 600 Hz excitation.

[19]The pattern inside the rotating cylinder domain is again caused by the time averaging on a rotating mesh.

Summarizing, it can be concluded that the elliptic cylinders ECD05a2b1 are absolutely capable of exciting the rotor blades with 600 Hz, but do so by significantly influencing the flow field.
Moreover, the broad peak at 600 Hz implies that the excitation is not that clean, which was also outlined when looking at the phase controllability of the elliptic cylinders.
A cleaner excitation mechanism with a smaller impact on the mean flow is therefore desirable.

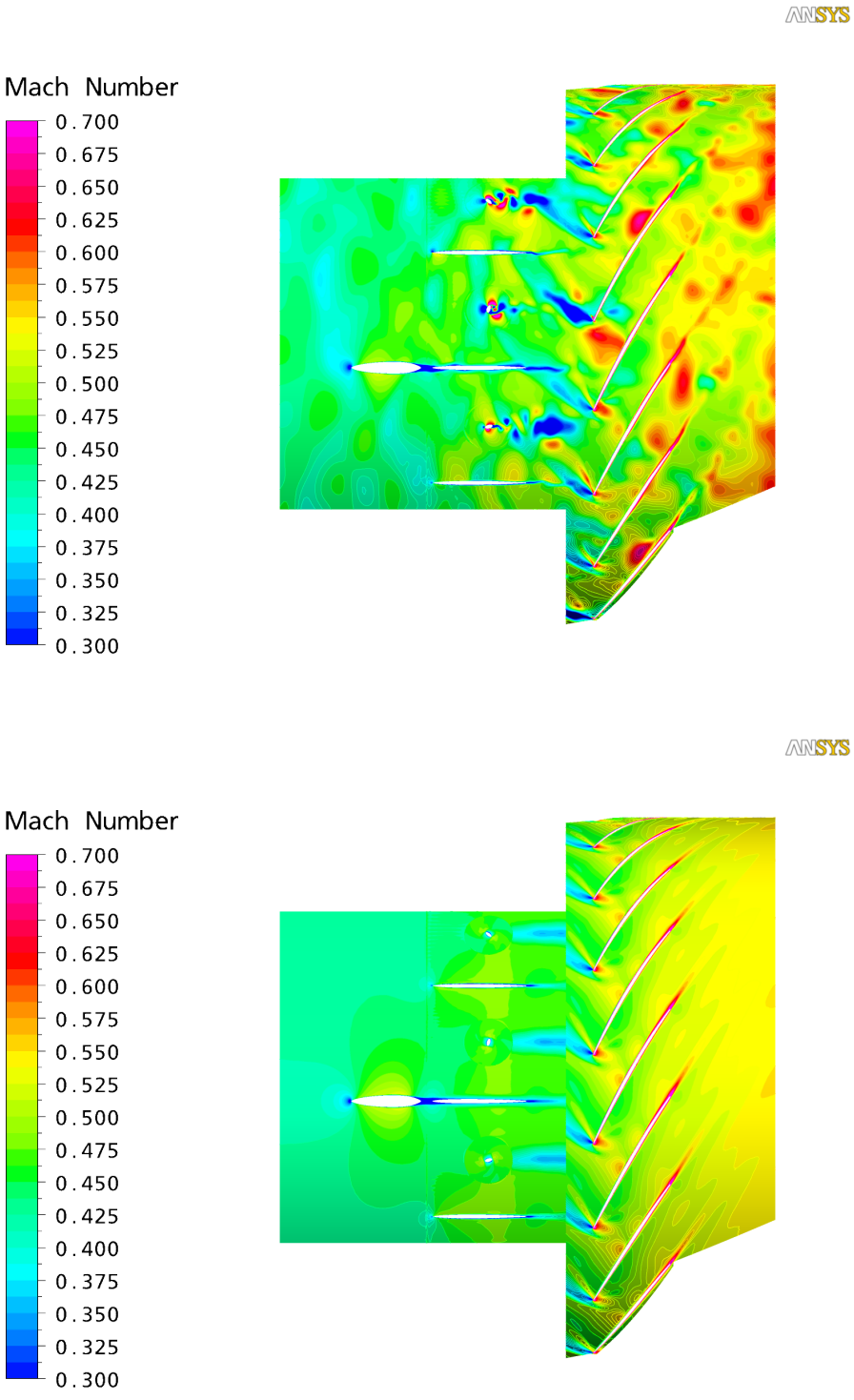

Figure 4.13: Instantaneous and time averaged M_{stn} for elliptic cylinders with 5 mm diameter

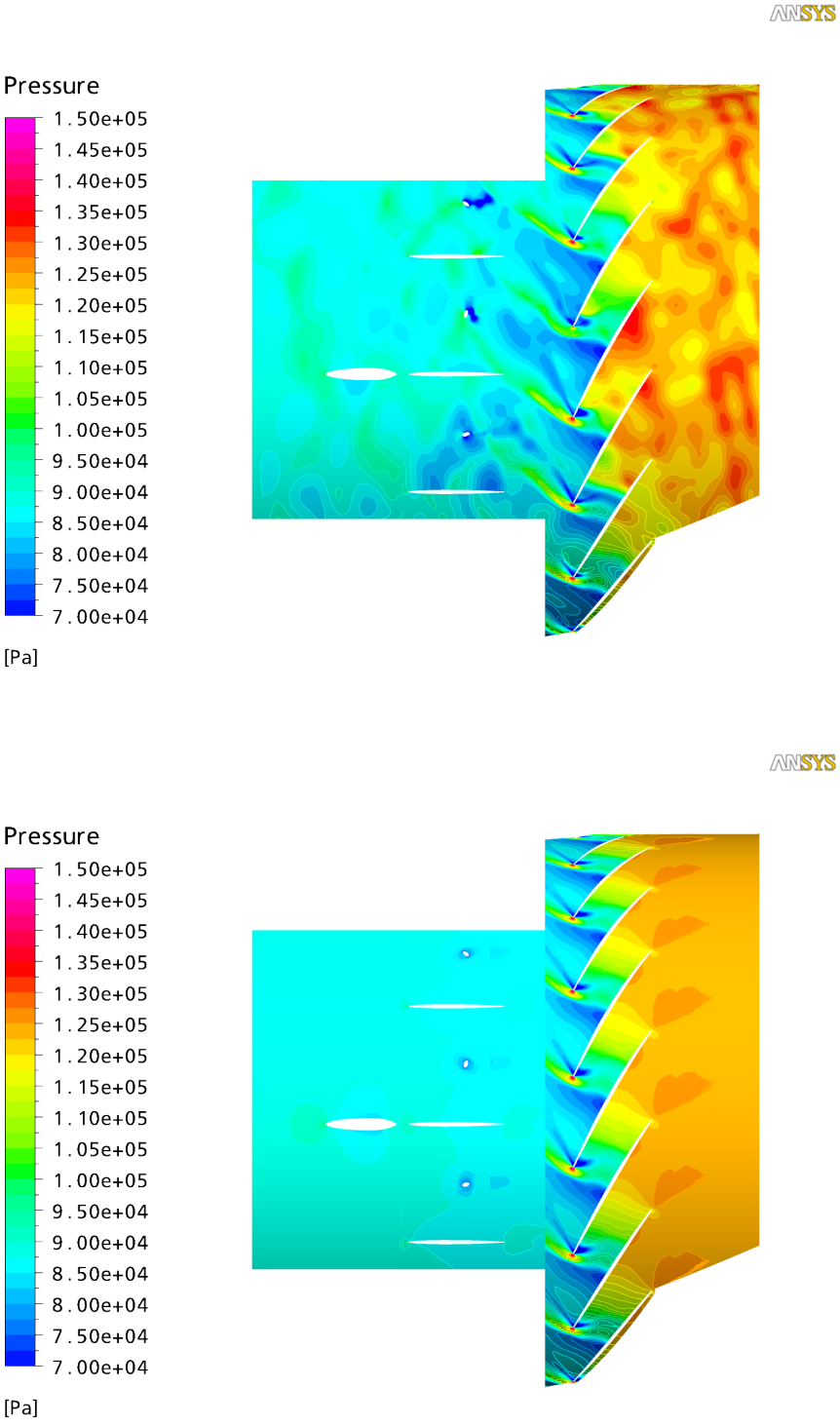

Figure 4.14: Instantaneous and time averaged p_s for elliptic cylinders with 5 mm diameter

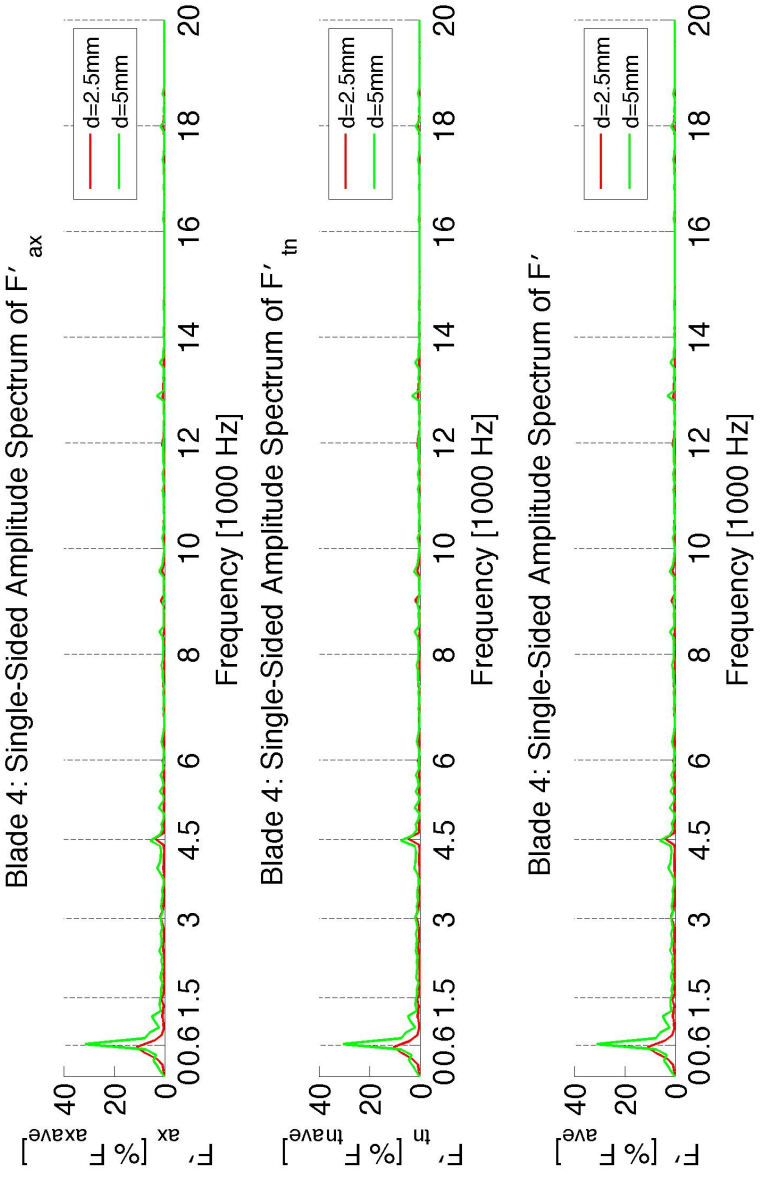

Figure 4.15: Rotating Elliptic Cylinders: Forces on rotor blade 4

5 Tangential Air Injection

Even though the Rotating Cylinders concept looks promising with regard to the achievable rotor blade amplitudes, two problems remain:

- Limited Phase Controllability
- Amplitude Control

For the Rotating Cylinders, the phase controllability will always be limited due to the turbulence the profile rotation involves.
Hence, the excitation of the rotor is a statistical process that cannot be controlled to a 100%.

The more critical issue, though, is to control the excitation level and thereby the rotor blade displacement.
With the Oscillating VIGVs, the excitation amplitude could be easily controlled by reducing the oscillation angle of the VIGVs and thereby lowering the induced tangential velocity component of the flow.
For the Rotating Cylinders, the excitation amplitude depends on the cylinder profile as well as the penetration depth, i.e. the cylinder length.
It is readily clear, that the profile cannot change during the forced response campaign. Thus, only changing the penetration depth remains. Unfortunately, this cannot be easily achieved and would require a complex and expensive mechanism to do so[1].

Therefore, air injection offering easily achievable amplitude control by regulating the supply pressure and thereby the injected mass flow comes into mind.
Tangential air injection generates flow disturbances comparable to the Rotating Cylinders by creating a velocity deficit and introducing turbulence during the compressed air pulse and does not disturb the main flow when the air pulse is past.

Figure 5.1 shows the concept based on additional injectors pulsing the compressed air tangentially towards the VIGVs.
In order to not induce an overall tangential velocity component, the compressed air is injected from both injector sides simultaneously.
The idea of the concept is to use injector profiles with a row of holes on each side through which the sharp air pulses are injected.

[1] Note, the cylinders are rotating with 800 rps and different phase angles!

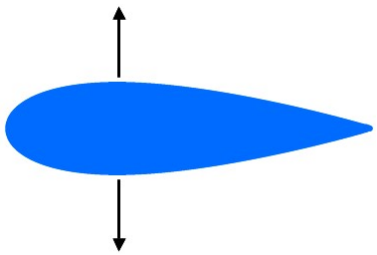

Figure 5.1: Concept for Tangential Air Injection

5.1 Injector Mass Flow

When looking at air injection, the first parameter that needs to be defined is the injected mass flow.
In agreement with the excitation system requirement that the impact on the mean flow be small and well determined, it was decided to limit the maximum allowable injected mass flow to 1% of the core mass flow.
Having a core mass flow of 14.2 kg/s for the R6S1 compressor configuration, this constrains the mean injected mass flow to 142 g/s.

The compressed air is supposed to be injected in distinct pulses using a high speed valve close to the injector nozzles[2].
The mass flow per injector can hence be described using the following function

$$\dot{m}(t) = \dot{m}_{max} \cdot \max\left(0,\, \sin\left(2\pi f \cdot t + \varphi\right)\right) \tag{5.1}$$

where $\dot{m}_{max}$ is the maximum mass flow per injector that yet remains to be defined. f is the excitation frequency in the stationary frame and φ the phase between the compressed air pulses of neighboring injectors depending on the traveling wave pattern that is to be excited. The function follows the positive half of the sine curve and remains zero for the negative half of the sine.
The average injector mass flow can hence be derived using

$$\dot{m}_{ave} = \frac{1}{T} \cdot \int_0^{\frac{T}{2}} \dot{m}_{max} \cdot \sin\left(2\pi f \cdot t + \varphi\right) dt \tag{5.2}$$

Neglecting φ, the average mass flow is $\dot{m}_{ave} = \frac{1}{\pi} \cdot \dot{m}_{max} \approx 0.32 \cdot \dot{m}_{max}$.

Having a supply pressure above the critical pressure ratio of 1.894 and hence assuming choked

[2] In order to keep the air pulses sharp, the feed cavity needs to be small and the valve therefore close to the nozzles.

flow in the injector nozzles, the mass flow per injector hole can be calculated as

$$\dot{m}_{hole} = \varrho u A = \varrho^* u^* A^* = \varrho^* a^* A^* \tag{5.3}$$

where ϱ is the density, u the flow velocity, a the speed of sound, A the hole area and * indicates choked conditions (see [17]).
Using

$$\varrho_t = \frac{p_t}{RT_t} \tag{5.4}$$

$$a_t = \sqrt{\gamma R T_t} \tag{5.5}$$

$$\frac{a^*}{a_t} = \left(\frac{2}{\gamma+1}\right)^{\frac{1}{2}} = 0.913 \tag{5.6}$$

$$\frac{p^*}{p_t} = \left(\frac{2}{\gamma+1}\right)^{\frac{\gamma}{\gamma-1}} = 0.528 \tag{5.7}$$

$$\frac{\varrho^*}{\varrho_t} = \left(\frac{2}{\gamma+1}\right)^{\frac{1}{\gamma-1}} = 0.634 \tag{5.8}$$

where R is the specific gas constant for air, γ the specific heat ratio for air and the index t indicates stagnation values, we can calculate the injected mass flow as a function of hole diameter and supply pressure (for constant supply temperature[3]).
A simplified numerical simulation was used to find hole diameter and supply pressure for a reasonable jet penetration width.
Promising values were found to be a 0.5 mm hole diameter with a supply pressure of 2 bar or 3 bar[4].
Table 5.1 summarizes the mass flow values for the Tangential Air Injection. As can be seen, all values are below the margin of 1% core mass flow.

[3] $T_t = 288.15$ K
[4] Larger pressures and areas lead to a significant blockage area when injecting the compressed air.

Table 5.1: Summary of mass flows for Tangential Air Injection

0.5 mm Hole Diameter, 3 bar Compressed Air Supply				
No. of Holes	$\dot{m}_{Injector}$ [g/s]	$\dot{m}_{Total}$ [g/s]	$\dot{m}_{Peak}$ [% $\dot{m}_{Core}$]	$\dot{m}_{Mean}$ [% $\dot{m}_{Core}$]
30	8.4	126.5	0.89	0.28
20	5.6	84.3	0.59	0.19
15	4.2	63.2	0.45	0.14
0.5 mm Hole Diameter, 2 bar Compressed Air Supply				
No. of Holes	$\dot{m}_{Injector}$ [g/s]	$\dot{m}_{Total}$ [g/s]	$\dot{m}_{Peak}$ [% $\dot{m}_{Core}$]	$\dot{m}_{Mean}$ [% $\dot{m}_{Core}$]
30	5.6	84.3	0.59	0.19
20	3.7	56.2	0.40	0.13
15	2.8	42.2	0.30	0.09

5.2 Setup

The approach for simulating the Tangential Air Injection is similar to the procedure used for the Oscillating VIGVs and the Rotating Cylinders studies.
Again, the CFX model represents $\frac{1}{5}$th of the compressor geometry at 92.5% tip radius including 1 front frame strut, 3 VIGVs, 4 rotor blades and now 3 additional injector profiles halfway between the VIGVs.
Hence, the setup used for the Rotating Cylinders concept was reused except for the inner domains with the elliptic profiles. The cylinders were replaced with NACA0025 airfoils as will be explained below.

In the preceding section it was mentioned that a promising design for the Tangential Air Injection was found to have an injector hole diameter of 0.5 mm and a supply pressure of 2 to 3 bar, with the values as specified in Table 5.1.
The thickness of the geometry used for the numerical simulation is with 0.05 mm only one tenth of the hole diameter. Thus, the Tangential Air Injection was modeled as a slot with 0.5 mm width and 0.05 mm height.
The mass flow for the simulation was calculated based on the area ratio of $\frac{A_{hole}}{A_{CFX}} = 7.9$.
For this concept it is obviously more problematic than for the preceding studies that 3D decay effects are neglected. Instead of modeling a segment of a VIGV extending over the entire span or at least a 20 mm long cylinder, the segment of a small injector nozzle is modeled.
Therefore, 3D vortex decay would probably have a larger effect on the quality of the results of this simulation.

5.2.1 Injector Profile

For being able to simulate the Tangential Air Injection, a representative injector profile needs to be found.
Two issues have to be considered when trying to find an appropriate injector:

- the profile needs to be thick enough to incorporate the compressed air feed line

- the profile has to be short enough to fit into the CFX setup

As for the elliptic cylinders, the inner domains into which the profiles need to be integrated have a diameter of 30 mm. In order to keep the solid walls of the profile at least 5 mm away from the interface, the maximum profile length cannot exceed 20 mm.
For representing a profile capable of incorporating the compressed air supply, the profile thickness should not be less than 5 mm.
Hence, the symmetric NACA0025 airfoil out of the NACA 4-digit series with a maximum thickness t of 25% at 30% chord was used.
The profile was generated with MATLAB using

$$y = c\frac{t}{0.20}\left(0.2969\sqrt{\frac{x}{c}} - 0.1260\left(\frac{x}{c}\right) - 0.3537\left(\frac{x}{c}\right)^2 + 0.2843\left(\frac{x}{c}\right)^3 - 0.1015\left(\frac{x}{c}\right)^4\right) \quad (5.9)$$

where c is the chord length, x the position along the chord, y half the thickness at position x and t the maximum thickness as a fraction of the chord.

For the Tangential Air Injection, the injector nozzles are positioned at 30% chord, where the airfoil has its maximum thickness[5].
This also guarantees that the flow is injected in normal direction without gaining axial momentum due to the leaned airfoil surface normal.

5.2.2 Mesh and Solver Setup

As mentioned before, the mesh is in general identical to the Rotating Cylinders mesh, only that the inner domains with the elliptic cylinders have been replaced by the NACA0025 injectors.
Figure 5.2 shows the mesh as it was used for obtaining the rotor response effected by Tangential Air Injection. Concerning the mesh statistics, be here only refered to the values as given in Table 4.4. The values are consistent, only that the minimum angle for the front frame domain is reduced to 21° because of the NACA0025 airfoil.

The CFX simulation used for the Tangential Air Injection is similar to the simulation used for the Elliptic Cylinders with two exceptions:

- Domains around the NACA0025 airfoils are stationary
- Injector nozzles are specified as inlets

Since the injectors are not rotating, the application of a mesh motion is not required. The interface connecting the inner injector domain and the surrounding front frame domain can be specified as GGI[6], thereby saving computing time.

[5] Having the NACA0025 profile equidistantly integrated into the Rotating Cylinder Interface of the compressor domain, the nozzle is not placed in the center of the interface but 4mm upstream resulting in a distance to the rotor leading edge of 296.41 mm.
[6] GGI = General Grid Interface

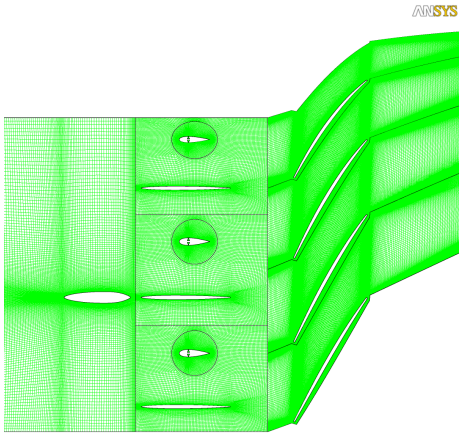

Figure 5.2: Hexahedral mesh as used for Tangential Air Injection

In order to overcome convergence problems with the compressed air injection, the inlets of the injection holes had to be defined as subsonic inlets.
For still being able to achieve choked flow inside the injection holes, converging nozzles had to be created and attached to these holes.
First, the area ratio for the nozzle has to be found for obtaining choked flow. Using

$$\frac{A}{A^*} = \sqrt{\frac{1}{M^2}\left(\frac{2}{\gamma+1}\left(1+\frac{\gamma-1}{2}M^2\right)\right)^{\frac{\gamma+1}{\gamma-1}}} \tag{5.10}$$

we obtain an area ratio of 3 for still choking a hole inlet Mach number of 0.2.
Knowing the injector hole to have a width of 0.5 mm, the nozzle inlet needs to be 1.5 mm wide.
For a simple cosine shaped nozzle, the nozzle profile can be created in MATLAB applying

$$y(x) = 0.25\,mm + \left(1 - \cos\left(\frac{\pi}{L}\cdot x\right)\right)\cdot 0.5\,mm \tag{5.11}$$

where L is the nozzle length, x the position along the nozzle axis and y half the nozzle width. Here, L was arbitrarily set to 1.5 mm.
Having meshed the nozzle geometry with ANSYS ICEM CFD and imported it as separate domain to the Tangential Air Injection simulation, the nozzle can be attached to the injector nozzles using a GGI connection.
Figure 5.3 shows a close up of the injector profile with the two nozzles located at 30% chord.

Having thus created the mesh and set up the solver for analyzing the Tangential Air Injection

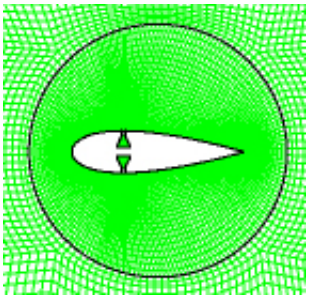

Figure 5.3: Nozzles for Tangential Air Injection

concept, the time resolution for the transient simulation still needs to be defined.
Due to time limitations, the time step was increased to $\frac{1}{315000}$s, resulting in about 52 time steps per blade passage.
For recording the blade forces, the monitoring function was used again writing out the blade forces for each time step.
The total time of the simulation was set to $\frac{1}{200}$s equivalent to 1.5 rotor revolutions or 30 blade passings.

5.2.3 Specifying the Excitation

As for the Oscillating VIGVs and the Rotating Cylinders, aim for the Tangential Air Injection is to excite the 1F mode of R6 with 3 nodal diameters forward traveling wave.
Due to the limitations of the numerical setup featuring only $\frac{1}{5}$th of the compressor annulus, the 5 nodal diameters forward traveling wave will instead be excited.
This results in a phase difference of 120° between the air pulses of neighboring injectors.
When exciting 5 nodal diameters, the excitation frequency needs to be adapted. In order to excite the rotor blades with a frequency of 600 Hz, the excitation frequency in the stationary frame needs to be 2100 Hz as explained before.
In Figure 5.4, the inception of the Tangential Air Injection is shown with the uppermost injector (see 5.2) starting first and the bottommost injector starting last.

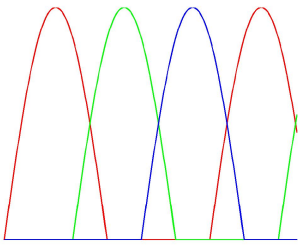

Figure 5.4: Onset of air pulsation with 5 nodal diameters forward traveling wave

Subsequently, we can summarize the excitation based upon Tangential Air Injection as follows:

- Traveling wave pattern: 5 nodal diameters forward traveling wave with $\varphi = 120°$
- Excitation frequency in stationary frame: 2100 Hz
- Excitation frequency in rotor frame of reference: 600 Hz
- Excitation amplitude: 2 and 3 bar air injection with 0.5 mm hole diameter

5.3 Results

In the following, the results for the Tangential Air Injection with a supply pressure of 2 bar and a hole diameter of 0.5 mm are given.
Figure 5.5 shows a contour plot of the Mach number in the stationary frame in the range of 0.3 to 0.7.
The upper image shows the instantaneous results, the lower image shows the time averaged flow field.
The corresponding static pressure contours are given in Figure 5.6 with a range of 0.7 to 1.5 bar.

When we look at the instantaneous plot of the Mach number, we can first of all observe that the flow field inside the compressor passages is heavily affected by the tangential air pulses. No blade passages resembles its adjacent passages.
Moreover, we can readily recognize the traveling wave pattern. When looking at the regions of low Mach number in between NACA0025 profiles and rotor leading edge, we can see that in line with the lowest injector one of those low Mach number regions is interfering with the rotor leading edge. Looking two blades upwards, we see that the interference pattern has already reached the blade passage whereas it has already disappeared for the uppermost injector.
A second diagonal of blue spots representing the blockage regions created by the air injection has already started to propagate towards the rotor.
The same pattern can be observed when looking at the air pulses themselves marked by the pink spots representing high Mach number regions.

Looking at the time averaged Mach number as given in the lower contour plot, we see the dominating wake of the injectors caused by the Tangential Air Injection.
We also perceive regions of high Mach number in between the injectors and the VIGVs, where the flow is accelerating because of the blockage zones. In a 3D simulation, this effect would probably not be as dominant.

In Figure 5.6 it is clearly shown how severely the compressor is driven into stall by the Tangential Air Injection. Whereas the third blade passage from the bottom shows still a comparably normal flow pattern, the passage shock is beginning to move upstream in the fourth blade passage from the bottom. This also agrees with the Mach number plot since this

is the very blade where the low Mach number bubble hits the rotor leading edge.
In blade passages five and six, the shock has already left the passage and is beginning to separate from the leading edge.
Blade passages seven, is again in phase with blade passage three.

The same is confirmed by the time averaged static pressure plot in the lower image. That the shock is smeared out along the blade chord indicates that it is oscillating inside the passage.

Having perceived that the compressor is actually driven into stall, it is not surprising to find the blade forces fluctuate by about 30 to 40% blade mean load as shown in Figure 5.7 for the 600 Hz excitation frequency[7].
The second and third largest peaks are found for frequencies of 1200 Hz and 4500 Hz. 1200 Hz corresponds to the second harmonic of the blade excitation frequency, the 4500 Hz is the 15th engine order, i.e. either the VIGVs or - more likely - the injectors.
When comparing the rotor blade forces for 2 and 3 bar air injection, it is remarkable that the forces don't change significantly.
Having seen how the Tangential Air Injection affects the flow field, this can be readily explained.
Instead of exciting the rotor blades directly, the Tangential Air Injection messes up the flow field what then causes the rotor excitation.

Table 5.2 summarizes the time averaged blade forces for the Tangential Air Injection simulation. The values differ up to 15% from the values without excitation what is probably caused by the significantly affected flow field.

Table 5.2: Time averaged forces on rotor blade 4

$F_{axial\,ave}$	-1.73 N/mm
$F_{tangential\,ave}$	0.93 N/mm
F_{ave}	1.96 N/mm

Even though the observed effects might be less crucial in a 3D flow, it still remains questionable whether it is desirable to excite a rotor with a particular high flutter susceptibility in such a way.
In order to bring down the amplitudes and improve the controllability, the flow perturbations need to be significantly reduced, either by lowering the supply pressure or by decreasing the injector hole diameter.

[7] As for the blade forces in the preceding chapters, the blade force data was analyzed using the standard MATLAB FFT function.

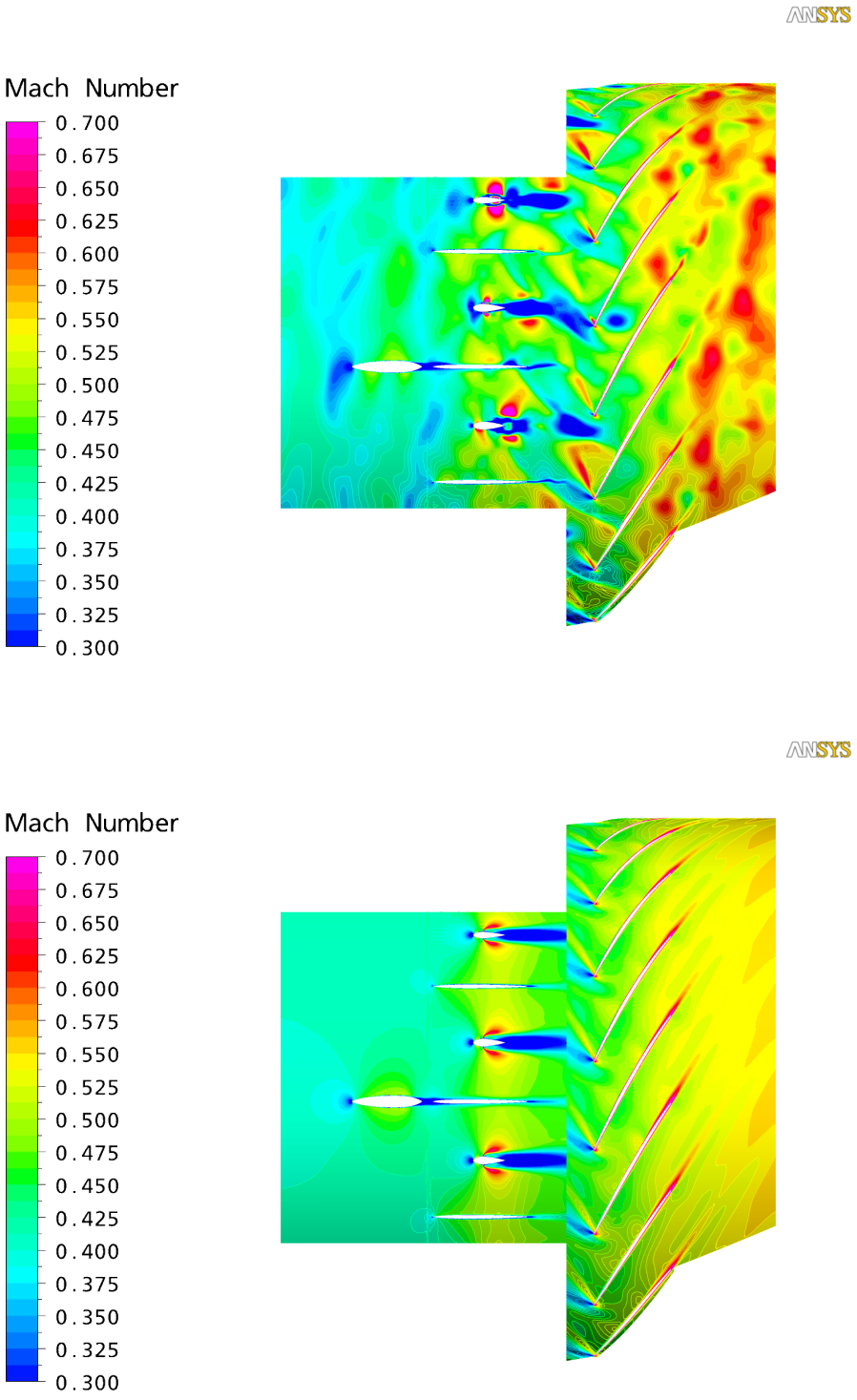

Figure 5.5: Instantaneous and time averaged M_{stn} for Tangential Air Injection with 2 bar compressed air supply

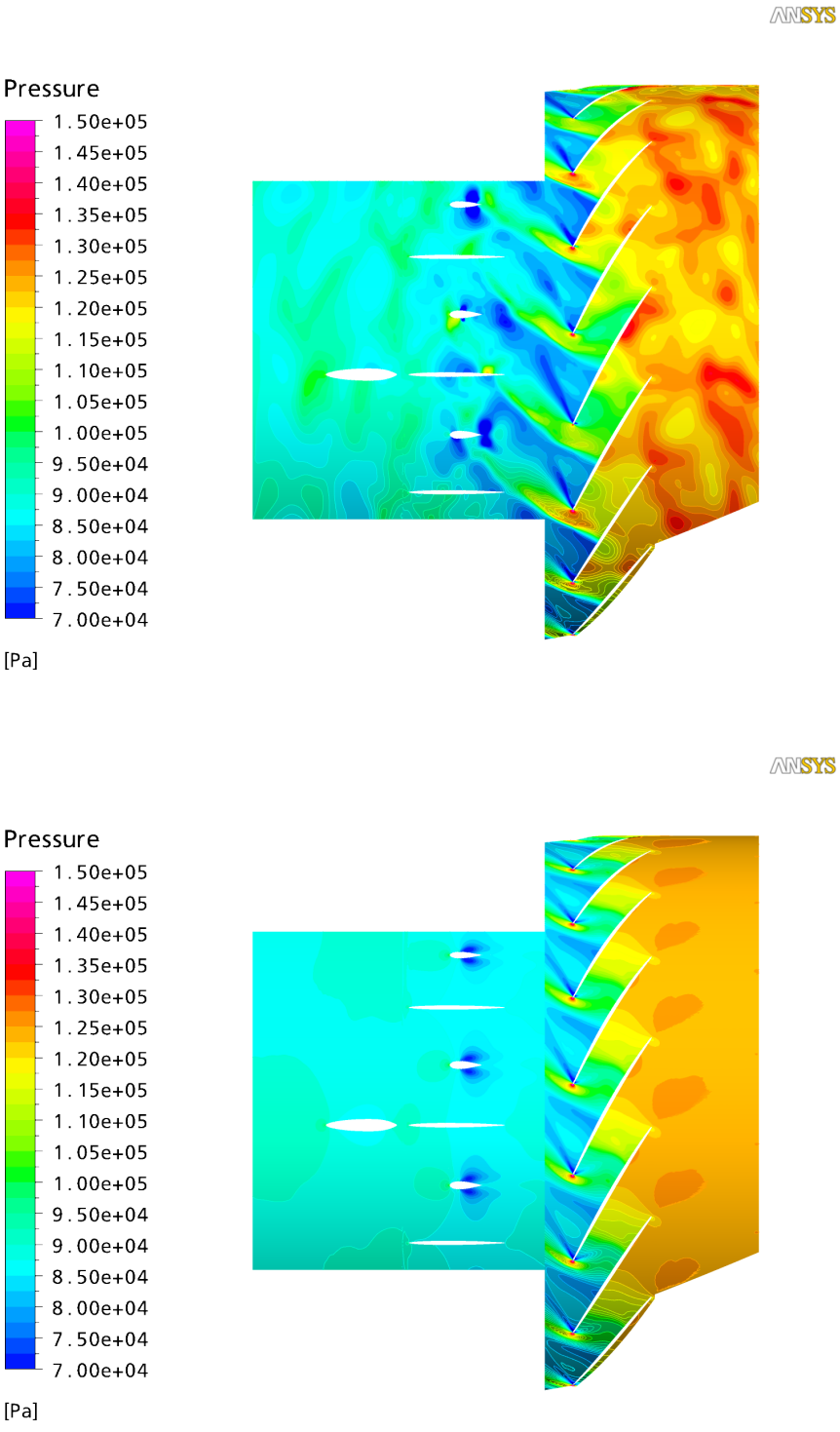

Figure 5.6: Instantaneous and time averaged p_s for Tangential Air Injection with 2 bar compressed air supply

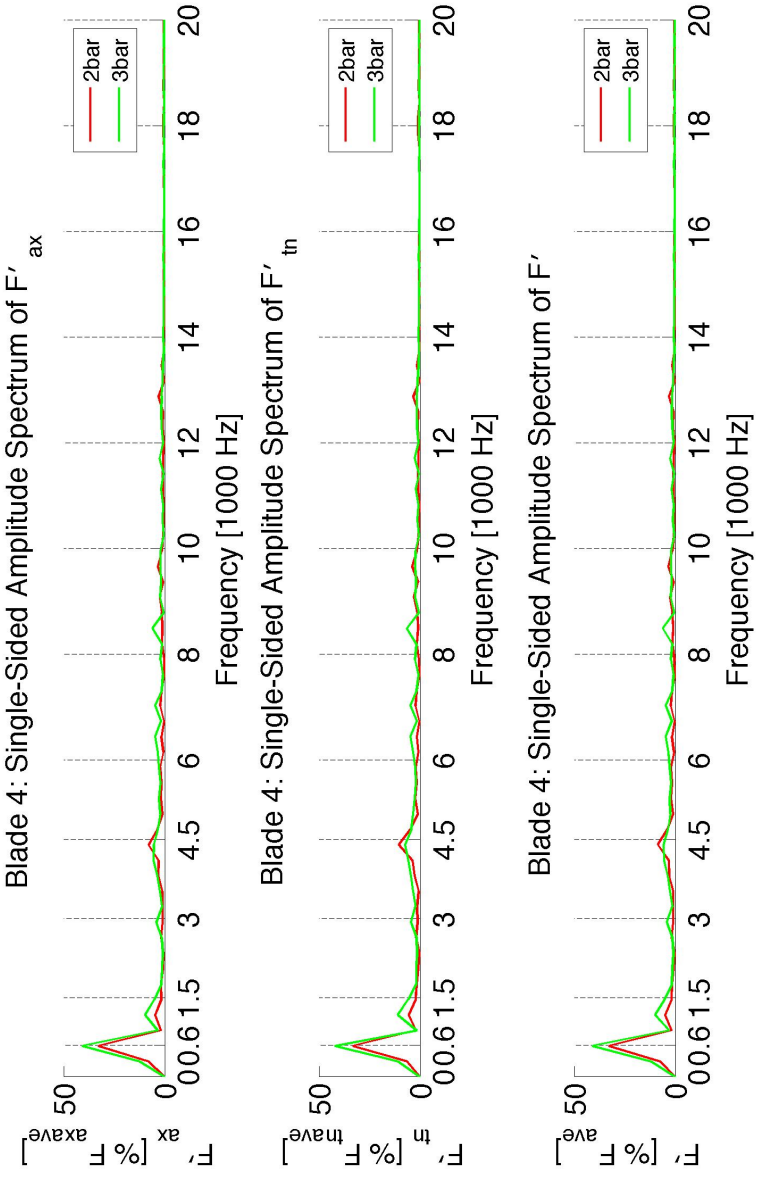

Figure 5.7: Tangential Air Injection: Forces on rotor blade 4

6 Axial Air Injection

Having observed that introducing too much turbulence drives the compressor quickly into stall, it seems reasonable to consider a somewhat cleaner excitation system concept.
Having obtained substantial excitation amplitudes with a reasonably small injector mass flow for the Tangential Air Injection it can be assumed that a concept with Axial Air Injection offering a more direct excitation is also feasible.

Therefore, the same injector profiles have been adapted as to inject the flow from their trailing edge in axial direction towards the rotor.
The concept is outlined in Figure 6.1

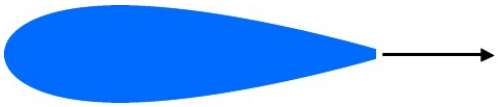

Figure 6.1: Concept for Axial Air Injection

Table 6.1 summarizes the mass flow data for Axial Air Injection. Having only one row of injector holes at the trailing edge instead of two at the profile sides as for Tangential Air Injection, only half the mass flow is injected for identical supply pressures.

Table 6.1: Summary of mass flows for Axial Air Injection

0.5 mm Hole Diameter, 4 bar Compressed Air Supply				
No. of Holes	$\dot{m}_{Injector}$ [g/s]	$\dot{m}_{Total}$ [g/s]	$\dot{m}_{Peak}$ [% $\dot{m}_{Core}$]	$\dot{m}_{Mean}$ [% $\dot{m}_{Core}$]
30	5.6	84.3	0.59	0.19
20	3.7	56.2	0.40	0.13
15	2.8	42.2	0.30	0.09
0.5 mm Hole Diameter, 3 bar Compressed Air Supply				
No. of Holes	$\dot{m}_{Injector}$ [g/s]	$\dot{m}_{Total}$ [g/s]	$\dot{m}_{Peak}$ [% $\dot{m}_{Core}$]	$\dot{m}_{Mean}$ [% $\dot{m}_{Core}$]
30	4.2	63.2	0.45	0.14
20	2.8	42.2	0.30	0.09
15	2.1	31.6	0.22	0.07
0.5 mm Hole Diameter, 2 bar Compressed Air Supply				
No. of Holes	$\dot{m}_{Injector}$ [g/s]	$\dot{m}_{Total}$ [g/s]	$\dot{m}_{Peak}$ [% $\dot{m}_{Core}$]	$\dot{m}_{Mean}$ [% $\dot{m}_{Core}$]
30	2.8	42.2	0.30	0.09
20	1.9	28.1	0.20	0.06
15	1.4	21.1	0.15	0.05

6.1 Mesh Setup

The mesh for the Axial Air Injection study is identical to the mesh used for Tangential Air Injection, with the exception that the trailing edge of the NACA0025 airfoil has been truncated by 0.85 mm to fit in the injector holes.
The converging, cosine shaped nozzle known from the previous chapter was moved to the injector trailing edge.

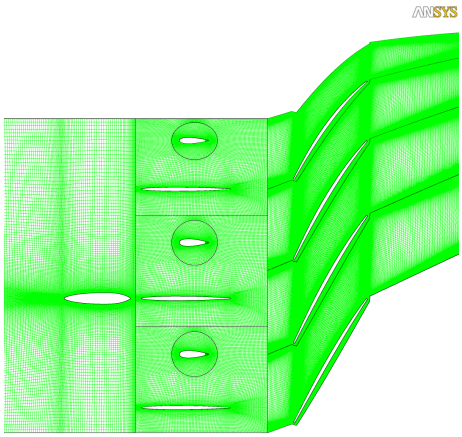

Figure 6.2: Hexahedral mesh as used for Axial Air Injection

Figures 6.2 and 6.3 show the overall mesh and a close-up of the injector profile with the nozzle connected to the trailing edge[1].

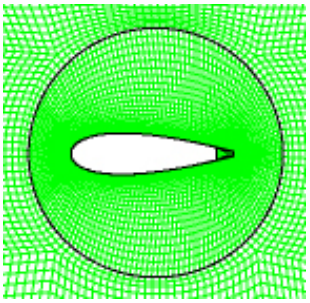

Figure 6.3: Nozzle for Axial Air Injection

[1] That nozzle and profile overlap is unimportant since they are defined as different domains. The connection is again a GGI.

6.2 Solver Setup

The setup of the solver is entirely identical to the Tangential Air Injection case.
The simulation was also resolved with a time step of $\frac{1}{315000}$s and thereby about 52 time steps per blade passage.
As for the Tangential Air Injection, the total simulation time was set to $\frac{1}{200}$s resolving 1.5 rotor revolutions and thus 30 blade passings.

The excitation was defined as to excite a 5 nodal diameter forward traveling wave with a phase difference of 120° between the pulsation of neighboring axial injectors as shown in Figure 5.4.
The excitation frequency in the stationary frame was adapted for the 5 nodal diameters and therefore set to 2100 Hz.
The excitation amplitudes were defined by 2, 3 and 4 bar air supply.

Summing up, the excitation parameters are:

- Traveling wave pattern: 5 nodal diameters forward traveling wave with $\varphi = 120°$
- Excitation frequency in stationary frame: 2100 Hz
- Excitation frequency in rotor frame of reference: 600 Hz
- Excitation amplitude: 2, 3 and 4 bar air injection with 0.5 mm hole diameter

6.3 Results

The following contour plots show the results for the Axial Air Injection with a compressed air supply of 4 bar.
In Figure 6.4 the Mach number in the stationary frame is plotted in the range of 0.3 to 0.7.
Figure 6.5 gives the corresponding contour plot of the static pressure within the range of 0.7 to 1.5 bar.

What immediately strikes the eye is the cleanliness of the flow field. Other than Rotating Cylinders and Tangential Air Injection, Axial Air Injection does not change the flow field significantly.
Looking at the instantaneous results for the Mach number contour, one can observe the five nodal diameter pattern distinctly.
Focusing on the central injector, we perceive the air pulse just emerging from the injector nozzle.
Looking at the uppermost injector, the pulse has just been shut of and the jet is propagating towards the rotor.
When finally looking either another injector passage upwards or at the bottommost injector, we see that the new air pulse cycle has not yet started. Instead, the jet from the last cycle just enters the blade passage and interacts with the leading edge shock.

The time averaged Mach number contours show a high Mach number region around the injectors.
While wakes, i.e. regions with velocity deficits can be seen for the strut and the VIGVs, the inverse is the case for the injectors. Here, the time averaged Mach contour shows a negative velocity deficit, that is, the velocity relative to the main flow is positive.

The pressure contours do not show much but that the shock pattern inside the blade passage remains rather unimpressed by the Axial Air Injection.

When thus looking at Figure 6.6, a moderate rotor blade excitation of about 7% blade mean load can be seen for 600 Hz, the excitation frequency in the rotor frame of reference.
Remarkable is, how well the amplitude can be controlled. In accordance to the thrust equation does an increase in pressure lead to an increase in blade forcing at the excitation frequency.
Besides the prominent peak at 600 Hz, another pronounced peak at 9000Hz, the 30th engine order, can be seen. This peak is caused by VIGVs and axial injectors.
Moreover, minor peaks at 1200 Hz, the second harmonic of the excitation frequency in the rotor frame and at 4500 Hz, i.e. the VIGVs or the axial injectors can be observed.
Even though the fifth engine order caused by the struts cannot be perceived at 1500 Hz, the second harmonic thereof at 3000 Hz can be detected.
Table 6.2 summarizes the mean values for axial, tangential and total blade force. The blade forces agree very well with the forces for the case without excitation and do thereby also confirm the cleanliness of the Axial Air Injection.

Table 6.2: Time averaged forces on rotor blade 3

$F_{axial\,ave}$	-1.76 N/mm
$F_{tangential\,ave}$	1.05 N/mm
F_{ave}	2.05 N/mm

Even though the rotor blade excitation is with only 7% blade mean force significantly smaller than that of Rotating Cylinders or Tangential Air Injection, the cleanliness and the amplitude controllability of the Axial Air Injection make it a promising concept.

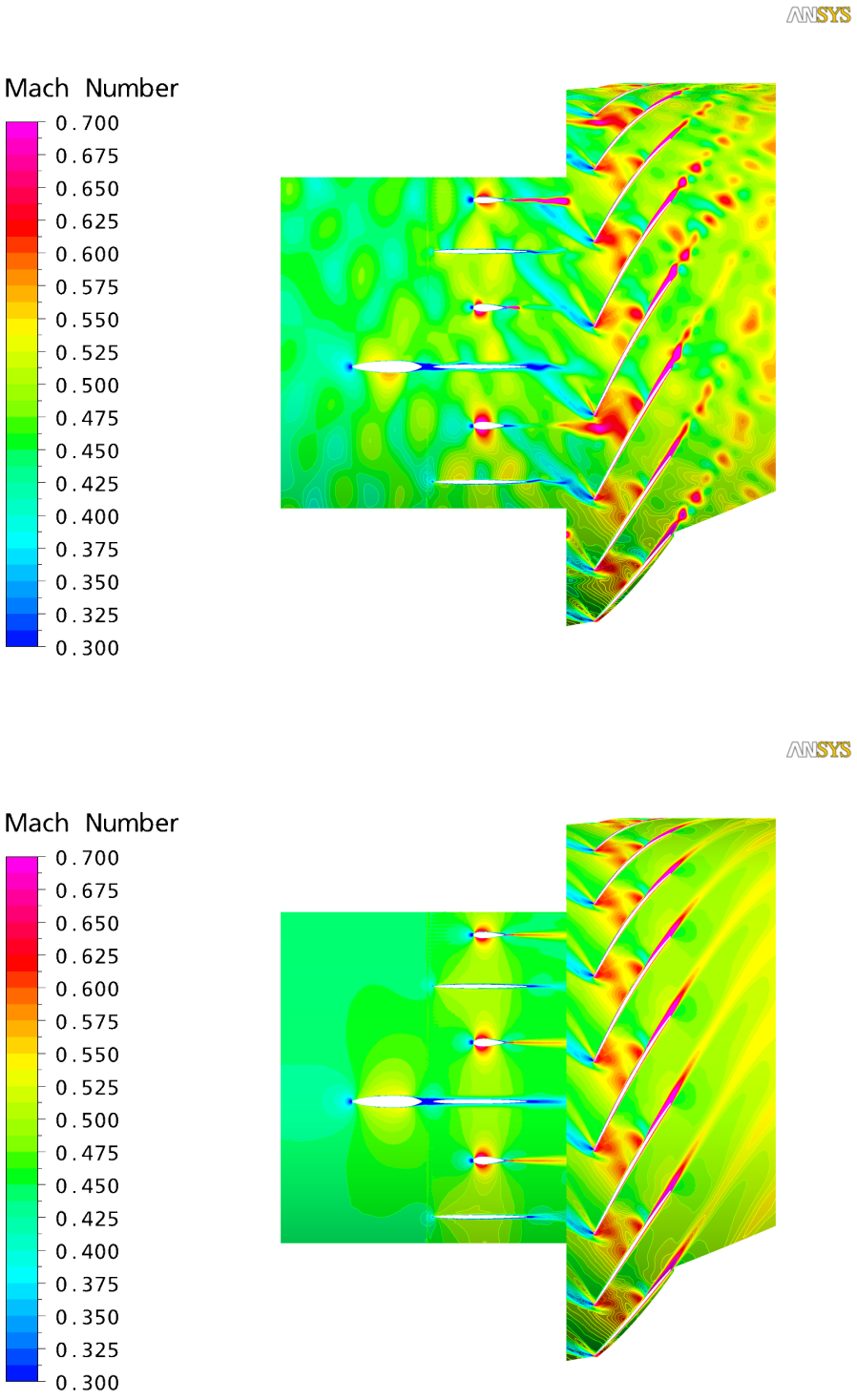

Figure 6.4: Instantaneous and time averaged M_{stn} for Axial Air Injection with 4 bar compressed air supply

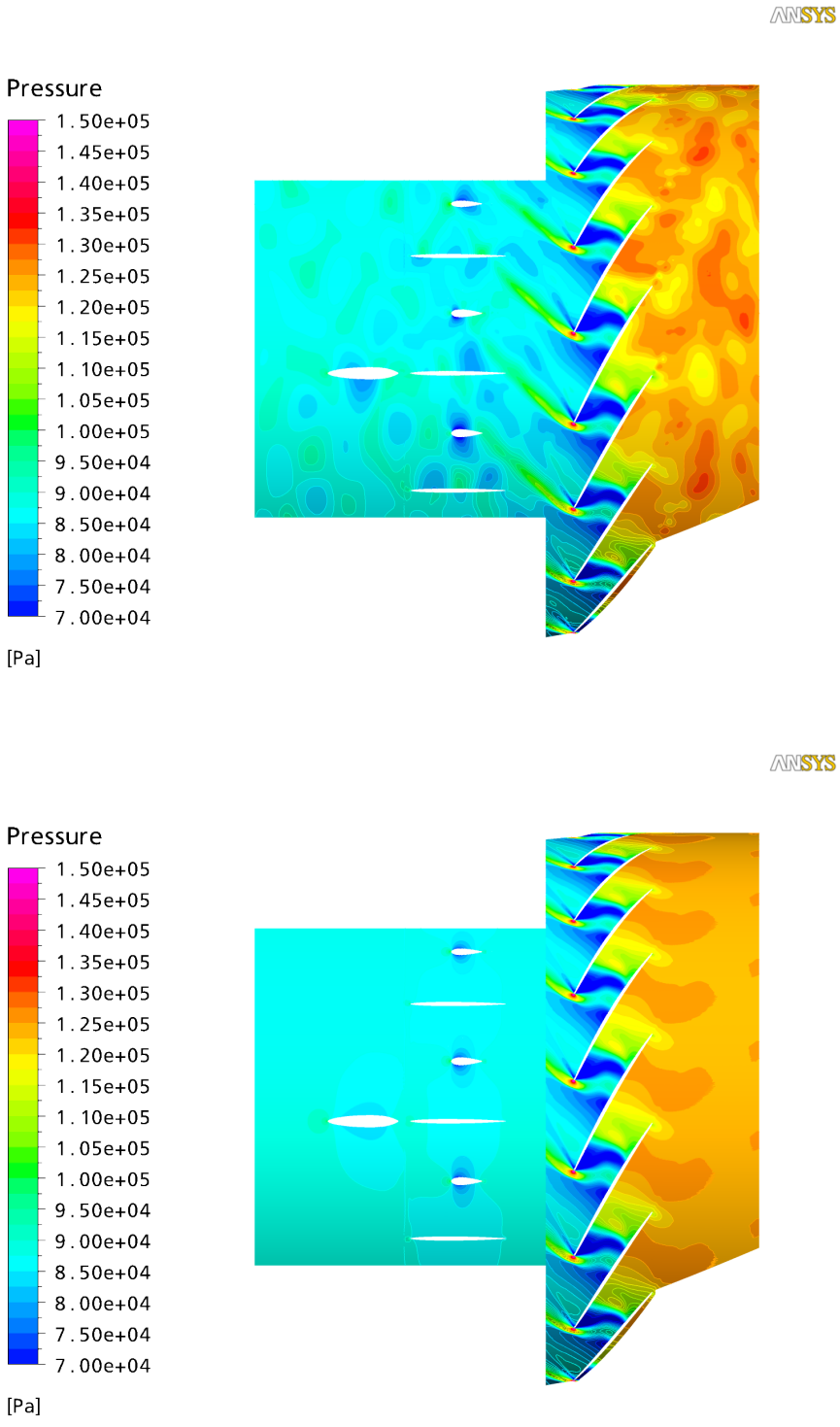

Figure 6.5: Instantaneous and time averaged p_s for Axial Air Injection with 4 bar compressed air supply

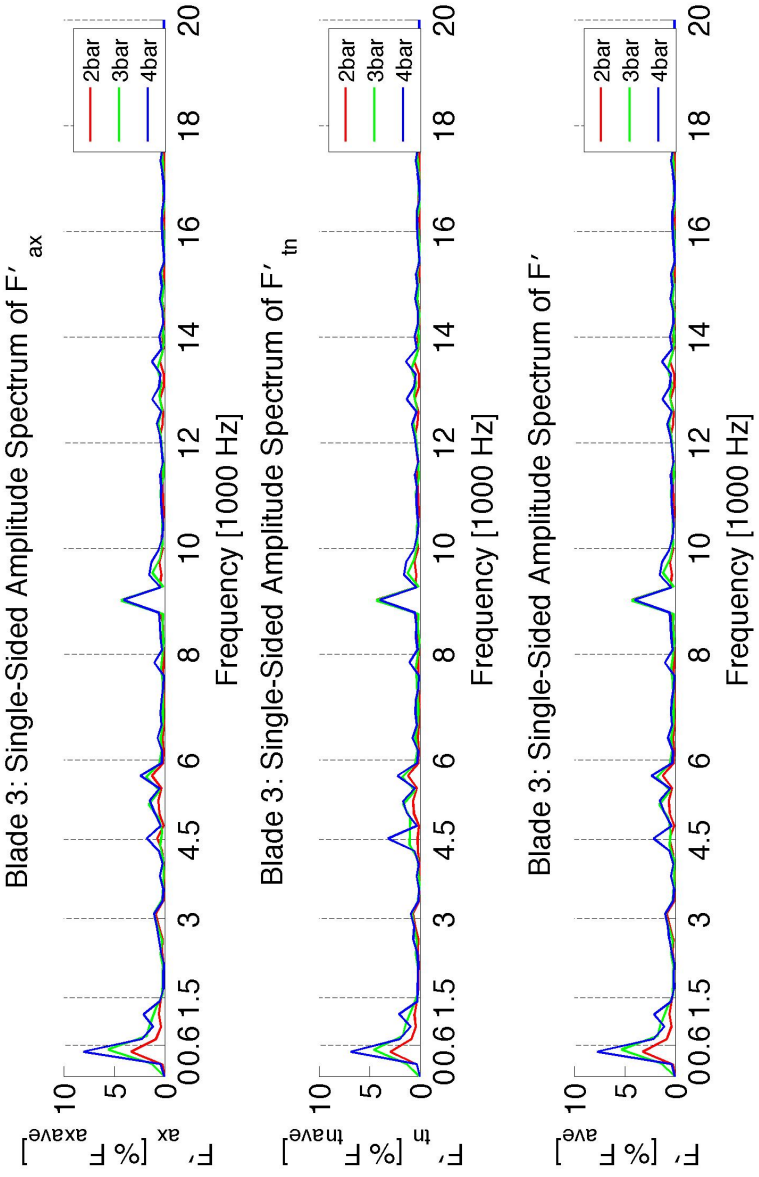

Figure 6.6: Axial Air Injection: Forces on rotor blade 3

7 Summary and Conclusions

From what was discussed in the previous chapters, all investigated excitation system concepts seem capable of exciting the rotor blades to the required degree.
The excitation levels for the different concepts vary significantly, but none of the excitation system concepts has levels so small that they deem it impractical.
The smallest excitation level of about 5% blade mean force is obtained for the Oscillating VIGVs, but again, the VIGV oscillation acts across the entire span and therefore still leads to sufficient forcing.

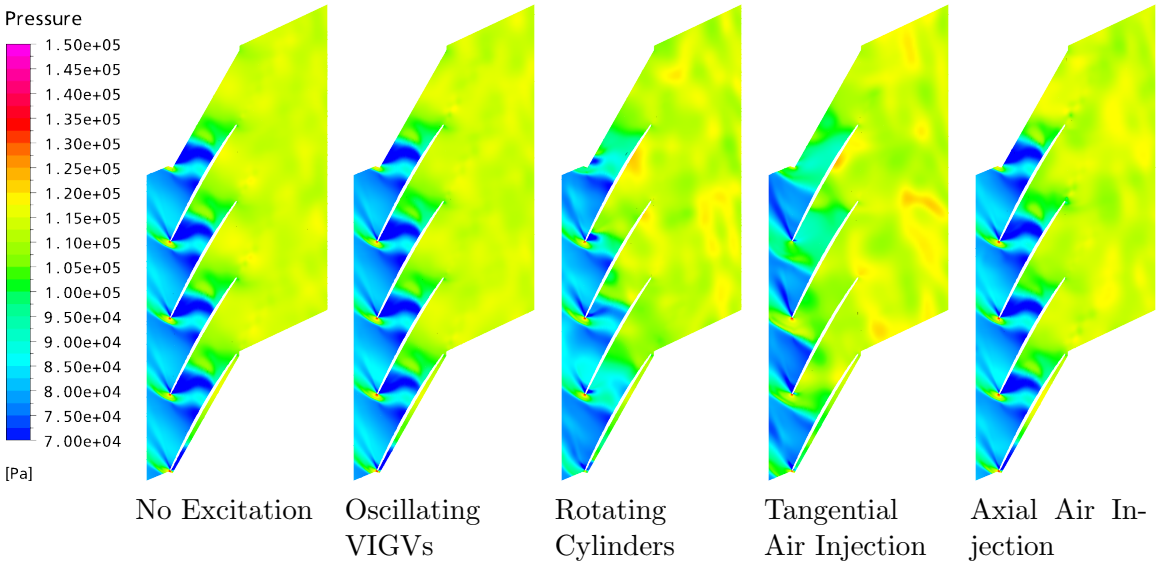

Figure 7.1: Comparison of static pressure contour plots

The superior concept proposes itself when considering the static pressure contour plots as shown in Figure 7.1:
Knowing - what was just stated - that all of the concepts generate satisfactory rotor blade forces and thus looking at the flow patterns in the rotor blade passages, we can readily see that just two of the proposed concepts result in a clean rotor flow field.
Only for the Oscillating VIGVs and the Axial Air Injection remains the flow pattern almost identical to the flow in the blade passages for the case without excitation.
For the Rotating Cylinders as well as for the Tangential Air Injection, the compressor is driven into stall.

Having to discard the Oscillating VIGVs for mechanical reasons, solely the Axial Air Injection remains and is hence the excitation system concept recommended.

Using a more complete approach to evaluate the excitation system concepts leads to the same conclusion.
Table 7.1 contains the evaluation matrix as proposed for selecting a concept.

Table 7.1: Concept evaluation matrix

	Oscillating VIGVs	Rotating Cylinders ECD05a2b1	Tangential Air Injection	Axial Air Injection
Frequency	✓	✓	✓	✓
Integrability and Cleanliness	✓	✓	✓	✓
Mechanical Robustness	*X*	✓	✓	✓
(Phase) Controllability	1	1	3	6
Excitation Level	3	6	6	3
Low Impact on Mean Conditions	6	1	1	6
Sum	**10**	**8**	**10**	**15**

The Frequency criterion is evaluated on a pass-fail basis since it would certainly limit the feasibility of the concept.

Integrability and Cleanliness as well as Mechanical Robustness are also assessed as pass or fail criteria as they were not explicitly investigated in this study. For the Oscillating VIGVs concept the mechanical limitations are known, hence Oscillating VIGVs are given a failing grade. All other concepts seem promising when it comes to these aspects.

Oscillating VIGVs as well as Rotating Cylinders are given only 1 point for (Phase) Controllability since the exciting perturbations are not directly controlled, but introduced indirectly by a component motion.
Tangential Air Injection is given 3 points for (Phase) Controllability for the reason that the flow perturbations are created with sharp air pulses controlled by a high speed valve. The

small motion of the valve is believed to be better controllable than the motion of the larger VIGVs or Rotating Cylinders.
Axial Air Injection is considered superior to the other concepts when it comes to controllability since the air pulse is aiming directly for the rotor. Hence, the excitation is most directly applied.

The excitation level for Rotating Cylinders as well as for Tangential Air Injection is by orders of magnitude greater than the excitation levels for Oscillating VIGVs and Axial Air Injection. Nevertheless, non of the concepts is incapable of exciting the rotor to a satisfactory degree.

As lined out above, the impact on the mean flow is significant for Rotating Cylinders and Tangential Air Injection. Both concepts achieve the large excitation levels by driving the compressor into stall[1].

Concluding, Axial Air Injection seems the most promising concept and should be aimed for.
Since in the present study 3D decay effects have been neglected, performing a 3D simulation for finding the optimum parameters of this concept is strongly recommended.

Based upon the presented results, an initial design for beginning a more detailed study on Axial Air Injection could look like the one given in Figure 7.2.

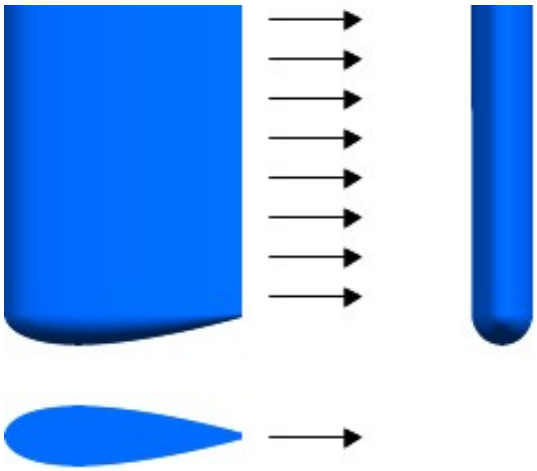

Figure 7.2: Potential design for an axial air injector

Table 7.2[2] summarizes the main parameters for the Axial Air Injector as shown in Figure 7.2.

[1] Redimensioning the cylinders and the injector nozzle size might help to overcome this problem, but then with the drawback of also reducing the achievable excitation level.
[2] Injector height refers to the length of the injector sticking into the compressor and utilized for distributing the injector holes at the trailing edge.

Table 7.2: Potential parameters for an axial air injector

Parameter	**Value**
Profile Geometry	NACA0025
Profile Chord Length	20 mm
Injector Height	20 mm
Supply Pressure p_0	4 bar
Hole Diameter d_h	0.5 mm
Number of Holes n_h	20
Peak Mass Flow/Injector $\dot{m}_{peak\,i}$	3.75 g/s
Mean Mass Flow/Injector $\dot{m}_{mean\,i}$	1.2 g/s
Total Peak Mass Flow $\dot{m}_{peak\,t}$	56.3 g/s
Total Mean Mass Flow $\dot{m}_{mean\,t}$	17.9 g/s
Percent Core Mass Flow	0.13%
Achievable Blade Force F_{exc}	1.2 N

8 Appendix

8.1 Supplementary to Forced Response Testing

The equation describing vibrational behavior of structures and governing forced response is given in [21] as

$$m\ddot{x} + c\dot{x} + kx = F(t) \tag{8.1}$$

, where M is the mass, C the system damping and K the stiffness.
F(t) is the (periodic) force as introduced by a system used for the forced response test as is explained in more detail below.
As outlined in [21, 3], the above mentioned system damping originates from different sources, namely structural and aerodynamic damping.
Whereas structural damping including friction[1] and material damping is a welcome feature limiting vibrational amplitudes by dissipating energy, aerodynamic damping needs to be regarded more critical.
Other than the always positive structural damping, certain conditions can result in a negative aerodynamic damping that adds to the vibrational energy instead of dissipating it. This is referred to as flutter.
With the occurrence of flutter, initially small vibrational displacements begin to grow and become unstable. If no nonlinear effects limit the amplitudes, this phenomenon will eventually result in system failure either through HCF[2] or through overload by exceeding the maximum material stresses.
The equation governing free vibrations is given in [21] as

$$m\ddot{x} + kx = 0 \tag{8.2}$$

, where the system damping is zero and

$$m\ddot{x} + c\dot{x} + kx = 0 \tag{8.3}$$

for damped free vibrations.
As explained above, in case of flutter the system damping becomes negative which is possible

[1] Modern blisk designs lack friction surfaces and hence friction damping.
[2] High Cycle Fatigue

because of the contribution of aerodynamic damping.

8.2 Supplementary to Technical Specifications

The following graph in Figure 8.1 shows the work coefficient as result of the flutter predictions for R6 design loop 2b. The flutter analysis was performed by Volvo Aero.
It can be readily seen, that the 1F is the mode most likely to flutter for an interblade phase angle of about -50°.

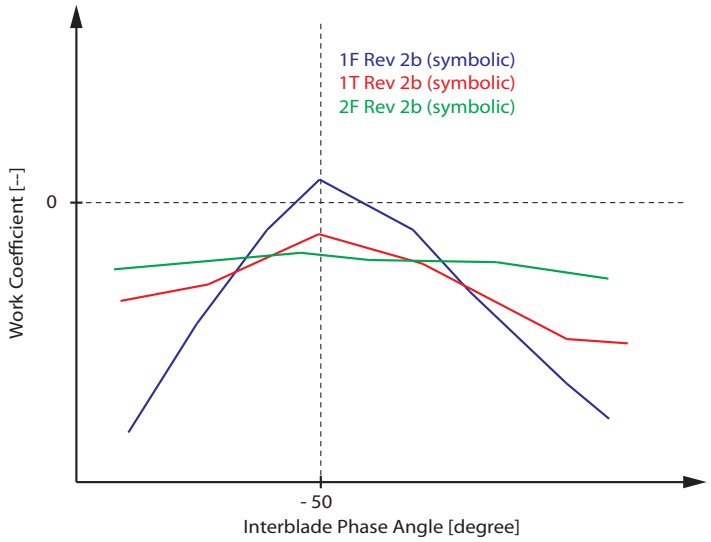

Figure 8.1: Volvo Aero flutter prediction results (interblade phase angle inversely defined and symbolic values only)

8.3 Supplementary to Oscillating VIGVs

Figure 8.2 shows the contour plots for time averaged Mach number[3] and static pressure.
The conclusion is the same as drawn before that the oscillating motion of the VIGVs does not have a significant impact on the compressor flow field.

[3] in stationary frame

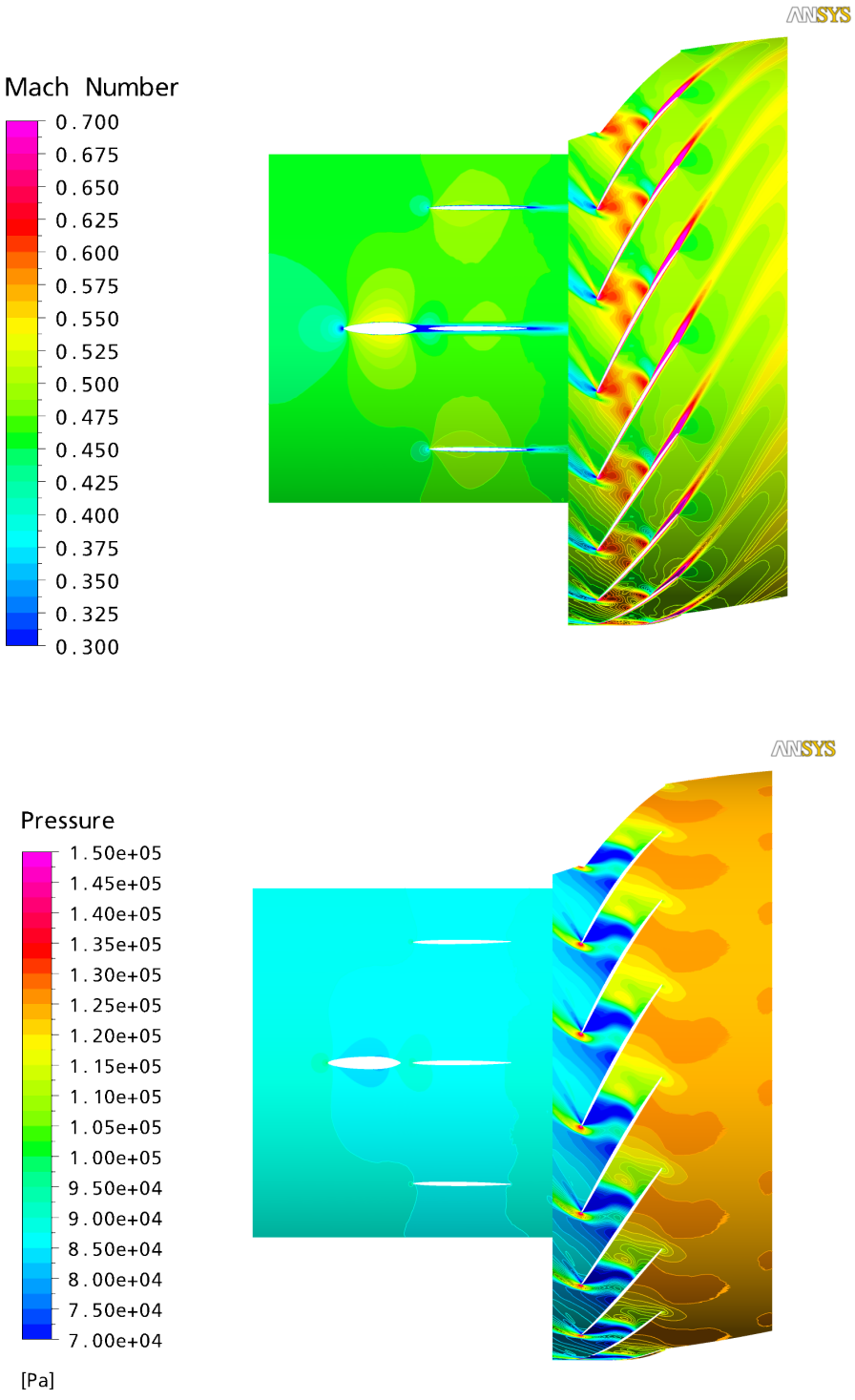

Figure 8.2: Time averaged M_{stn} (top) and p_s (bottom) for 0.5° VIGV oscillation

8.4 Supplementary to Rotating Cylinders I

Figure 8.3 shows the contour plots of time averaged Mach number and static pressure. Since the flow field does not differ significantly from the parallel rotating cylinders due to the diminishing Magnus effect, this setup was not further investigated.
For comparison reasons, the parallel rotating case is also shown.
The used cylinder geometry is for both cases the slotted cylinder with a slot width of 2 mm.

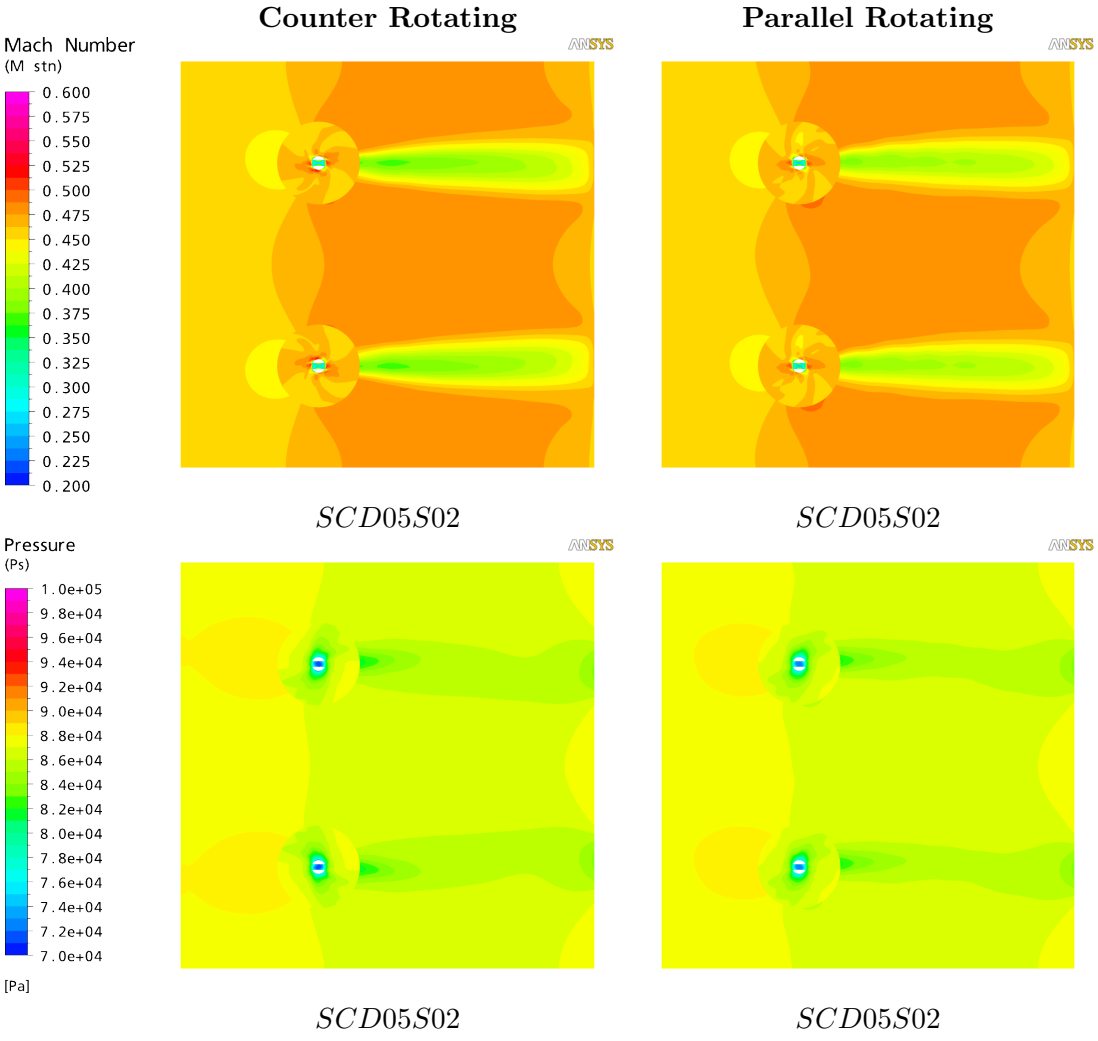

Figure 8.3: Time averaged M_{stn} and p_s for counter rotating and parallel rotating cylinders

8.5 Supplementary to Rotating Cylinders II

Figures 8.4 thru 8.8 show the results of the FFT of the velocity fluctuations induced by the cylinder rotation.

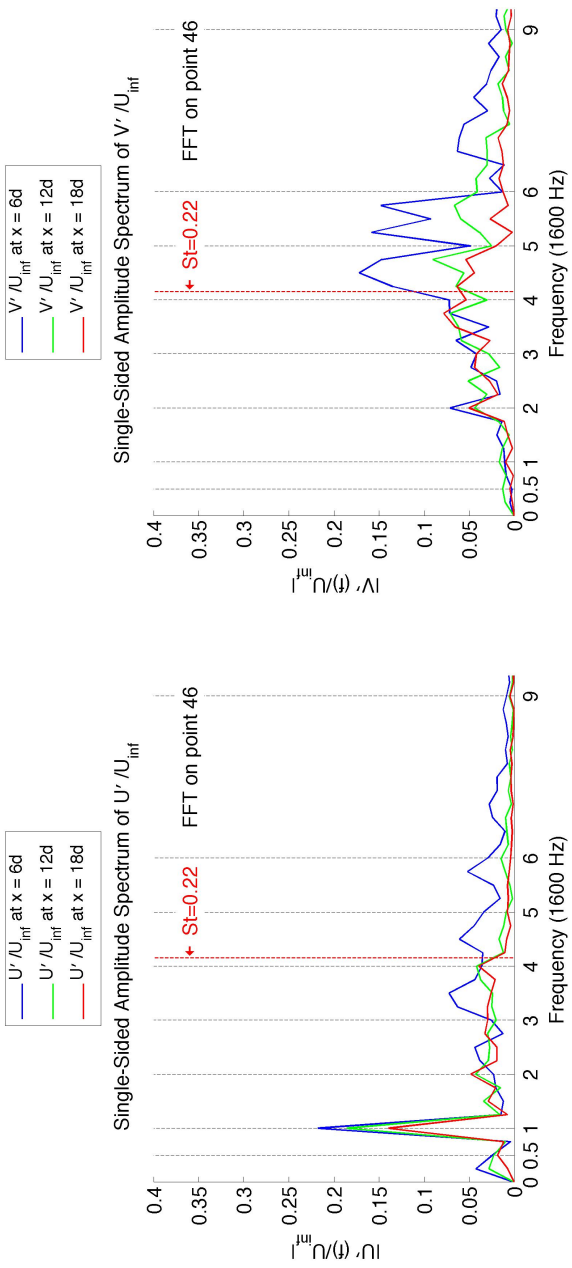

Figure 8.4: SCD05S01: FFT of velocity fluctuations induced by cylinder rotation

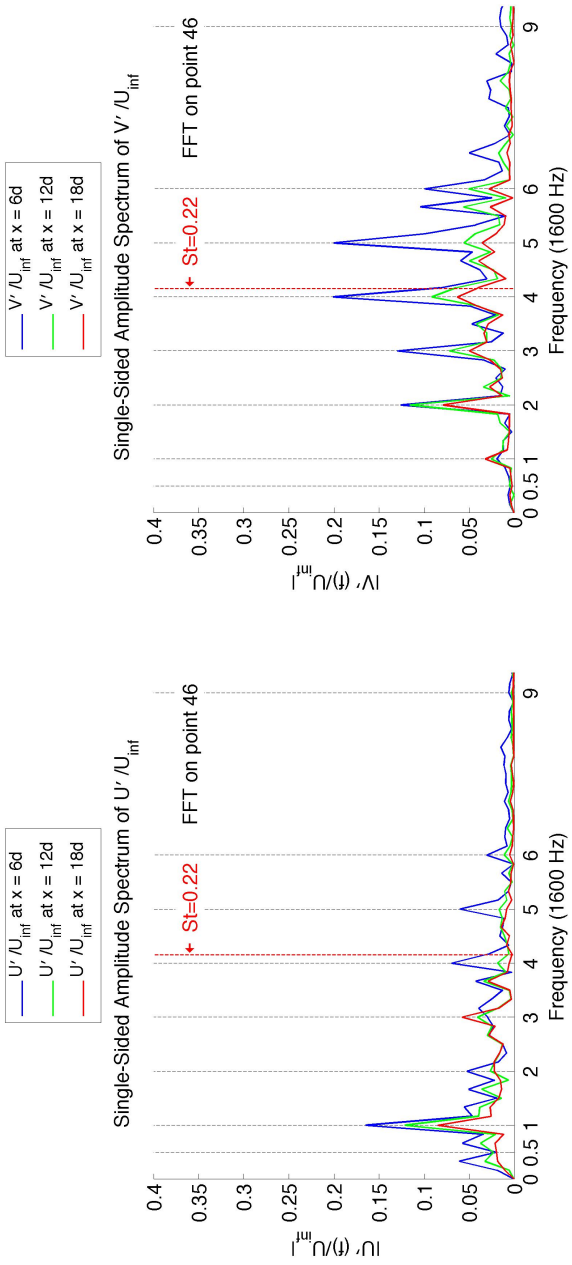

Figure 8.5: SCD05S02: FFT of velocity fluctuations induced by cylinder rotation

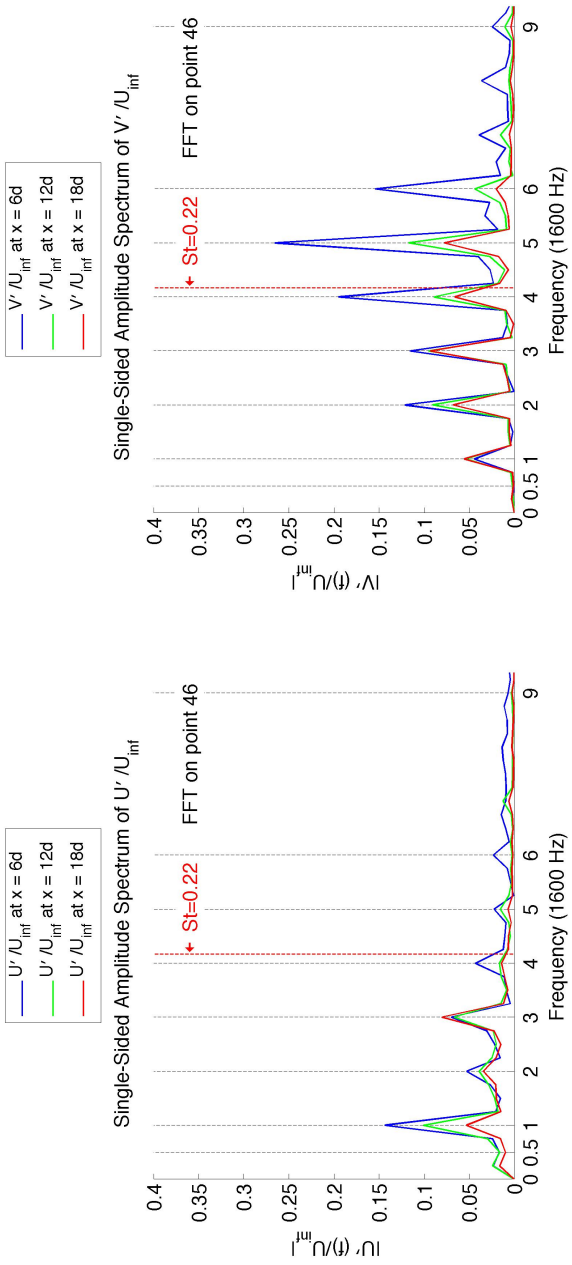

Figure 8.6: SCD05S03: FFT of velocity fluctuations induced by cylinder rotation

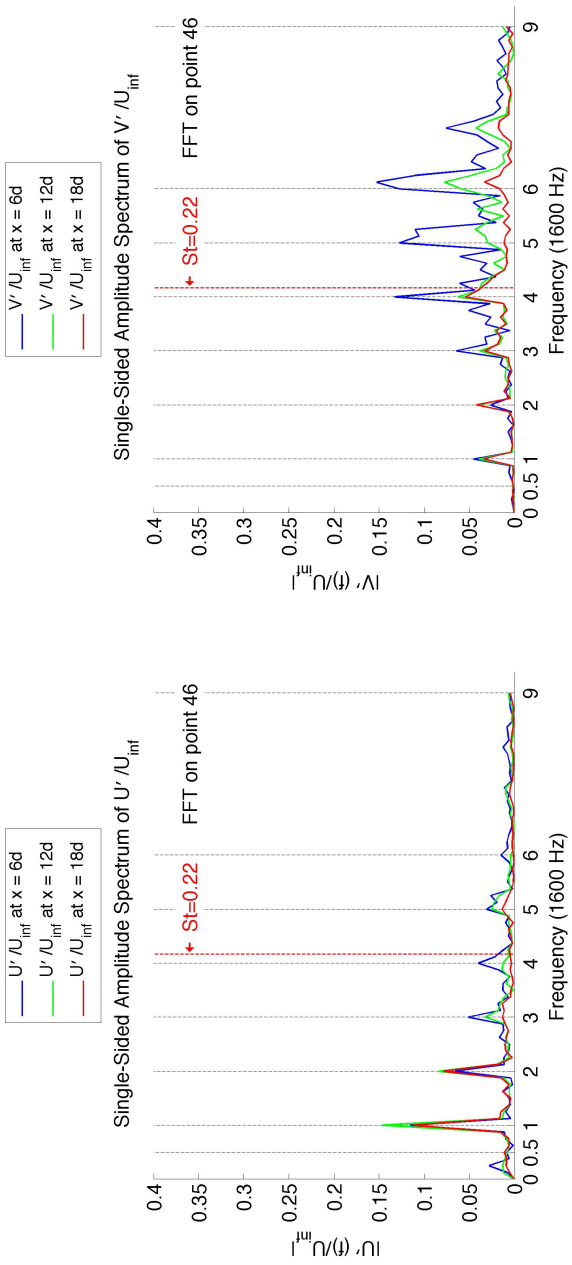

Figure 8.7: CCD05S01: FFT of velocity fluctuations induced by cylinder rotation

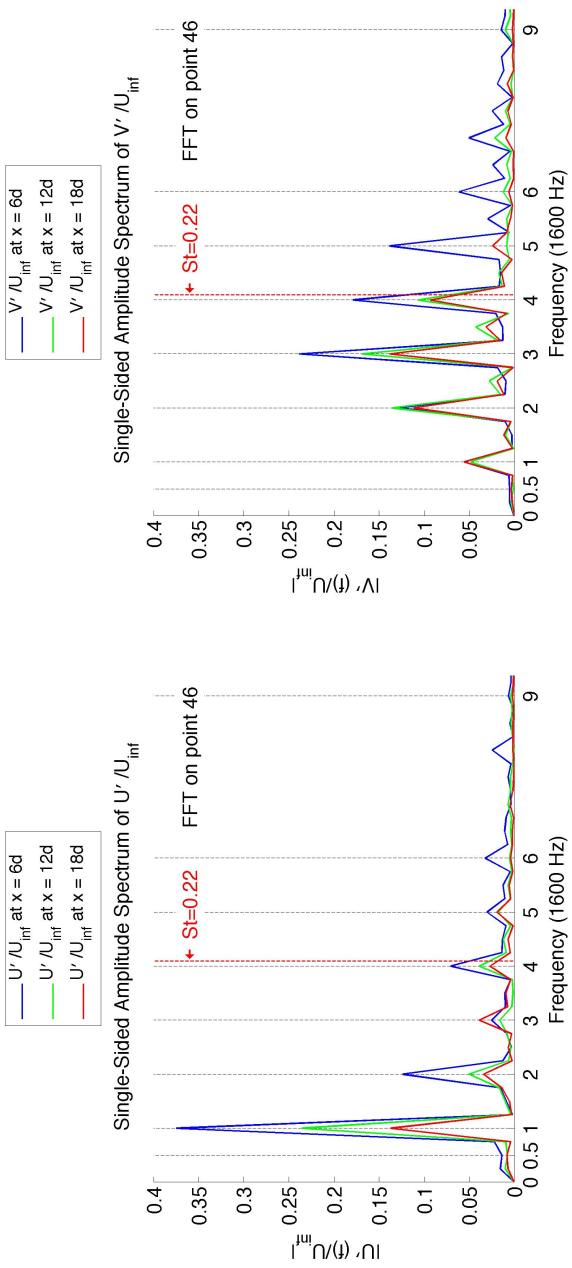

Figure 8.8: ECD05a3b1: FFT of velocity fluctuations induced by cylinder rotation

References

[1] FUTURE Annex I - Description of Work. Seventh Framework Programme, Theme 7.1, Aeronautics and Air Transport, 2008. Grant Agreement No.: 213414.

[2] J.E. Bardina, P.G. Huang, and T.J. Coakley. Turbulence Modeling Validation. AIAA Paper 97-2121, 1997.

[3] Edward F. Crawley. Aerodynamic Damping Measurements in a Transonic Compressor. ASME Paper 82-GT-287, 1982.

[4] E.F. Crawley. Measurements of Aerodynamic Damping in the MIT Transonic Rotor. MIT Gas Turbine and Plasma Dynamics Laboratory Report No. 157, 1981.

[5] E.F. Crawley, J.L. Kerrebrock, and J. Dugundji. Preliminary Measurements of Aerodynamic Damping of a Transonic Compressor Rotor. Measurement Methods in Rotating Components of Turbomachinery, ASME 79-57425, 1980.

[6] N.A. Cumpsty. *Compressor Aerodynamics*. Krieger Publishing Company, 2nd edition, 2004.

[7] John D. Gill and V. R. Capece. Experimental Investigation of Flutter in a Single Stage Unshrouded Axial-Flow Fan. 42$^{\text{nd}}$ AIAA Aerospace Sciences Meeting and Exhibit, AIAA 2004-686, 2004.

[8] Philip Hill and Carl Peterson. *Mechanics and Thermodynamics of Propulsion*. Addison-Wesley, 2nd edition, 1992.

[9] Felix Holzinger. VIGV design. FUTURE Report No.: FTR-5-4, 2008.

[10] E. Johann, B. Mück, and J. Nipkau. Experimental and Numerical Flutter Investigation of the 1$^{\text{st}}$ Stage Rotor in 4-Stage High Speed Compressor. ASME Turbo Expo 2008, GT2008-50698, 2008.

[11] Christian Lundh. Design Presentation Assy_R1S1-3d-1.10-1-1.ppt. WP3 TUD Compressor Design Presentation, 2008.

[12] Hans Mårtensson, Joergen Burman, and Ulf Johansson. Design of the high pressure ratio transonic $1\frac{1}{2}$ stage fan demonstrator Hulda. ASME Turbo Expo 2007, GT2007-27793, 2007.

[13] Jan Oestlund. Test specification including instrumentation. FUTURE Report No.: FTR-5-2, 2009.

[14] A. J. Sanders, D. C. Rabe, and K. K. Hassan. Experimental and Numerical Study of Stall Flutter in a Transonic Low-Aspect Ratio Fan Blisk. ASME Turbo Expo 2003, GT2003-38353, 2003.

[15] G. Schulze, C. Blaha, D. K. Hennecke, and J. M. Henne. The Performance of a New Axial Single Stage Transonic Compressor. Proceedings of the 12th International Symposium on Air Breathing Engines, ISABE paper 95-7072, 1995.

[16] Glen Snedden. WebEx.ppt. FP7 - Compressor excitation system, WebEx-Teleconference, 2008.

[17] Joseph H. Spurk. *Stroemungslehre - Eine Einfuehrung in die Theorie der Stroemungen.* Springer, 5th edition, 2004.

[18] H. Stargardter. Subsonic/Transonic Stall Flutter Study, Final Report. NASA CR-165256, June 1979.

[19] Damian Vogt. Blade Row Interaction Phenomena. Lecture Notes MJ2430 / MJ2244, 2008.

[20] Damian Vogt. Damping. Lecture Notes MJ2430 / MJ2244, 2008.

[21] Damian Vogt. Structural Dynamics. Lecture Notes MJ2430 / MJ2244, 2009.

[22] I.H. Woods. 167-4-300309tn.doc. FUTURE WP3 - Results of Preliminary Blisk Design Version 10, 2009.